Fakultät für Medizin

Institut für diagnostische und interventionelle Radiologie

Analysis of multi-energy spectral CT for advanced clinical, pre-clinical, and industrial applications

Radin Adi Aizudin Bin Radin Nasirudin

Written by:

Radin A. Nasirudin

2014

Abstract

The attenuation of X-ray photons is material- and energy dependent. This dependency can be exploited to obtain additional spectral information of the scanned object. This work focuses on the different techniques of multi-energy CT and the possible clinical applications that take advantage of the additional information obtained. The main aim is to study the effectiveness and the applicability of two material decomposition techniques – image-based and projection-based material decomposition – in detecting and distinguishing two or more materials in an object. The decomposed images are then used for various applications such as for beam-hardening corrections, metal artifact reduction, detection of low-concentrated contrast medium, and the distinguishing of two or more K-edge materials. Results from each of these applications show a significant improvement in image quality, the ability to enhance low iodine signal in the image, and the potential usage of a mixture of two or more contrast agent in a single scan. Additionally, the same material decomposition techniques are tested with objects scanned with micro-CT. The positive outcome of this investigation shows the feasibility of extending the algorithm for applications beyond medical purposes such as for pre-clinical imaging and non-destructive testing. In conclusion, multi-energy CT provides many advantages in clinical diagnostics as well as in pre-clinical and industrial CT.

Acknowledgement

the good times and the bad times. There is always a reason to smile when she is around.

Lastly, this dissertation is specially dedicated to my younger brother Aliff, who passed away when I was writing this work. Thank you for the beautiful childhood memories we had together and the great things you have done for the family. We were blessed with all the joy you brought to our life. You will always be in our prayers. Al-Fatihah.

Contents

Notations and Abbreviations

AS: Analytical Simulation

CAD: Computer-Assisted Diagnosis

CIN: Contrast-Induced Nephropathy

CM: Contrast Medium

CNR: Contrast-Noise-Ratio

CT: Computed Tomography (X-ray)

CTC: CT Colonoscopy

DECT: Dual-Energy CT

FBP: Filtered-Back Projection

HU: Hounsfield Unit

IR: Iterative Reconstruction

KCR: Known Component Reconstruction

MAR: Metal Artifact Reduction

MCS: Monte-Carlo Simulation

MLIR: Maximum-Likelihood Iterative Reconstruction

PCD: Photon-Counting Detector (PCD)

SCT: Spectral CT

SPIR: Spectral-driven Iterative Reconstruction

VMI: Virtual Monochromatic Image(s)

VRT: Variance Reduction Technique

WL: Window Level

WW: Window Width

List of Tables and Figures

Chapter 1

Introduction

1.1 Motivation

Soon after the introduction of CT in early 1970s, researchers in the medical imaging field began to pursue the idea of dual-energy CT (DECT). Early investigators such as Alvarez, Macovski and Lehmann [1-3] recognized the potential of dual-energy x-ray acquisition for characterization of tissue, bone and other components in the body. However, DECT approach was abandoned due to the limitations of CT scanners at that time [4, 5]. Previously, DECT acquisition required two separate scans. This was problematic not only due to dose consideration, but also due to poor image registration as a result of movement between scans. Thus, dual energy scans were deemed unfeasible on human subject.

Since then, CT scanners have undergone many developments and technical advances. The introduction of slip ring in the gantry, for example, enables the fast scanning of patients within a single breath-hold [6, 7]. Improvements in CT scanners have revived the idea of multi-energy imaging and made DECT acquisition on human subject possible again. The availability of DECT imaging has improved tremendously the diagnostic processes; while at the same time provides additional spectral information that aids diagnosis [8, 9].

Further advancements in detector technology have contributed to the development of energy-resolved photon counting detectors (PCDs). PCDs have the ability to discriminate incoming photons based on their energies – PCDs split the X-ray spectrum into several predefined energy bins – enabling the acquisition of separate CT data in each energy bin [10, 11]. As a result more information of the object can be obtained in a single scan at the same tube voltage. Besides that, quantum efficiency in PCDs suppresses electric noise at the detectors; thus low dose acquisition protocol is possible without compromising the quality of the CT image.

This work focuses on the different techniques of multi-energy CT and the possible clinical applications that take advantage of the additional information

obtained from the techniques. New applications and algorithm were developed for DECT and photon counting based spectral CT.

1.2 Organization

This dissertation is divided into several chapters. It begins with an introduction to X-ray CT imaging, which includes a brief overview on the X-ray physics and image reconstruction.

Chapter 3 discusses dual-energy CT (DECT) technique. The chapter starts off with an explanation of the theory of dual-energy imaging, as well as the different implementations of DECT. Then, new possible clinical applications for DECT are introduced and the results of proposed clinical application are shown. In Chapter 4, the fundamental idea of photon counting based Spectral CT (SCT) is explained, including the detector technology that enables the implementation of such technique. The data generation methods used in this work are described, which includes two simulation techniques and the acquisition of spectral data using the Medipix3RX chip. Further, three possible clinical applications specially designed for Spectral CT are introduced and the results are shown and discussed.

In Chapter 5, the possibility of extending the developed algorithms to applications beyond clinical CT, such as in pre-clinical imaging and in industrial CT, is investigated. In order to test the feasibility, the same algorithm developed for clinical applications are tested on data acquired from a Micro-CT.

A general discussion on this work and the future directions are discussed in Chapter 6. Finally, a brief but concise summary on a whole is given in the last chapter.

Chapter 2

Principles of X-ray CT Imaging

This chapter briefly describes the principles of X-ray CT imaging, from the generation of X-ray in CT to the detection process at the detector, and finally to the process of image reconstruction. Explanations on the various physical processes that take place in between are also provided. At the end of the chapter, a short overview of the relationship between image quality and radiation dose is given.

2.1   X-ray Generation

X-rays for usage in clinical radiography and CT are produced by accelerating a beam of high-energy electrons onto a metal target. Upon striking the metal solid anode, the electrons experience rapid deceleration, generating X-ray photons with a wide range of energies that are commonly called bremsstrahlung. If the electrons have sufficient energy, they can eject an electron out of an inner shell of the target metal atoms. Then, electrons from higher state fill the hole left by the expelled electron, in the process emitting another type of radiation known as the characteristic X-rays of the target material [12].

A typical X-ray tube used in CT consists of rotating metal target at the anode and small thin tungsten filament at the cathode, enclosed in an evacuated vessel made of glass. The evacuated vessel is surrounded by oil to provide cooling, by dissipating heat from the tube, and electrical isolation. A schematic diagram of an X-ray tube is shown in Figure 2.1.
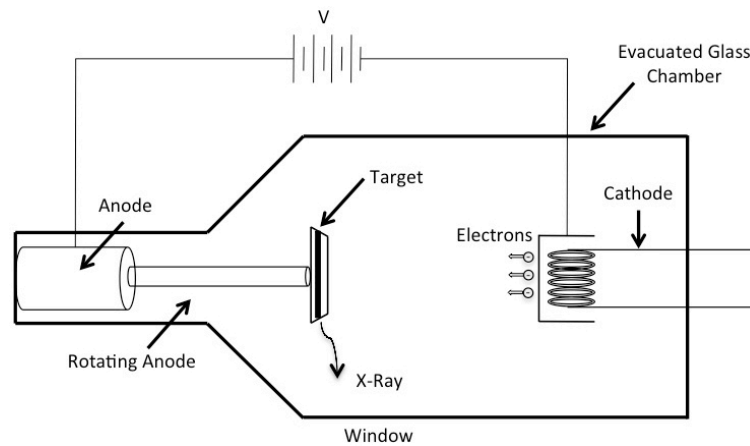
Figure 2.1: The schematic diagram of an X-ray tube.

There are a few considerations for the metal anode target. First, the metal anode must be able to produce X-rays efficiently. A general rule is that metal with high atomic number has higher X-ray production efficiency. Secondly, due to the constant bombardment of electrons, the metal must be able to withstand high heat. A commonly used metal target is tungsten, which has a high atomic number, 74, and a high melting point of 3400°C [12]. Other suitable metal targets are molybdenum and rhodium. Even though tungsten is considered to be an efficient anode metal target, only about 1% of the energy of the electrons is converted into X-rays, while the remainder of the energy is dissipated as heat. Due to high heat dissipation in the X-ray generation process, the anode is rotated to reduce the localization of heat.

Adjusting the electrical parameters of the tube controls the quality and the quantity of the X-ray. The range of the produced photon energies, also called the X-ray spectrum, can be adjusted by changing the potential difference (kV) between the anode and cathode. On the other hand, the tube current (mA) and exposure time (s) determines the quantity of the produced X-ray photons. An increase either in the tube current or exposure time increases the number of X-ray photons generated by the tube. An example of X-ray spectrum produced from a clinical grade tube at different voltages is shown in Figure 2.2.
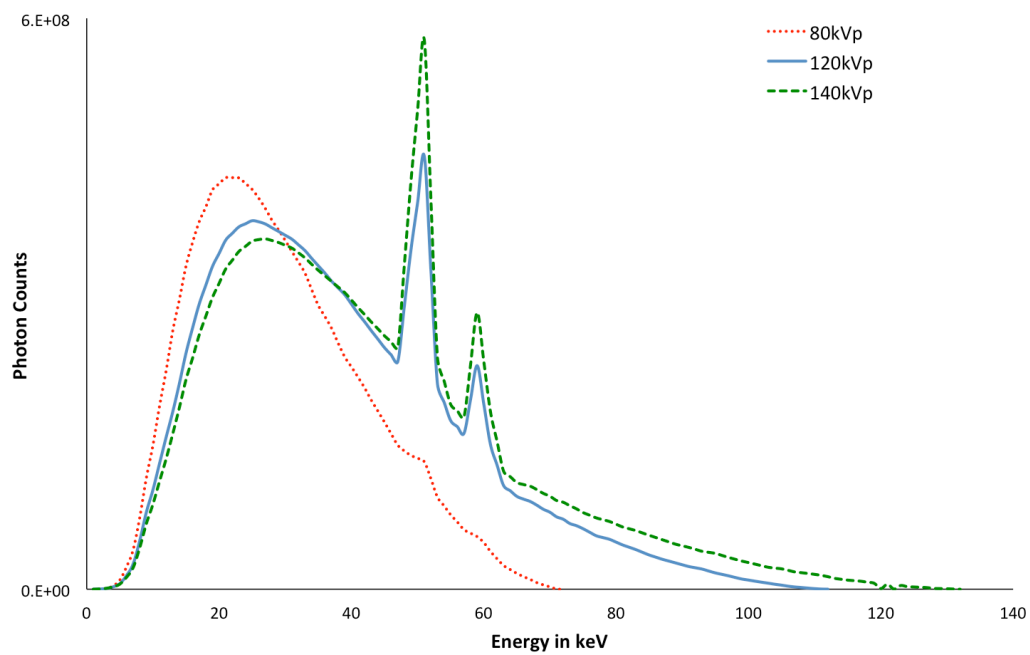
Figure 2.2: X-ray spectrum generated at different energy levels.

2.2 Photon-Matter Interaction

As the X-ray photons penetrate a scanned object, the material in the scanned object attenuates the photons. In the diagnostic energy range of 25keV to 150keV, the photon-matter interactions that take place are the Rayleigh scattering, photoelectric absorption and Compton scattering (see Figure 2.3). Rayleigh scattering is the elastic scattering of the electromagnetic radiation by particles much smaller than the wavelength of the incident radiation. In Rayleigh scattering, the energy of the photons is conserved, but the direction of the incident photon changes. Rayleigh scattering is dominant at low energy but becomes constant as the energy of the incident photon increases. Therefore, Rayleigh scattering is of less interest in CT, but has been shown to be sensitive to structural variation and density fluctuation, and is important in bone characterization and in deriving cellular and molecular information [12, 13].
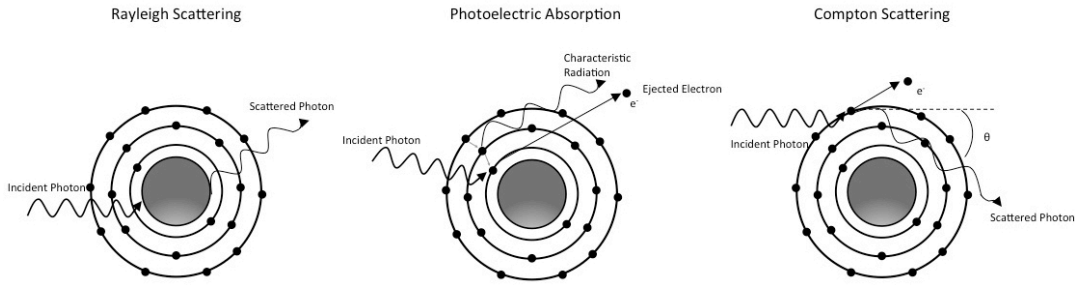
Figure 2.3: The photon-matter interactions in diagnostic imaging energy range. Rayleigh scattering only occurs at a very low energy, thus the primary photon-matter interactions in diagnostic are photoelectric absorption and Compton scattering.

The next important photon-matter interaction is the photoelectric absorption. In this physical process, the entire energy of an incident X-ray photon is absorbed by an atom, resulting to the ejection of an electron of a lower shell from the atom. Some of the energy is used to liberate the electron, while the rest is converted to the emitted photoelectron's kinetic energy. Electrons from the outer shells then fill the vacancy left by the ejected electron, in the process emitting X-ray characteristic of the atom. In order for photoelectric absorption to occur, the energy of the incident X-ray must be greater than or at least equal to the binding energy of the inner-shell electron. The probability of photoelectric absorption depends on the energy of the incident photon and the atomic number, Z, of the absorber material and can be approximated by:

$$\alpha \propto \frac{Z^4}{E^3} \tag{2.1}$$

The strong Z^4 dependence of the absorption coefficient makes iodine ($Z = 53$) or barium ($Z = 56$) an ideal choice for contrast media in CT. However, due to low effective atomic number of biomaterial in the body ($Z_{eff} \approx 7.6$) and the E^{-3} dependence, the probability of photoelectric absorption is only dominant in the lower energy (< 50 keV) range and decreases rapidly as the photon energy E increases.

The primary particle-matter interaction in the diagnostic imaging energy range is the Compton scattering. Compton scattering occurs when an X-ray photon collides with a loosely bound valance electron in the outer shell. The interaction causes the incident photon to transfer part of its energy to the recoiling electron, also known as the Compton electron or secondary electron, while the rest of the energy is kept by the scattered photon. If the energy is adequate, both the scattered photon and the

Compton electron may undergo further interactions such as Rayleigh scattering, photoelectric absorption, or even Compton scattering. As the incident photon energy increases, both scattered photons and electrons are more likely to be scattered in the forward direction; thus, these photons are more likely to be detected by the detector. For an incident photon with energy E, the total cross section for Compton scattering can be derived from the Klein-Nishina equation [1]:

$$f_{KN}(\varepsilon) = \frac{1+\varepsilon}{\varepsilon^2}\left[\frac{2(1+\varepsilon)}{1+2\varepsilon} - \frac{1}{\varepsilon}ln(1+2\varepsilon)\right] + \frac{1}{2\varepsilon}ln(1+2\varepsilon) - \frac{(1+3\varepsilon)}{(1+2\varepsilon)^2} \quad (2.2)$$

with $\varepsilon = E/511$ keV
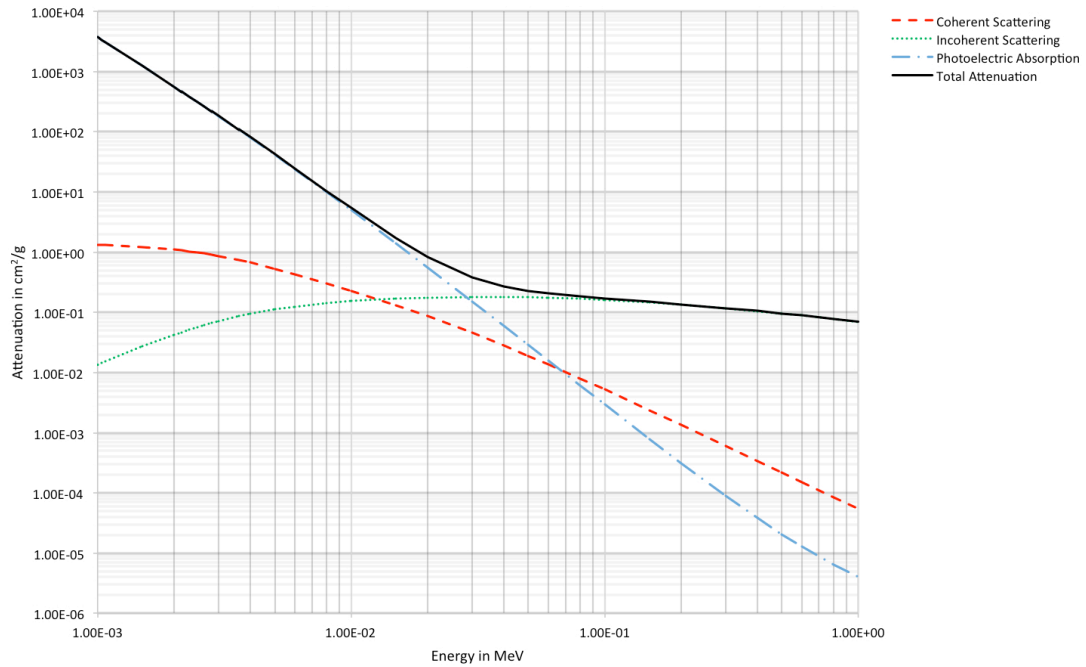
Figure 2.4: Mass attenuation coefficient of soft tissue, as defined by ICRU-44. At lower energy below 25 keV, photoelectric absorption is the most dominant attenuation factor, but at the higher energy, Compton scattering (incoherent scattering) dominates the most.

2.3 Detector

After interaction with matter in the scanned object, remaining photons are detected at the detector. Most modern CT systems available are equipped with scintillator detectors. A scintillator detector consists of two components: the scintillator medium and the photon detector [12] (see Figure 2.5). Generally, the detection process occurs in two steps. In the first step, the incident photons are converted into optical photons (or light) inside the scintillation media. The photodiode

absorbs the emitted light and reemit signals in the form of electron charges. These electrons are first amplified, before they are collected and integrated at the integrator. Finally, these analog signals are converted to digital signals by an Analog-Digital-Converter.
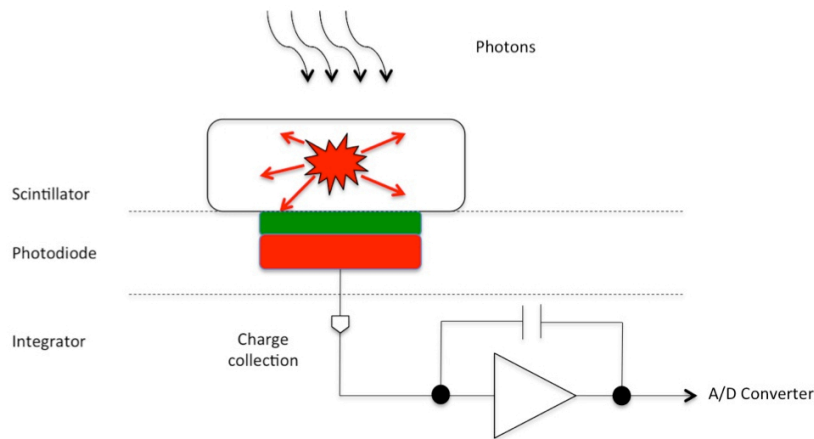
Figure 2.5: A schematic diagram of a CT detector. Incident photons are first converted into optical photons in the scintillator and subsequently converted into electrical signal at the photodiode. The electrical signal is then collected and converted into digital signal.

Earlier generations of CT scanners are equipped with single row detectors. The introduction of multi-row detector CT (MDCT) has improved scanning times and enables the imaging of rapidly moving organs such as the heart. The fast scanning time is mainly due to the increased coverage in a single rotation and is in particular advantageous in clinical cardiac CT.

2.4   Image Reconstruction

There are two main categories of image reconstruction in CT, analytical reconstruction and iterative reconstruction [14, 15]. The most popular reconstruction algorithm in the analytical reconstruction category is the filtered back-projection (FBP). In the FBP algorithm, the projection data obtained from the CT scanner is first filtered in the frequency domain, before the filtered data is back-projected into an image. The back-projection process involves adding each filtered projection dataset's contribution to each pixel of the final image (see Figure 2.6). The quality of the final image depends on the filter, also known as reconstruction kernels, used. The selection of the reconstruction kernel is based on the intended clinical application. In general, a smooth kernel generates less noisy images but with reduced spatial resolution, which

makes it suitable to view soft tissue. On the other hand, a sharp kernel offers images with higher spatial resolution, but has the drawback of increased noise in the image. The usage of a sharp reconstruction kernel is mostly suitable to assess bony structures. FBP is the reconstruction method of choice because it is very fast. However, one particular disadvantage of FBP is that in the back-projection process, all X-rays are equally weighted, although in reality the X-ray source is polychromatic in nature. The discrepancy between the simplified model of FBP and the true physical nature of the acquisition gives rise to artifacts in images such as beam hardening.
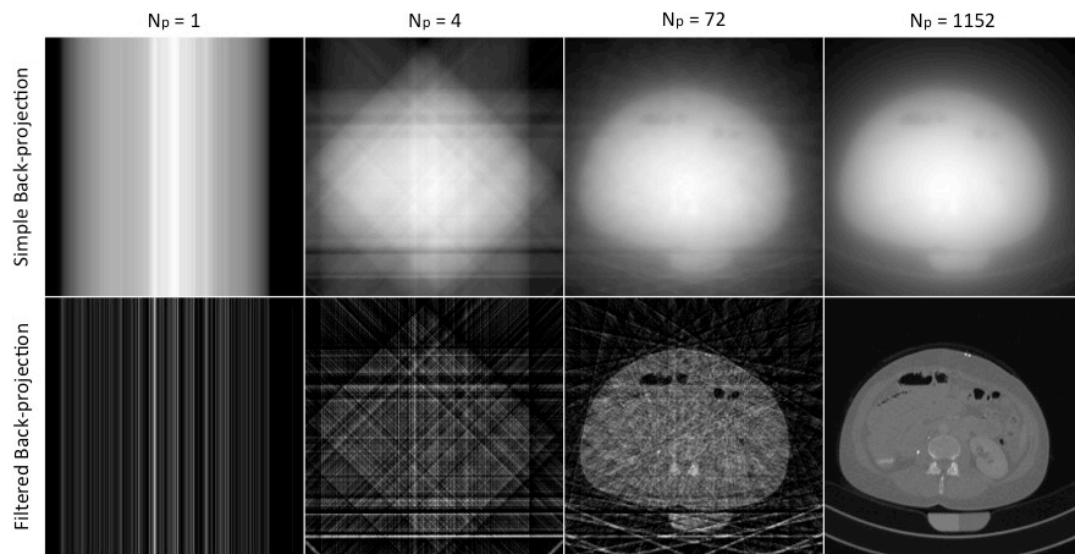
Figure 2.6: A comparison between simple back-projection, and filtered back-projection (FBP) presented for different numbers of projections (column-wise). The higher the number of projections, the higher is the sampling rate, thus the better the image quality will be.

Another method of image reconstruction in CT is iterative reconstruction. Iterative reconstruction takes into account the accurate modeling of the acquisition process, such as the photon statistics, X-ray beam spectrum, and the detector absorption efficiency. Although the first CT image reconstruction by Hounsfield was carried out using iterative reconstruction, this technique was not the method of choice for image reconstruction due to the massive computation effort involved. With the advancement of computational technology in recent years, iterative reconstruction has gained in popularity [15, 16]. The accurate modeling of the acquisition process results in a reduced appearance of image artifacts such as beam hardening and metal artifacts in CT images. Further, it has been shown that the usage of iterative reconstruction has the potential to reduce radiation dose, without compromising the diagnostic quality of

the image [17]. There are many types of iterative reconstruction algorithms developed by the medical imaging community; with the most popular ones are the algebraic reconstruction technique (ART) and the maximum-likelihood (ML) method.

2.5 Image Quality and Radiation Dose

Image quality in CT is important as it can determine the outcome of patient diagnosis. Generally, image quality can either be assessed visually or measured quantitatively [18]. In a visual assessment, also known as human observer-based measurements, radiologists subjectively score the CT images according to a set of criteria, for instance, tissue contrast and lesion detectability. Common human observer-based tests include receiver operating characteristics (ROC) and alternative forced-choice (AFC). Human observer-based measurements are usually the benchmark for image quality assessment, but are impractical as such tests are time-consuming, prone to bias, and limited to specific acquisition parameters and techniques. On the other hand, quantitative measurements, also known as observer-independent measurements, do not involve human interactions, thus are bias-free and can be universally applied to all systems and acquisition techniques[19, 20]. Metrics such as modulation transfer function (MTF) [21], noise-power-spectrum (NPS) [22], and noise-equivalent quanta (NEQ) [23] are commonly used to characterize radiographic imaging systems, but may not be the real representation of image quality for diagnostic purposes.

One important parameter for visual assessment is image contrast. Image contrast refers to the ability to differentiate small changes in tissue density [24]. In theory, CT scanners can differentiate tissue attenuation differences of less than 0.5% but the contrast detectability of different tissue depends on the amount of statistical variations (noise) in the measured region. In order to enhance low contrast detectability, good sampling statistics are needed. As the signal measured in CT is directly proportional to the amount of radiation detected, higher sampling statistics can be achieved by increasing the number of X-ray photons transmitted through the patient, or in other words, by increasing the radiation dose. The relationship between noise in an image and dose is inversely proportional and can be written as $1/\sqrt{dose}$. Thus, in order to reduce noise by half, a fourfold increase of radiation dose is required. Figure 2.7 illustrates an example of the effect of dose on image quality.
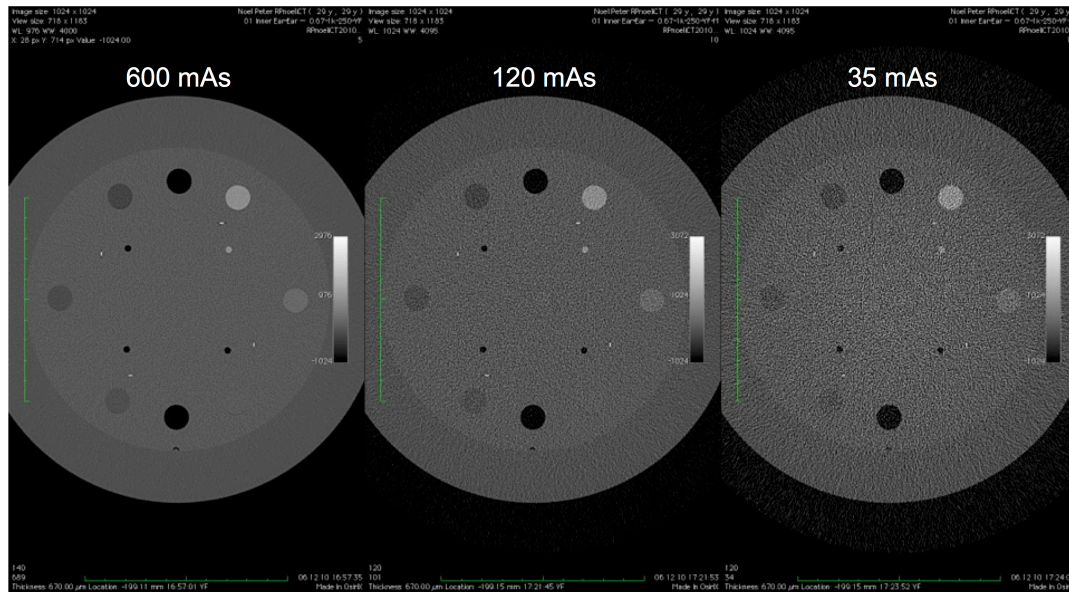
Figure 2.7: The effect of radiation dose on image quality. The image quality is best at highest dose level (600 mAs) and becomes worse as the radiation dose is decreased (from left to right). The image at the lowest dose level (35 mAs) suffers due to increased noise levels, reducing the contrast between different components in the image.

Although X-ray CT offers many benefits in clinical diagnostics, as in many aspects of medicine, there are also risks associated with the use of X-ray CT. One of the most discussed risks in recent years is the increased possibility of radiation-induced cancer [25, 26]. X-rays transmitted through patients can damage DNA and create mutations that induce tumor growth. The high association of X-ray usage to cancer has lead to many studies on methods of reducing the amount of radiation exposure to patients, without compromising image quality [27]. Suggested techniques include better image reconstruction methods such as iterative reconstruction [28, 29] and the introduction of more efficient detector technology [30]. For example, a retrospective study of CT scans done in a clinic shows that the amount of radiation dose from CT has decreased over the years (see Figure 2.8), especially on the onset of the introduction of iterative reconstruction [17]. This shows that advanced reconstruction technique can significantly reduce radiation dose, while at the same time maintain or even improve image quality.
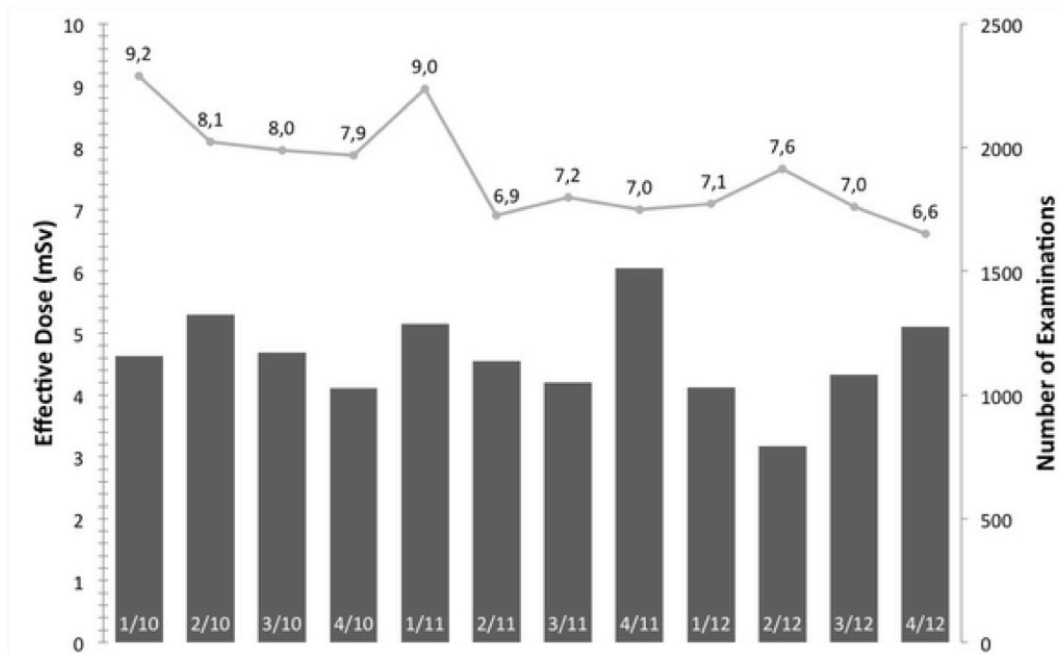
Figure 2.8: The median effective dose and number of examinations per quarter year in mSv for all types of CT examination between 2010 and 2012. After the iterative reconstruction scheme is introduced clinically (between the 1/11 and 2/11), a significant reduction in radiation exposure is reported. Source: Noël et al. PLOS ONE 8.11 (2013).

2.6 Summary

This chapter of the dissertation provides an overview of the fundamentals of X-ray CT imaging. It also forms the basis for the various concepts of multi-energy CT that will be described and explained in the rest of this work. For example, the different X-ray energies that can be generated by an X-ray tube are essential in two out of three dual-energy CT approaches, while the material- and energy dependency of X-ray photon attenuation described in section 2.2 brings forth many applications that make use of the additional information in multi-energy spectral CT.

Further, the inefficiency of conventional detector based on scintillation and signal amplification as explained in section 2.3 necessitates the development of more advanced detectors that are not only more efficient, but also are able to count and discriminate incident photons based on their energies. Besides, the need to produce images of high diagnostic quality without increasing the radiation dose has motivated the development of new algorithms that will be introduced in the following chapters of this work.

Chapter 3

Dual-Energy CT

3.1   Basic Principles

3.1.1 Attenuation Dependence

As explained in the previous chapter, the type of photon-material interactions are heavily influenced by the incident energy of a photon and the material it interacts with. The same fundamentals form the basis of Dual-Energy CT (DECT), in which the main principle behind this technique is that the attenuation of X-ray photons is material- and energy dependent. Figure 3.1 shows the attenuation of X-ray photons by different materials at different energy levels. These materials represents components normally seen in CT scans: water is a representation of soft tissues in the body, calcium for bone, and iodine for contrast medium widely used in CT scans for image enhancements. From the plot, one can see that iodine attenuates photons more in comparison to calcium and water, while at the same time, the degree of attenuation decreases with increasing photon energy. What this means is that scanning the same object with at least two different spectra yields more information on the scanned object, and thus different components in the scanned object can be distinguished.
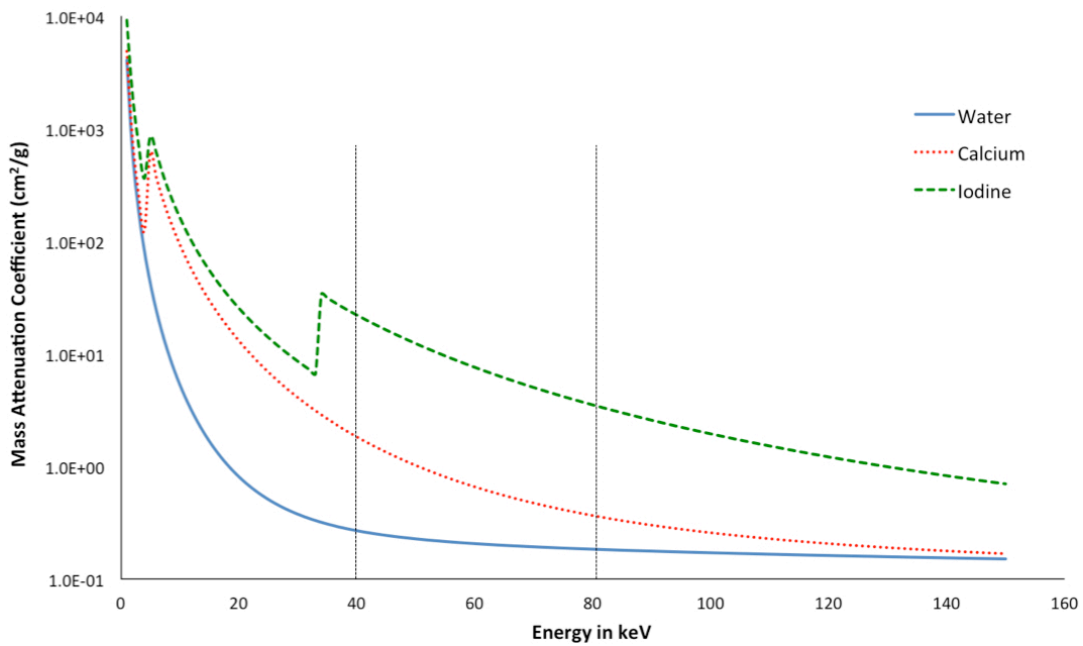
Figure 3.1: The attenuation of X-ray photons for different materials at different energy levels. Water represents the attenuation for soft tissue in the body, calcium for the bone, and iodine for the contrast agent widely used in CT. The difference of attenuation value at the low- and high-energy levels is larger for iodine than calcium and soft tissue. This difference can be used to decompose the anatomical components of the scanned object.

The choice of spectra used is essential to the degree of differentiation of materials in material decomposition techniques. Ideally, the object would have to be scanned with two distinctive spectra; one spectrum with a very low energy and another with a very high energy. Besides that, the amount of overlapping between those two spectra has to be minimal. Figure 3.2 shows three different spectra available in most clinical systems. Although the difference in energy level is high, the combination of 80kVp and 140kVp is less desirable due to the huge overlap of the two spectra. One way of increasing the spectral separation is to apply additional filters such as tin or aluminum, especially to the higher energy spectrum [31]. The effect of filtration 'hardens' the beam, i.e. increases the mean energy, and 'shifts' the spectrum to a higher energy level. An example is the combination of spectra of 80kVp together with 140kVp filtered with copper and tin, as this combination has less overlapping and thus yields better material separation.
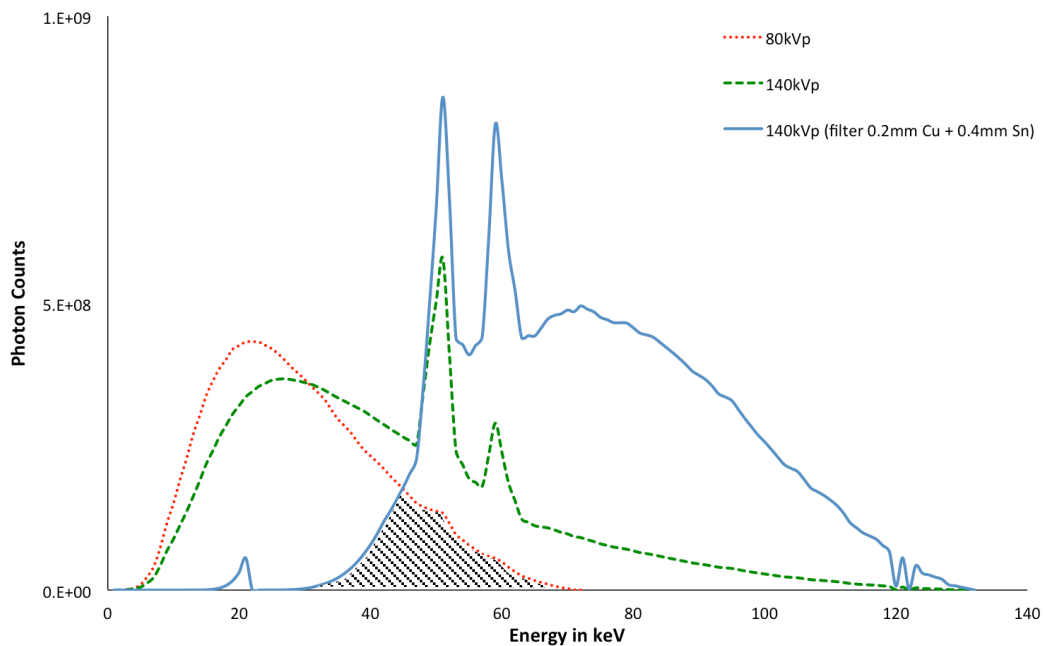
Figure 3.2: Profiles of three different X-ray spectra: unfiltered 80kVp, unfiltered 140kVp, and 140kVp filtered with copper and tin. The unfiltered spectra of 80kVp and 140kVp overlaps each other in the entire spectrum, thus has poor spectral separation. The filters 'harden' the beam and 'shift' the spectrum to a higher energy. As a result, only a small overlap exists between the low- and high-energy spectra, as shown by the shaded region.

3.1.2 Acquisition Techniques for Dual-Energy CT

There are currently several techniques of acquiring CT data with spectral information. These techniques are divided into two categories based on the working principles: the usage of different pre-patient X-ray spectra or the deployment of energy-resolving detectors.

Rapid kV-Switching

In the rapid kV-switching technique, the voltage tube of the X-ray tube is rapidly switched between the lower and higher energy at every other projection during the course of the scan [32, 33]. The projections at odd numbered angles $\theta_{1,3,5...}$ are acquired with low energy kV settings, while the projections at even numbered angles $\theta_{2,4,6...}$ are scanned with the higher kV settings. Although the acquisition of each set of projections has less angular sampling due to the alternating angles, the differences between the two sets of projections are only small and can be overcome by interpolation between the projections. In comparison to the conventional dual-energy method of scanning the same patient twice in succession, acquiring projections

alternatingly has the advantage that it is fast, does not require additional radiation dose, and avoids artifacts due to patient motion. Besides, the rapid kV-switching technique enables instantaneous scanning of changes in contrast medium concentration.

The rapid kV-switching method requires fast generator and scintillator response. Current X-ray tube technology only enables tube voltage switching in the magnitude of one half a millisecond. This means that in order to avoid angular sampling artifacts, the CT needs to be rotated at 0.6 – 1s, even though modern CT systems are known to be able to rotate at 0.35s [32]. As a consequence, this method is unsuitable for scanning of fast moving organs such as the heart or dynamic perfusion scans. Another consideration is the dose imbalance between the low-energy and high-energy acquisition. While the X-ray tube can be rapidly switched, the tube current cannot be rapidly changed. At equal tube current, 80kV acquisition yields as much as 3 times lower dose than 140kV [32]. A solution to this problem is to increase the integration time of the 80kV by a factor of three, thus the X-ray flux of both acquisitions will be approximately the same.
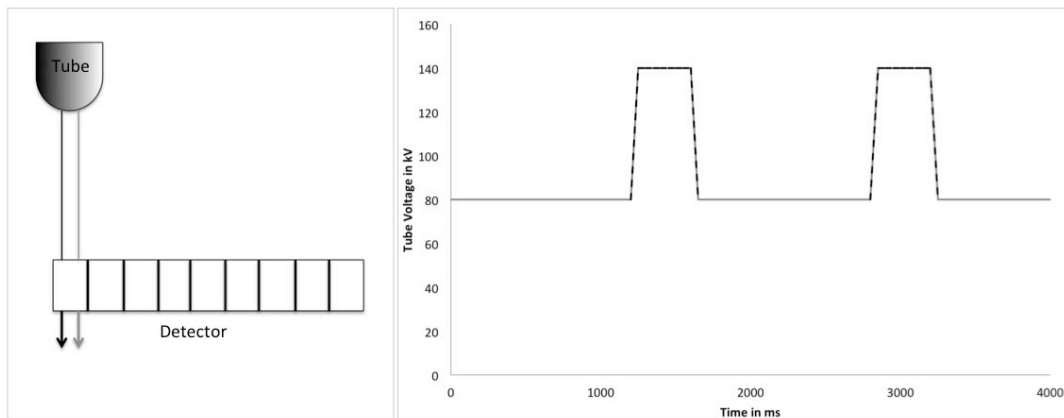
Figure 3.3: Left: A sketch of a kV switching system. This method employs a single X-ray tube and a corresponding detector. The voltage of the tube alternates between the low- and high-energy for every other projection. Right: An ideal fast kV switching scheme. The integration time for the 80kV is longer than for 140kV in order to equalize the radiation dose between the low-energy and the high-energy spectra.

A further drawback of the kV-switching method is the under- or overshoots of the tube voltage [32]. Ideally the switching curve of the X-ray tube has to be a rectangle, as shown in Figure 3.3. However, under- or overshoots of voltage can occur due to the instability of the generator, and as a consequence reduce the spectral

separation between the generated energy spectra. A way to limit such occurrence and to enable stable switching of tube potential is to optimize both acquisition settings (e.g. tube current) to only the high tube current at the expense of the ability to modulate dose according to specific examination.

Dual-Source CT

Another widely used method for DECT that utilizes differences in pre-patient X-ray spectra is dual source CT (DSCT). A DSCT is equipped with two acquisition systems (two X-ray tubes and two corresponding detectors) that are simultaneously operated to acquire data from the same anatomical slice [32]. DSCT has several advantages to other DECT methods. Firstly, each X-ray tube-detector pair can be individually adjusted. Scan parameters such as tube voltage and tube current can be independently set-up and thus the problem of unequal radiation dose from a low- and high-energy acquisition is eliminated. The availability of dedicated detectors avoids the problem of slow scintillator response between the different energy acquisitions. The second advantage of DSCT is that, due to the simultaneous acquisition of data, DSCT systems have improved temporal resolution and are suitable to image rapidly moving organs such as the heart and lungs [34]. Further, the simultaneous acquisition avoids registration problems for the two sets of low- and high-energy projections. This is important for many diagnostic applications using contrast medium for contrast enhancements, as early changes in contrast agent concentration can be accurately detected.

Nevertheless, mounting separate acquisition systems in a single gantry poses several technical limitations. The limited space in a gantry means that one of the two detectors has to be built smaller than the other one, resulting in two different fields of views (FOV). A typical combination is the detector A has full FOV, while detector B has about half the FOV of detector A. The smaller FOV for the second detector can be a problem for the examination of larger-sized patients and makes raw-data based dual-energy algorithms difficult to be realized. Further, mounting two acquisition systems gives rise to the problem of cross-scatter contamination – scattered radiation from tube A is detected in detector B and vice versa [35]. The cross-scatter contamination causes artifacts, reduces the contrast-to-noise ratio (CNR) of the image [36], and has a negative impact on the dual-energy analysis of the acquired data. One

method of correcting for this contamination is to directly measure the cross-scatter radiation and later subtract the amount from the measured signal [32, 37]. While this reduces the effect of cross-scatter radiation, it does so at the expense of noisy images and lower CNR, which in turn implies more radiation dose to compensate for the low CNR.
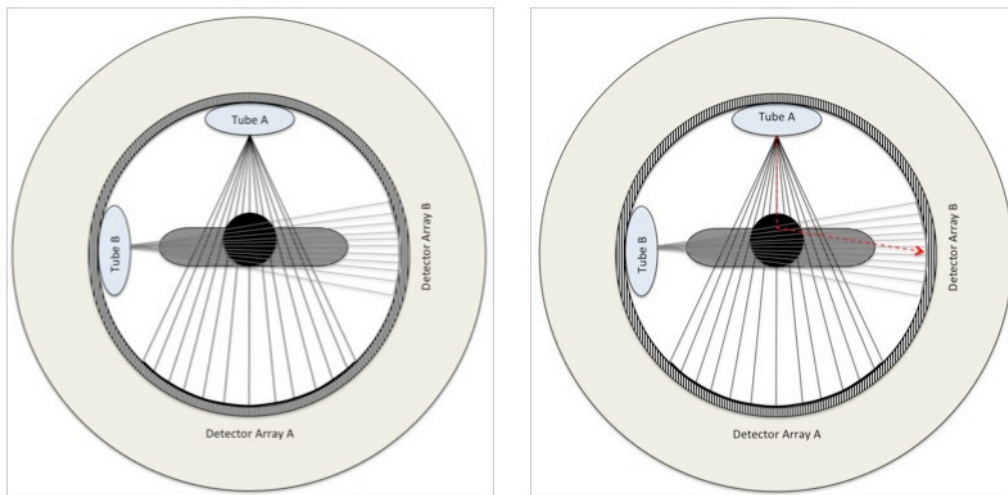
Figure 3.4: Left: A schematic diagram of a dual-source CT (DCST) system. Two separate acquisition systems are fitted into a single gantry. Due to the limited space, one system has a smaller detector array than the other. Right: The dashed line shows cross-scatter contamination, in which scattered radiation from tube A is detected in the detector B.

Dual-Layer (Sandwich) Detector

Instead of using different X-ray spectra for the realization of dual-energy imaging, another method is to use energy-resolving dual-layer detectors. Dual-layer detectors still use conventional scintillation detectors, but are distinctive from other detectors in that they have two sets of scintillation arrays and photodiodes stacked on top of each other [32]. In this setup, lower-energy photons are absorbed by the top scintillator array, while the higher-energy photon penetrates the top layer and are absorbed by the bottom scintillator array [38].

The use of dual-layer detector has several advantages to the other DECT methods. Firstly, upgrading current CT systems to enable dual-energy imaging only involves upgrading the existing detector module to one with dual-layer capabilites. Secondly, dual-energy data acquisition can be done using standard CT parameters at full FOV and can be optimized for the type of examination. This is important as

radiation dose savings can be achieved by adapting the image acquisition to the patient's needs and physical attributes. Thirdly, due to the simultaneous acquisition of low- and high-energy projection datasets, they are perfectly aligned making it possible to detect early phase of contrast concentration changes [39]. Further, since the acquisition of both projection datasets are consistently done at the same angle, raw-data based dual-energy analysis can be directly done without the need for interpolation. And lastly, due to the single acquisition system, the problem of cross-scatter contamination will not arise [32, 39].

Despite of these advantages, the biggest drawback of dual-layer detectors are the poor spectral separation in comparison to techniques that utilize different X-ray spectra [40]. Although the top layer is meant to absorb lower-energy photons, there is a high possibility for higher-energy photons being absorbed on the same layer. Figure 3.5 illustrates the phenomenon of huge overlap between the low- and high-energy spectra.
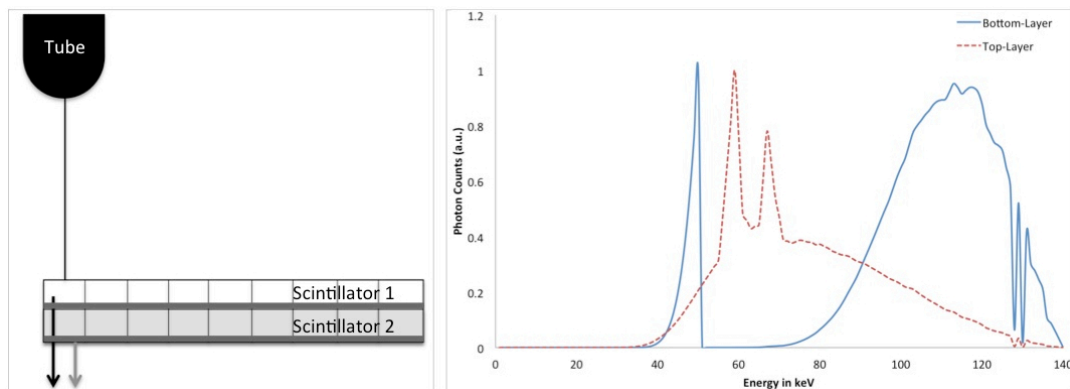
Figure 3.5: Left: A sketch of a dual-layer detector with a single source. There are two scintillators stacked on top of one another. The top layer absorbs the lower-energy photons, the bottom layer the higher-energy ones. Right: The spectral profile of the top- (dashed line) and bottom-layer (solid line) material irradiated with a 140kV spectrum. The top-layer is made of 1mm ZnSe and the bottom layer of 2mm of gadolinium oxysulfide (GOS). The overlap goes over the entire spectral range.

3.1.3 Clinical Applications of DECT

The advantage of having additional spectral information has spurred the development of many new applications that add diagnostic value to clinical CT. These new applications do not only help clinicians make accurate and reliable diagnostic decisions in real time, but also open new avenues to more specific treatment planning [41]. One such application of DECT is the differentiation of kidney stone. Basically,

there are three clinical relevant types of renal stones: calcified stones, uric acid and struvite stones [8]. Uric acid calculi can be easily dissolved with urine alkalization, but calcified and struvite stones can only be removed mechanically or crushed using shock wave therapy. Therefore, the accurate identification of these renal stones, as shown in Figure 3.6, is essential for the treatment of patients.
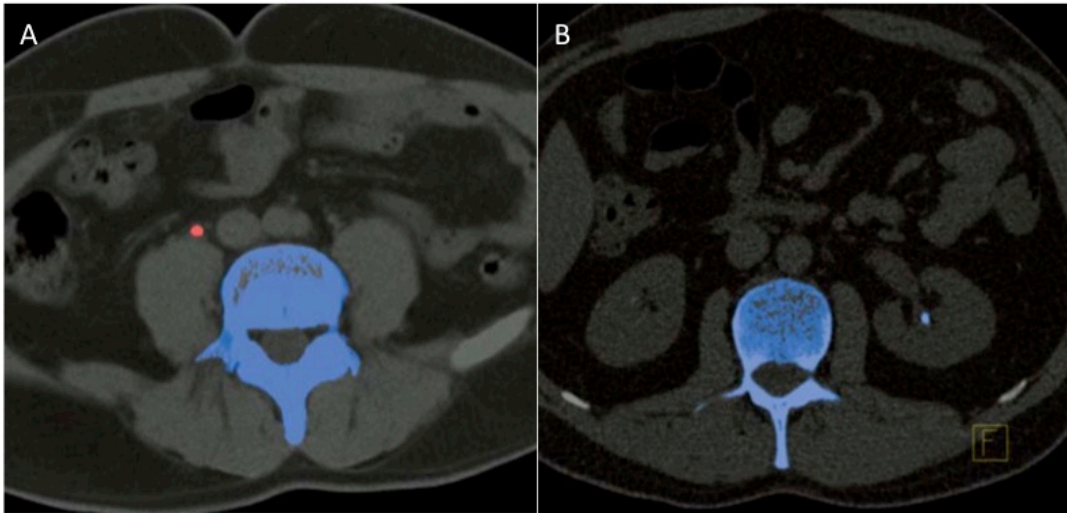
Figure 3.6: Some examples of dual-energy applications. DECT imaging enables the detection and characterization of renal stones. Image A shows a renal stone characterized as uric acid stone (color-coded in red), while image B as calcified stone (color-coded in blue). All images were taken from the Siemens Healthcare webpage.

3.2   Material Decomposition

Datasets acquired by DECT systems contain additional spectral information and can be used and processed in several different ways. One of the known methods is to decompose the datasets to several basis materials that constitute the components of the scanned object. The material decomposition technique can be applied either on the reconstructed images (image-based decomposition) or on the raw data (projection-based decomposition). Decomposition on the reconstructed images can be done by solving a system of linear equations [42], analysis of 2D histogram measurements, or calculating the difference between the low- and high-energy images. On the other hand, decomposition on the raw data can be implemented using the maximum-likelihood estimator (MLE) [43], the A-table method [44], or the empirical dual energy calibration (EDEC) [45] method. Generally, the image-based methods are easy to implement and usually produce results in a short period of time. In contrary, the projection-based methods are more complex, slow, and computational expensive, but

produce superior image quality than image-based methods. A summary of widely known methods for material decomposition is given in Table 3.1. It has to be noted that the list is by no means exhaustive.

Table 3.1: A summary of methods for image-based and projection-based decomposition.

Image-Based Decomposition	Projection-Based Decomposition
Solving a system of linear equations	Maximum-likelihood estimator (MLE)
2D histogram analysis	A-table method
Difference image	Empirical dual energy calibration (EDEC)

3.2.1 Image-Based Decomposition

In this work, the image-based decomposition is achieved by solving a system of linear equations. The reconstructed images from the scanner (DICOM-formatted images) are used as input for the decomposition. First, the reconstructed images are transformed from the Hounsfield Units (HU) scale to the linear attenuation coefficients. The Hounsfield units can be written as:

$$HU = 1000 * \frac{\mu_X - \mu_{water}}{\mu_{water}} \qquad (3.1)$$

where μ_X and μ_{water} are the average linear attenuation coefficient and linear attenuation of water respectively.

The inverse transformation is done for both high- and low-energy scans. Then, the rescaled images are decomposed into two materials, e.g. water and iodine, to determine the local concentration A_i of the material by solving the following equation.

$$\begin{bmatrix} f_{1_{E1}} & f_{2_{E1}} \\ f_{1_{E2}} & f_{2_{E2}} \end{bmatrix} * \begin{bmatrix} A_1 \\ A_2 \end{bmatrix} = \begin{bmatrix} L_{E1} \\ L_{E2} \end{bmatrix} \qquad (3.2)$$

where

$$f_i(E) = \frac{\mu}{\rho}(E) * \rho$$

A_i is the local fraction of the material, $L_{E(i)}$ the linear attenuation coefficient of the input images, μ / ρ *(E)* is the mass attenuation coefficient at energy E, and ρ the

density of the material. As the X-ray spectra have photons with a wide range of energies, the effective energy E_{eff} of each spectrum is used as E.

3.2.2 Projection-Based Decomposition

In projection-based decomposition technique, the composition of known materials in the scanned object can be obtained from at least two CT measurements. In the presence of two known materials, the measurements with two different source spectra can be written as [1]

$$I_1(A_1, A_2) = \int S_1(E) exp[A_1(\vec{x})f_1 + A_2(\vec{x})f_2]dE$$

$$I_2(A_1, A_2) = \int S_2(E) exp[A_1(\vec{x})f_1 + A_2(\vec{x})f_2]dE$$

(3.3)

where I_i is the intensity measurements, $S_i(E)$ the photon number spectra, A_i the line integrals of the material coefficient and f_i the mass attenuation coefficient of the material.

In order to estimate the line integrals of the individual materials A_i, a number of parameter estimation techniques can be used, such as the least-squared method or maximum-likelihood method. In this work the maximum-likelihood parameter estimation method derived from a Poisson distribution model is used. A detailed explanation is given in the Chapter 4.

3.3 Clinical Application (I) – Beam Hardening Correction

The polychromatic nature of X-ray source used in CT causes beam-hardening artifacts [14, 46]. As photons penetrate through an object, more low energy photons are readily absorbed, resulting in a shift of the X-ray spectrum to a higher energy range. This causes two types of artifacts: cupping artifacts and dark streaking between dense objects [46, 47]. One way of overcoming this problem is to use a monochromatic X-ray source. However, this is not practical in clinics as such kind of radiation can only be generated in a large synchrotron. Another possible way to reduce the effects of beam hardening is to use the decomposed images to produce virtual monochromatic images of the scanned object.

3.3.1 Virtual Monochromatic Images

Virtual monochromatic images (VMI) are images that are produced as if the images are acquired using monochromatic sources. The VMI can be generated from the decomposed images for different energy levels. For the image-based decomposition, the calculation is done by summing up the products of the local density of the individual materials and their linear attenuation coefficients at energy E.

$$L(E) = A_1 * \frac{\mu_1}{\rho_1}(E) * \rho_1 + A_2 * \frac{\mu_2}{\rho_2}(E) * \rho_2 \tag{3.4}$$

For the projection-based decomposition, the calculation is carried out in the projection space itself. This is done by summing up the products of the line integrals of the individual materials and its mass attenuation coefficients at energy E.

$$\mu(\vec{x}, E) = A_1(\vec{x}) * \frac{\mu_1}{\rho_1}(E) + A_2(\vec{x}) * \frac{\mu_1}{\rho_1}(E) \tag{3.5}$$

After this step, the projection data is reconstructed using a conventional filtered back-projection (FBP) reconstruction.

3.3.2 Description of Experiment

The effectiveness of both image-based and projection-based material decomposition methods in distinguishing different materials was evaluated. Further, the amount of reduction in beam hardening was also visually and quantitatively assessed.

In this investigation, retrospective datasets from five patients subjected to ultra-low-dose dual-energy scans and administered with iodine were used. These patients were scanned on a Siemens SOMATOM Definition Flash (Siemens Healthcare, Erlangen, Germany) operated in dual-source mode at 80kVp and 140kVp. Both the image-based and the projection-based material decomposition techniques were applied to all the datasets. Further, using the decomposed images, VMI were generated at 120 kV. The choice of 120 kV was made, as this is the standard tube voltage used in most clinical CT applications.

The problem with the different FOV between the low- and high-energy datasets was avoided by applying a padding scheme to the smaller projection dataset. In this scheme, the outside of the smaller projection dataset is padded with values from the larger one in order to have projection dataset of a similar size for both. This scheme was only applied to the projection datasets, as the reconstructed images from the scanner were of the same size for both low- and high-energy acquisitions.

3.3.3 Results

Figure 3.7 shows the decomposed images obtained from both methods. One can see that both decomposition techniques are able to separate iodine from other materials. On closer inspection, bone is wrongly classified as iodine in the image-based method, but in the projection-based method the appearance of bone is not as distinctive. This suggests that the projection-based method has a better material separation capability in comparison to the image-based method. Note that the projection-based images appear to be noisier than the image-based method. This is due to the different kernel feature of the FBP image reconstruction process. The image-based technique uses images from the scanner, which are reconstructed using proprietary software and incorporates more information on the imaging system, such as the detector efficiency. On the other hand, the projection-based reconstructions are done using in-house developed general-purpose image reconstruction software.
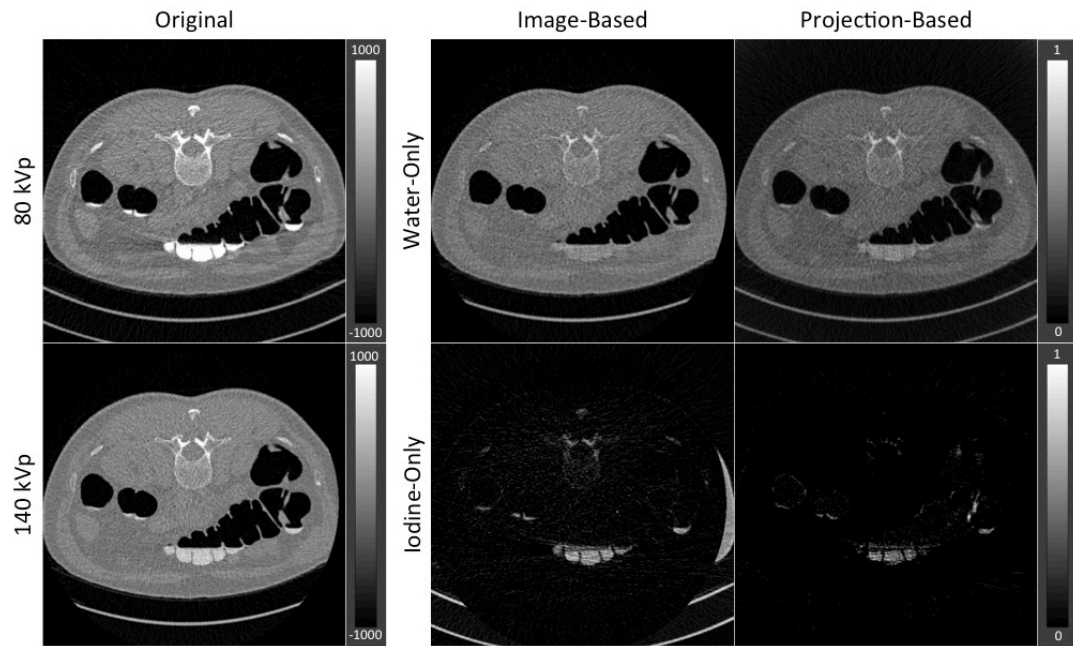
Figure 3.7: The decomposed images from the both the image-based and projection-based methods. Both decomposition methods are able to detect iodine. However, the bone is wrongly classified as iodine in the image-based method whereas the projection-based method works almost correctly. The original images are windowed with WL of 0 and WW of 2000. The material decomposed images are normalized to 1 and illustrated with WL of 0.5 and WW of 1.0

Figure 3.8 shows the VMI obtained from both decomposition methods. One can observe that the VMI at 120 kV shows less beam hardening in the images in comparison to the original image acquired at 80kVp. An analysis of the line profiles suggests that the VMI better reflects the theoretical value of soft tissue (~0 HU). Further analysis of the plot indicates that the projection-based technique delivers better results than the image-based technique, as shown by the constant HU value, indicating less beam hardening-induced CT number variations in the image.
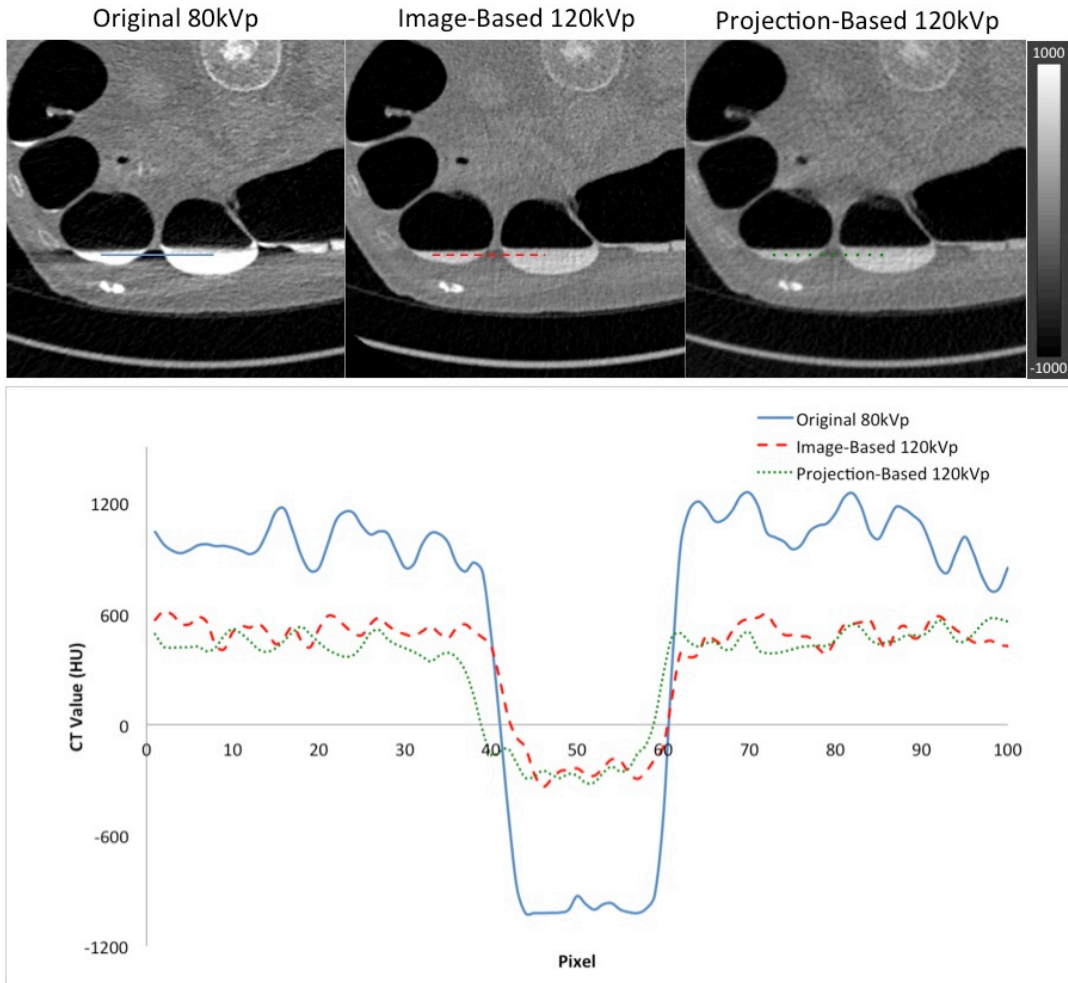
Figure 3.8: An original CT image at 80kVp and the corresponding VMI at 120keV generated using both image-based and projection-based techniques. Visually, one can see the reduction of beam-hardening artifacts in the VMIs. The line profile shows that, quantitatively, the projection-based method is less noisy and better reflects the true value than the image-based technique. Images on the top row have WL of 0 and WW of 2000.

The choice of energy influences the outcome of the VMI generated. At a high energy level, the effect of beam hardening due to the presence of high-attenuating material such as iodine can be significantly reduced; however, the drawback of generating images at a high energy is that the contrast in the image gets reduced. Figure 3.9 illustrates this phenomenon. At 80kV, one can see that the image has more soft-tissue contrast than the ones at 120kV and 140kV as indicated by the solid arrow, but more streaks due beam hardening artifacts are also observed, especially around the area shown by the dashed arrows.
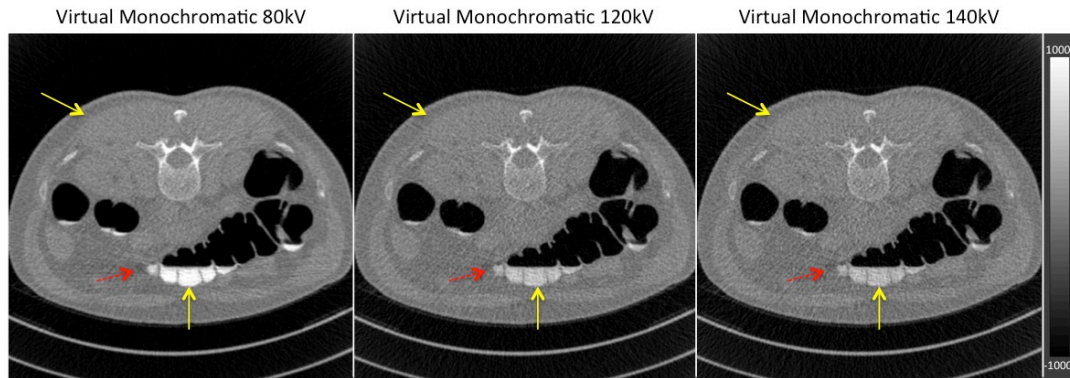
Figure 3.9: VMI generated at different energy levels. One can observe that at higher energy levels, beam-hardening artifacts due to the presence of iodine is minimized as shown by the dashed arrow (in red), but at the same time the contrast in the image is also reduced as can be seen by the solid arrow (in yellow). All images have WL of 0 and WW of 2000.

3.4 Clinical Application (II) – Improving CAD Performance in CT Colonoscopy

CT colonoscopy (CTC) is a procedure used for experimental screening of colorectal cancer [48, 49]. In this clinical procedure, patients are administered with contrast agents and then scanned with two different X-ray spectra (typically 80kVp and 140kVp). From these two X-ray spectra, a virtual unenhanced image can be produced. The combination of the contrast-agent enhanced and virtual unenhanced images is able to assist the detection of polyps, especially the ones obscured by residual fecal material in the colon.

CTC with the combination of computer-aided diagnosis (CAD) is able to distinguish small polyps from feces, which are otherwise difficult to detect. While CAD has been reported to be able to detect lesions with high sensitivity [50, 51], the success of this technique depends highly on the quality of the input image. The use of contrast agent such as barium and iodine causes beam hardening artifacts that leads to inconsistencies in CT values, especially around the polyps [52]. The presence of the beam hardening artifacts can severely affect the detection performance.

In this preliminary study, the CAD performance for segmentation of colon and the detection of polyps is evaluated. Three types of input images were investigated: reconstructed images from the scanner (hereafter called original images), image-based VMI, and projection-based VMI.

3.4.1 Description of Experiment

A total of 20 patients underwent ultra-low-dose CTC scanning using Siemens SOMATOM Definition Flash (Siemens Healthcare, Erlangen, Germany) operated in dual-source mode at 80kVp and 140kVp. Each patient was prepared for CTC by use of reduced bowel cleansing and orally administered fecal tagging with iodine and was scanned twice, once in supine position and once in prone position.

The dual-energy datasets were first decomposed into two basis materials – water and iodine – using the image-based and projection-based decomposition techniques. Then, image-based VMI and the projection-based VMI were generated at 120 kV. The VMI images were then used as inputs to a virtual CT colonoscopy CAD Program (Philips IntelliSpace Portal, Philips Healthcare, Best, The Netherlands).

3.4.2 Results

In general, the CAD program using original images, as well as both image-based and projection-based VMIs as input was able to segment the colon from other organs in the body as shown in Figure 3.10 (A) and (B). But in the axial slices, the VMI images deliver better segmentation result in comparison to the original image. This is evident in images C-E. The poor quality of the original image in C results in areas being wrongly classified as the contrast agent (pointed by the solid arrows), and thus is not included in the cleansed image.
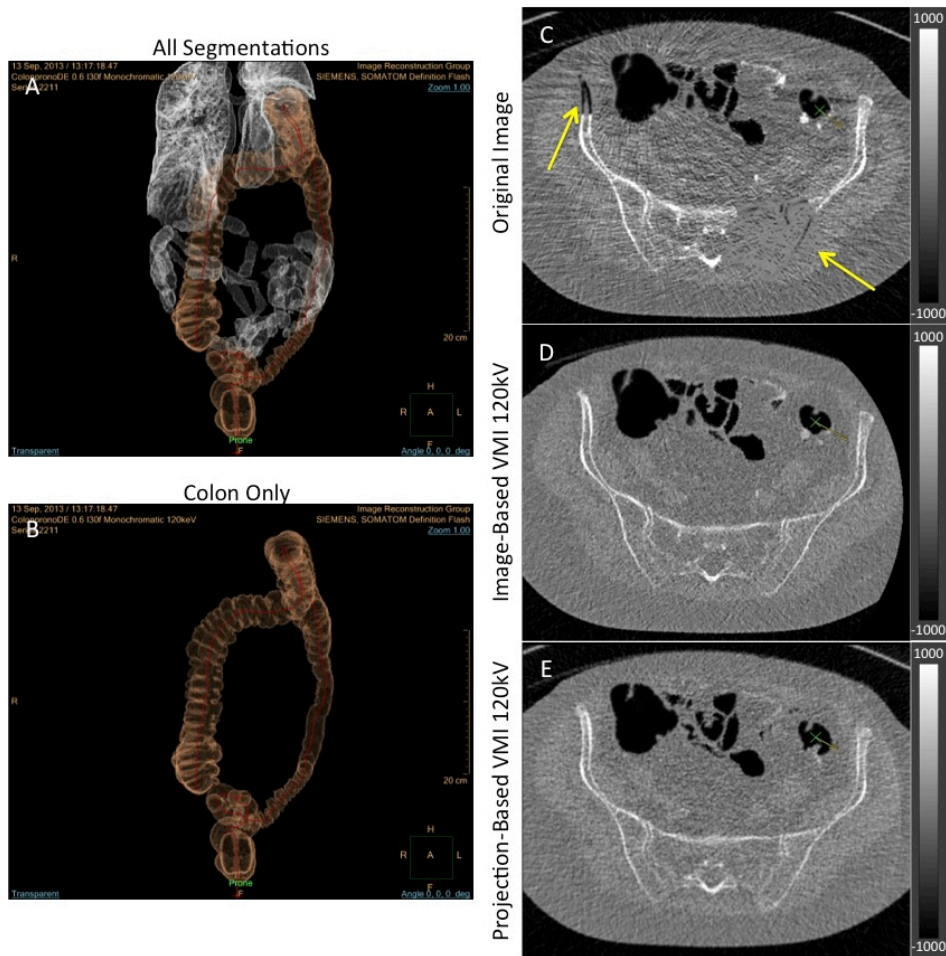
Figure 3.10: The results of the segmentation done by the CAD program using projection-based VMI as input. Image A shows all successfully segmented organs, while in image B only the colon is selected. The second column shows the axial view. Some parts of the image are wrongly segmented in image C as pointed by the arrow. This is due to the poor input image quality. The results are much better for VMI images (D and E). The axial images have WL of 0 and WW of 2000.

Further analysis suggests that the beam hardening artifacts have a negative impact on the performance of the CAD program. Figure 3.11 shows images in presence (uncleansed) and in absence (cleansed) of iodine. The solid arrow in image C shows part of the iodine solution that is wrongly classified as the colon tissue. The beam hardening artifacts were corrected in the generated VMI images as can be seen in image C. This also results in a correct segmentation of the colon shown in D.
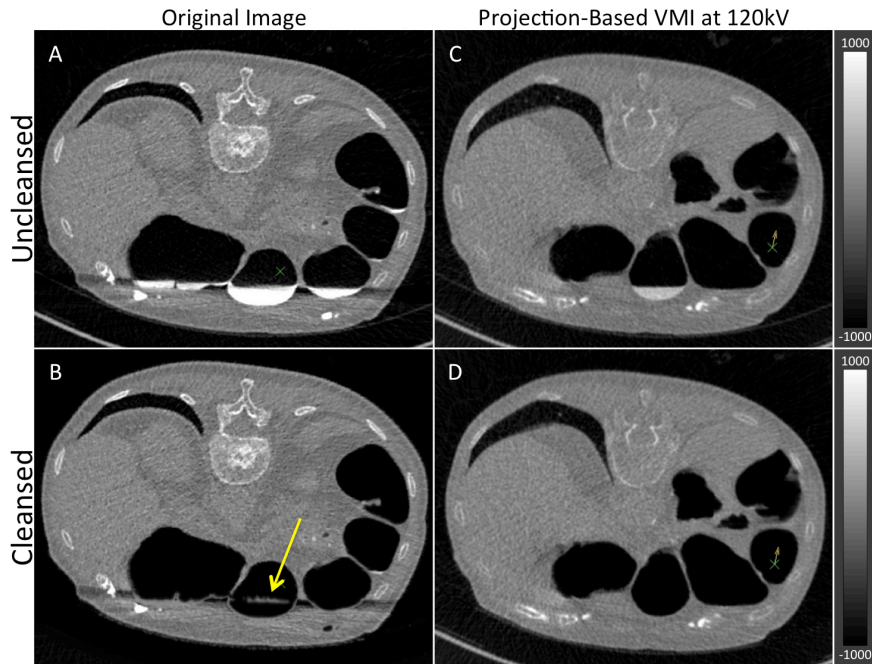
Figure 3.11: Axial images of uncleansed and cleansed colon using input from original images (first column) and generated VMI (second column). In image A, severe beam hardening can be seen around the iodine. This causes problems in the CAD segmentation of the colon resulting in the wrong classification of iodine in the cleansed image as pointed in image B. The VMI (image C) has better image quality; thus misclassification does not occur, as evident in image D. All images have WL of 0 and WW of 2000.

In order to evaluate the potential improvement by the VMI images in improving CAD performance, a CAD system [53] was used to detect lesion candidates automatically from the prone VMI datasets of 6 patients out of the 20 patients scanned, where 5 of the patients had a colonoscopy-confirmed polyp ≥6 mm in size. The detection sensitivity of CAD was 100% with both VMI methods. Furthermore, the CAD system calculated several three-dimensional image-based features from the extracted regions of lesion candidates to be used for the reduction of false positives. To measure the performance between VMI techniques, the area under receiver operating characteristic (ROC) curve for the discrimination performance of the CAD features was calculated. Table 3.2 demonstrates the discrimination performance in terms of the area under the ROC curve, A_z, for the mean of CT value, which is expected to be sensitive to the quality and consistency of input image. The generally higher values of the A_z with the projection-based method indicate that the use of the projection-based method makes it possible to discriminate true-positive and false-positive polyp candidates more accurately than the use of the image-based method. This also suggests that the CAD may have higher and more consistent

detection performance using the VMIs from the projection-based method than from the image-based method.

Table 3.2: Evaluation of the area under the ROC curve (A_z) of the CT value feature in the discrimination of true-positive and false-positive CAD detections. Higher values of the A_z indicate higher performance.

Energy of VMI Images (kV)	Area under the ROC curve (A_z)	
	Image-Based VMI	Projection-Based VMI
80	0.53	0.52
100	0.51	0.65
120	0.54	0.61
140	0.50	0.66

3.5   Discussions

Material Decomposition Technique

One of the methods for processing data acquired using DECT systems is to decompose the dual-energy datasets to several basis materials that represent the components of a human body. In this chapter, it is shown that iodine can be distinguished from other components of the image such as the adipose tissue, soft tissue and bone. This finding has several clinical benefits. For example, the detection of iodine can help detect diseased tissues or tumor in contrast-enhanced CT examination. Some diseased tissues such as lesions and polyps are known to absorb iodine more rapidly than healthy tissues, while at the same time do not excrete the iodine as fast as the healthy ones. Hence, the iodine-decomposed image may assist clinicians in detecting diseased tissues in patients. Further, the decomposed iodine image can be combined with the original image to produce color-coded images that will aid the diagnostic process of patients.

Two types of material decomposition techniques have been demonstrated – image-based decomposition and projection-based decomposition. In the image-based method, decomposition is done on reconstructed images. This is a particular advantage as such images are readily available in most clinics, thus the image-based method can be easily applied. Further, it is fast and the results are reliable and accurate. Single-slice decomposition takes less than a minute to complete and does

not require expensive computational power. Theoretically, a pair of dual-energy datasets can be decomposed to up to three basis functions if additional constraints are introduced into the equation 3.2 [42]. However, the decomposition to more than two basis functions for a pair of low- and high-energy datasets was not used in this work as such decomposition usually results in noisy decomposed images and less accurate differentiation of materials.

The image-based method has several limitations. First, the differentiation of materials is not as good as in the projection-based method, as shown in Figure 3.7, in which bone is also detected in the iodine-only image. Second, the decomposition quality is limited to the quality of the image used as input. Noisy images have a negative impact on the decomposition of the material and thus result in less than desirable detection results. Third, the difference in FOV between the two datasets poses additional problems in that only materials in the FOV can be decomposed, as shown in Figure 3.12. This is particularly challenging in decomposing images of larger patients and from off-center acquisitions.
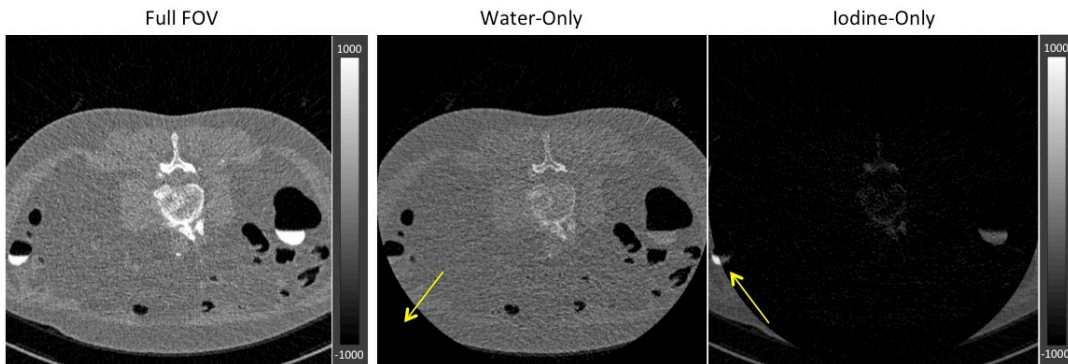
Figure 3.12: The effect of different FOV on the image-based material decomposition technique. Outside the FOV, materials cannot be accurately decomposed as pointed by the solid arrow. All images have WL of 0 and WW of 2000.

It can be said that the projection-based method delivers better decomposition results in comparison to the image-based method. It has better material separation ability and can correctly distinguish two highly dense materials such as bone and iodine. The decomposed images are also less noisy owing to the fact that this method takes into account the accurate physical modeling of the acquisition system. Further, the projection-based method is able, to some extent, overcome the limited FOV problem of the image-based technique. This is due to the padding scheme used on the

smaller projection dataset. However, it must be mentioned that the padding scheme is not only physically incorrect because of the energy-dependent nature of dual-energy acquisitions, but also may not work for all dual-source datasets. It is believed that the padding scheme works in the datasets used in this study by virtue of the normalized values in the raw-data (projections). Nevertheless, one can still observe residue lines in the images, as pointed by the solid arrow in Figure 3.13.
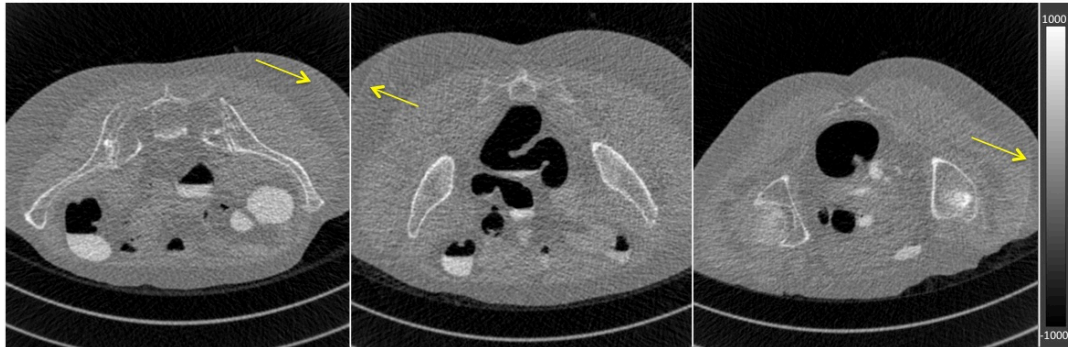
Figure 3.13: The residue lines from the effect of padding of the projection data. The non-linearity of the transmission data between the low-energy and high-energy data means that it is impossible to correctly pad the data. All images have WL of 0 and WW of 2000.

Despite the superiority of the projection-based method, it also has some limitations. In particular, it is slow and computational expensive. The decomposition of a slice may take up to several minutes, although employing parallelization techniques can accelerate the decomposition. Besides, the method requires the exact modeling of the acquisition process in order to yield the best result. For example, information on the X-ray spectrum, detector response, and the shape of the filter should be included in the acquisition model, but these details are not widely available and may be proprietary. The difficulty in obtaining such information and in accessing the raw data from the scanner has made the projection-based technique difficult to be widely applied.

The use of DECT data generated from dual-source CT (DSCT) may pose several complications to both material-decomposition techniques. First, the cross-scatter contamination can to some extent negatively impact the quality of the images and subsequently the effectiveness of the material decomposition, if corrections are inadequately done. Second, the simultaneous dual-energy acquisition and table movement can lead to line integrals from the low- and high-energy datasets to be

misaligned for the same slice of the object. This effect is especially worse if the table pitch is high or if there is movement in the scanned object. The misalignment between the datasets can either be minimized by reducing the table pitch or corrected by interpolating the datasets for a given slice position. However, the interpolation of datasets may not reflect the true line integral measurements of the slice position, which may result to less effective material decomposition.

Beam-Hardening Correction

Generation of a VMI has, to some extent, reduced the presence of beam hardening artifacts in the image; thus improves the overall image quality as shown in Figure 3.8. These images can be produced at any energy level in the diagnostic energy range. At higher energy, a higher reduction of beam hardening can be seen. However, the choice of energy level also influences the contrast of the image. One can observe from Figure 3.9 that while fewer beam-hardening artifacts can be seen at higher energy levels, the soft-tissue contrast is also reduced. Therefore, a right balance between beam hardening reduction and contrast has to be taken into consideration in selecting the energy level for generating VMI.

CAD Performance

The CAD CTC performance depends heavily on the quality of the input images. In the presence of severe artifacts such as beam hardening, the CAD program was not able to correctly distinguish the colon from other organs and materials such as bone and iodine. This has the consequence that in the presence of artifacts polyps and lesions may remain hidden, which may impede their detection. Therefore, it is essential for the CAD program to have input images that are superior in quality and artifact-corrected.

In comparison to the original images obtained directly from the scanner, the generated VMI images have shown to deliver better image quality and achieve notable reduction of beam-hardening artifacts. This raises the question, which of the two types of VMI will yield the best result with moderate effort. Comparison between the image-based and the projection-based VMIs suggest that the latter produces less false-positive detection than the former. But the generation of projection-based VMI is time-consuming and requires information and data that is not widely available.

Therefore, one can argue that the best compromise is to use the image-based method. It is fast and is readily available as the images are generated from the DICOM images. While the quality of the DICOM images can negatively impact the generated VMI, there are several workarounds to overcome this image quality problem, for instance, by iteratively reconstructing the image or using special filters such as bilateral filter [54]. Initial study on the use of bilateral filter for noise reduction has shown promising results (see Figure 3.14) and should be considered for future studies.
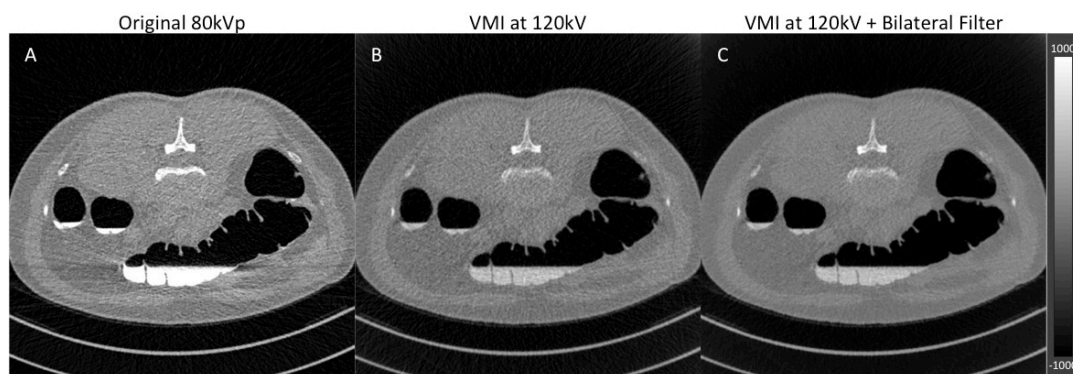
Figure 3.14: Noise reduction achieved by a bilateral filter. In comparison to the original (A) and the VMI (B) image, the application of bilateral reduces the appearance of noise, resulting in a better tissue contrast as seen in C. All images have WL of 0 and WW of 2000.

3.6 Summary

Dual-energy CT (DECT) imaging offers additional information that is otherwise not available in a single-scan acquisition. This additional spectral information can be processed in several ways and the result of the processing can be used to enhance image quality and aid clinicians in the diagnostic process. This chapter shows that the dual-energy datasets can be decomposed into several basis materials that constitute the different component of the scanned subject. The decomposed images can then be used to produce virtual monochromatic images that have been shown to reduce the appearance the beam-hardening artifacts in CT images. Such artifact-free images are desirable especially for the use in CAD software used in CTC, as it enables the accurate detection of lesions and small polyps in the bowel that are challenging to detect.

Chapter 4

Spectral CT

4.1 Introduction

In current Computed Tomography (CT) systems the X-ray beam consists of a spectrum of energies. Contrast in the reconstructed image is a result of averaging over the effects of (absorption at) these various energies. In this regard, the spectrum of energies can be seen as a disadvantage to the image contrast because the lower energy photons that carry with them information on the contrast are lowly weighted in comparison to higher energy photons. However, the same spectrum of energies can be an advantage when using detectors that are sensitive to specific energy ranges. One example is the energy-resolving photon counting detector (PCD).

4.2 Detector Technology

Advancements in detector technology have contributed to the development of energy-resolved photon counting detectors (PCDs) [55-57]. PCDs have the ability to discriminate incoming photons based on their energies; hence spectral information of the object can be obtained in a single scan at the same tube voltage [58, 59]. In this technique also known as Spectral CT (SCT) imaging, PCDs split the X-ray spectrum into several pre-defined energy bins, enabling the acquisition of separate CT data in each energy bin.

As the main component, PCDs have the ability of counting single photons and discriminate the photons into pre-defined energy bins based on their incoming energies. These discriminated photons carry with them the spectral information, which provides additional absorption information on the composition of the scanned object [60].
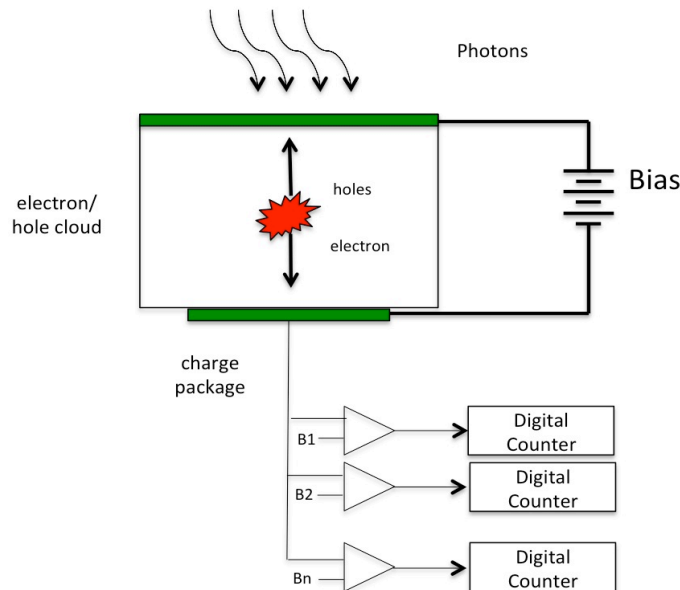
Figure 4.1: A schematic diagram of a photon-counting detector (PCD). The detector sensor absorbs incident photons, producing charge cloud of electrons and holes. The voltage bias applied causes the charges to be drifted to their respective electrodes. Electrons at the anode generate impulses, which are detected and counted by the digital counters.

In a conventional detector, incident photons are converted to optical photons at the scintillator. The amount of light created in the scintillator is proportional to the energy of the X-ray photon. The higher the energy, the larger the amount of optical photons produced; thus the energy weighting scheme is advantageous to the higher energy photons. Further, the photon detection process, conversion to electrical signals, and the subsequent amplification of the signals are inefficient, while the digitization process may induce some noise in the signal sampling.

On the other hand, PCD counts single photons, thus is already discrete in nature. This has several advantages. Firstly, electronic noise can be excluded from the measurement process by introducing thresholds above the highest amplitude of the noise. Due to the 'absence' of electronic noise at the detector, low radiation dose acquisition protocol is possible without compromising the quality of the CT image [61]. Secondly, low energy photons that contain valuable contrast information can be correctly detected. In an energy-integrating detector, low-energy photons may get 'mixed' with electronic noise. Further, due to the integration process over time, the low-energy photons are lowly weighted to the higher-energy photons [62]. However, in energy resolving single photon-counting detector such problem does not arise, thus valuable information contained in the low-energy photons can be preserved.

4.3 Data Acquisition Methods

In this work, two types of data acquisitions methods were used: the generation of projection data from PCDs using simulations and data acquisitions using Medipix3RX, a experimental PCD predominantly used in laboratories for various developmental purposes.

4.3.1 Simulation

Despite the many advantages of PCD, there are still many technical hurdles such as pulse pile-up [63, 64], detector pulse splitting [65], limited energy resolution [43, 56], and charge sharing problems [43] that need to be addressed before Spectral CT scanners equipped with PCD can be introduced into the clinical arena. Due to these reasons, two software packages that allows for simulation of a Spectral CT system equipped with a PCD were developed. They are Analytical Simulation (AS) and the more complex Monte-Carlo based Simulation (MCS).

Analytical Simulation

The analytical simulation (AS) is the forward projection of the phantom image at every energy level up to the peak energy [66]. The attenuation coefficient of the phantom image at each energy level is pre-calculated from the NIST website. In the projection process, parameters that characterize a clinical CT scanner such as the X-ray spectrum are taken into account. Additionally, Gaussian noise is added to the projection data. The simulation was done at 1keV steps, and the bins were later summed up to create several energy windows. A simulation using this technique takes several minutes to complete.

Monte Carlo Simulation

A more complex method of simulation is by using Monte Carlo (MC) simulations. The MC method is widely used in radiation therapy to simulate electron and photon transport throughout the body. It is used to calculate energy deposition from photons (or electrons) in different parts of the body, thus enabling radiotherapy to estimate the dose distribution at a particular target area for cancer treatment planning [67]. In recent years, MC simulations gained in popularity to simulate photon transport in X-ray imaging, with the main purpose of image quality assessment and new detector configuration development [68]. With accurate

modeling of the underlying physics and the incorporation of appropriate cross section data, MC methods provide in-depth assessment and accurate means of predicting radiation transport inside materials with complex geometries [68, 69]. Previously published works include the simulation of diagnostic X-ray tubes [69, 70], modeling of attenuating medium or phantom [71], study of X-ray scatter distribution [72], and simulation of X-ray detectors [64, 65, 73]. All of these work points to the reliability of MC technique as a tool to simulate real clinical imaging systems.

The EGSnrc is a general purpose Monte Carlo package that can be used to simulate the transport of photons and electrons in any arbitrary geometry for particles in the energy range of 1 keV to 10 GeV [74, 75]. In this study, the egs_cbct [76] MC simulator, which is distributed as a part of the EGSnrc simulation package, were used. In general, it allows a fast calculation of scatter distributions on the detector plane while having also the option to output the real and ideal (signal only from primary photons) scans of a simulation. This MC simulator is capable of producing not only circular cone beam acquisitions but also any trajectory or detector configuration. For the purpose of this work, a spectral scoring option is implemented in the egs_cbct user code, which adds the possibility to use either an energy integrating spectral detector or a photon counting spectral detector. Furthermore, different variance reduction techniques (VRTs) [77] already implemented in the user code such as forced detection and fixed splitting were also used. The splitting numbers for the primary and scatter photons used for the fixed splitting technique are empirically determined and set to 70 photons and 120 photons respectively. Photons not aimed at the detector are eliminated according to a predefined probability (Russian Roulette). The surviving photons are then transported using delta transport to speed up the simulation. For the calculation of the mean free path, which is used in the delta transport of the photons, cross section data of the materials in the phantom are used, which balances speed up and accuracy. The use of these VRTs in the egs_cbct user code were validated by comparing the results with the ones of the egs_cbct without VRTs and found no significant difference. Further, to evaluate whether the MC tool can be used for simulating different radiation exposure levels and that the used VRTs are not compromising the result, two independent simulations were performed with full dose and quarter dose. For this specific purpose a homogeneous water phantom with 20 cm thickness was used. The resulting images were evaluated by calculating the signal to

noise ratios (Figure 4.2). The signal-to-noise ratio for the quarter dose was 4.20 and for the full dose 8.33. The ratio between both is 1.98 and corresponds well to the expected value of 2.00. This staging of the algorithm illustrated that the expected theoretical values can be reached when using VRTs.

In all simulations the Compton interactions are modeled in the impulse approximation [78], the photon cross section is taken from the XCOM tabulations [79] and all photons are tracked to an energy level of 1 keV. All electrons set in motion are immediately discarded and all their energy locally deposited. This is done to speed up the simulation process, as the simulation of electrons is time-consuming, although the effects of their interactions are negligible. Further, the Rayleigh scattering, atomic relaxations and the photoelectron angular sampling were turned on.
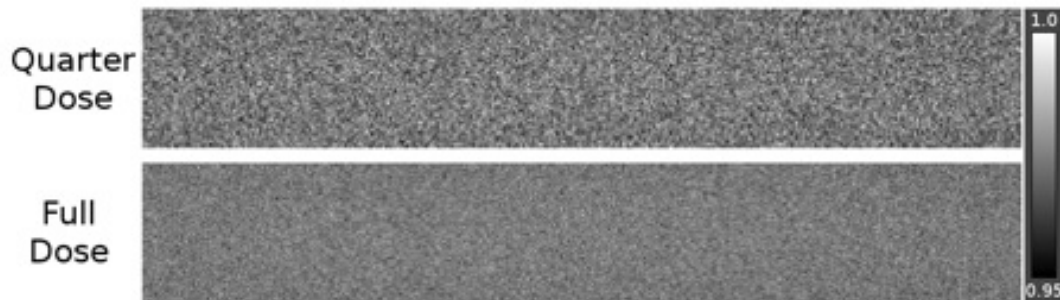
Figure 4.2: MC generated images at quarter dose level (top) and at full dose level (bottom). The signal-to-noise ratio in the quarter dose image is as expected half of the signal-to-noise ratio in the full dose image. The images are normalized to 1, with WL of 0.975 and WW of 0.05 as shown by the calibration bar.

Performance of Monte Carlo Simulator

In order to assess the performance of MCS, a modified version of the CTP515 module of the CatPhan 600 (The Phantom Laboratory, Incorporated, Greenwich, New York, USA) was simulated. The module is designed to measure low contrast sensitivity and consists of a series of cylindrical rods of various diameters and contrast-levels. Instead of three contrast-levels, the module was modified to have six different concentrations of iodine. Figure 4.3 shows the reconstruction of six individual energy bins; with energy thresholds set at 25 keV, 30 keV, 50 keV, 70 keV, 90 keV and 110 keV. One can see that at the energy window of 30 – 50 keV (B) the contrast targets exhibit strong attenuation due to the fact that the k-edge of iodine (33.2 keV) lies in this particular energy window. On the other hand, at higher energy windows (image E and F) the appearance of the iodine targets decreases, especially

the sub-slice targets (inner targets) that have lower concentrations of iodine due to the lower attenuation of high-energy photons.
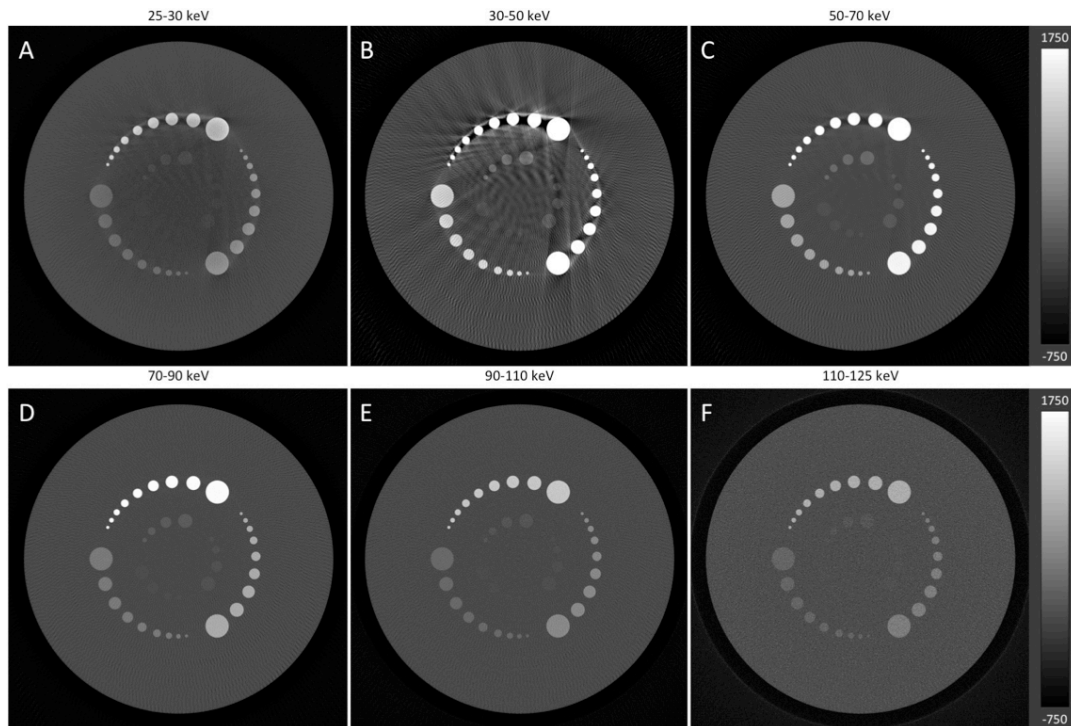
Figure 4.3: Reconstructed images from different energy window of X-ray spectra. All images were calibrated to Hounsfield units with window level (WL) of 500 HU and width of 2500 HU.

The presence of scatter does not only influence the quality of the reconstructed image, but also may have an impact on material decomposition techniques. One feature of the Monte Carlo simulator is the ability to simulate scatter-free (hereafter referred as ideal-scan) as well as full simulation with scatter (real-scan). Figure 4.4 illustrates the reconstruction of the 'real-case' scan (left column), the 'ideal-case' scan, and the difference of both images at different energy window. One can visually observe that the presence of scatter causes many streak artifacts and degrades the image quality. The effect of X-ray scatter is more obvious in the mid-range energy window, in which the attenuation of photons is stronger as illustrated in the second row. For the real scan (D), the streak artifacts are strongly visible, while in the ideal scan (E) the appearance of streak artifacts is significantly reduced. In addition, the presence of scatter reduces the contrast of the targets as shown by the black targets (negative values) in the difference images (third column). The calibration bar on the

right side of the figure illustrates the difference of HU unit between both sets of images.
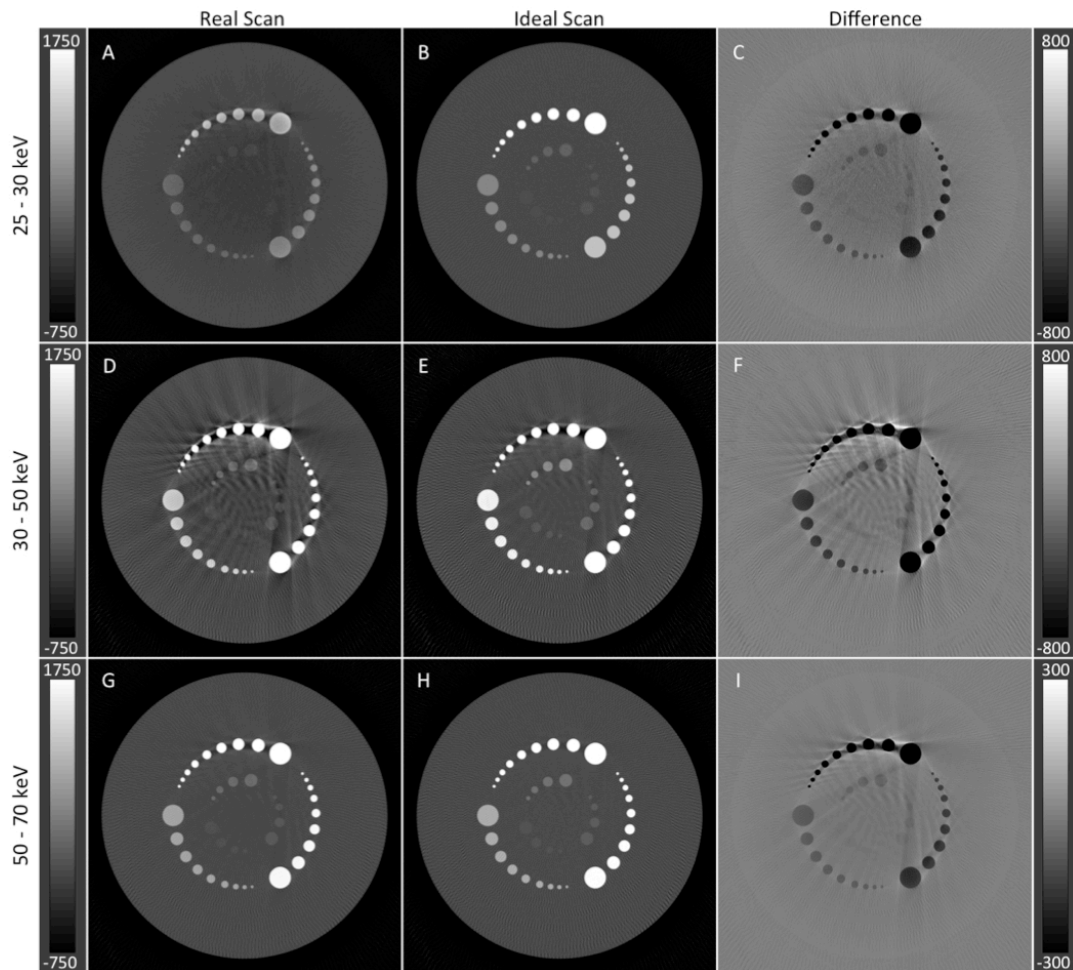
Figure 4.4: Reconstructed images from real-case (first column) and ideal-case (second column) scans at different energy windows (row-wise). The third column is the difference between the real- and ideal scan images. The presence of scatter reduces the contrast of the targets as shown by the black targets (negative values) in the difference images. The calibration bar on the right side of the figure illustrates the difference of HU unit between both set of images.

Analytical Simulation vs. Monte-Carlo Simulation

In the performance assessment above, the Monte-Carlo based (MCS) technique took about 120 hours for the 360 projections to be completed. For the same simulation, the Analytical Simulation (AS) method took about one hour, markedly faster than MCS. Figure 4.5 shows the reconstructed image from the MCS and the AS. At first inspection, one can see that the difference between those two images is only minor, with physical effects such as beam-hardening are more apparent in the

MCS than AS. However, when the AS image is subtracted from the MCS image, one can observe that the image intensity of MCS is less than AS. When quantified further, the discrepancy between those two images are 2-4%. The lower intensity of the MCS can be attributed to the more accurate and inclusive modeling of the MCS, such as the effects of scatter, in comparison to AS.
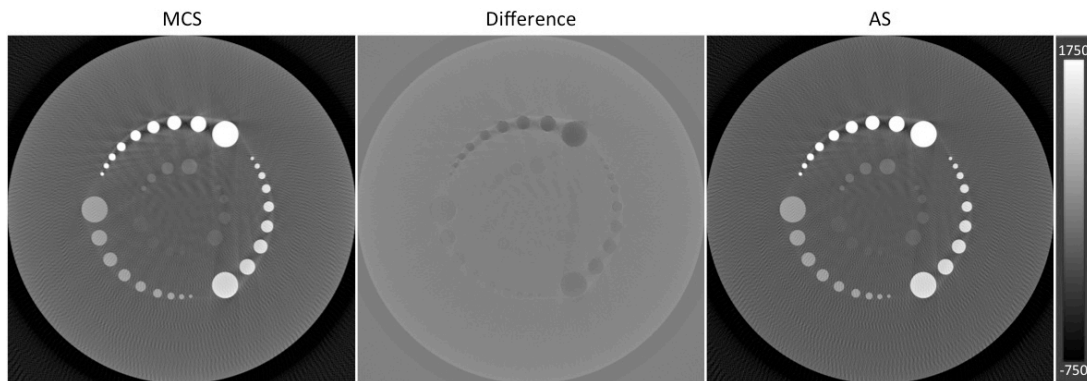
Figure 4.5: The reconstructed image from the projection data generated from the two different methods. The images are normalized and equally windowed, with WL 500 HU and WW 2500 HU. At first glance, one cannot see any difference between the MCS and AS. Only after subtracting the AS image from MCS, one can observe minor differences in the image. The differences in value between the two images are about 2 – 4%.

4.3.2 Medipix3 RX

The next method of acquiring spectral CT data is by employing the Medipix3 (Medipix3 Collaboration, CERN) detector, a single photon processing hybrid pixel detector. This detector chip is widely used in laboratories for experimental purposes and the development of preclinical applications such as targeted gold nanoparticle imaging [80] and luminal depiction in vascular imaging [81]. In this work, the Medipix3RX is used for the imaging of multi-material k-edge material in a single scan and to study the possibility of the differentiation of the materials per material decomposing technique.

The Medipix3RX chip's pixel matrix consists of 256x256 pixels with each pixel having a size of 55 x 55 μm^2. In total a maximum of eight thresholds can be set up, however, the availability of these thresholds depends on the operating mode of the pixels [82]. The pixels can be operated in either the 'Single Pixel Mode (SPM)' or in the 'Charge Summing Mode (CSM)'. In the SPM mode, the shaper outputs are connected only to the local discriminators, while in the CSM arbitration and synchronization logics are enabled to correct for charge sharing [82]. The pixel matrix

can be further configured to either work in Fine Pitch Mode or in Spectroscopic Mode. In the Fine Pitch Mode, every pixel is allowed to count independently with each pixel providing two counters. In this configuration, the pixel pitch size remains the same at 55μm; however the number of thresholds available is only limited to two. On the other hand, in the Spectroscopic mode, four pixels are grouped as a single cluster to provide more thresholds, but as a result the pixel pitch size becomes larger at 110μm, thus reducing the spatial resolution. A summary of the modes is given in Table 4.1.

Table 4.1: The different type of operating mode and the number of possible thresholds in each configuration. Table adapted from Ballabriga et al. [82].

Matrix Configuration	Pixel Operating Mode	Thresholds
Fine Pitch Mode	Single Pixel Mode	2
	Charge Summing Mode	1 + 1
Spectroscopic Mode	Single Pixel (Cluster) Mode	8
	Charge Summing Mode	4 + 4

Earlier generations of the Medipix chip suffer from charge sharing problems, in which the charge generated in a photon interaction is 'shared' between pixels [82, 83]. This results in high-energy incident photons being distinguished as two or more lower-energy photons, producing a distortion in the energy spectrum measured by the individual pixels. In the Medipix3RX chip, this limitation has been addressed by the implementation of an architecture that lets two adjacent pixels 'communicate' prior to assignation of the hit to a single pixel [82]. In this CSM mode, four pixels are clustered to form a single unit. The charge deposited to a single cluster unit is reconstructed at the summing nodes physically located at the pixel corners [84-86]. The arbitration logic will then identify the node with the highest energy deposition in the neighborhood and increases its counter; while at the same time inhibits the counter from incrementing for the same detected charge. Figure 4.6 illustrates the CSM mode in operation.
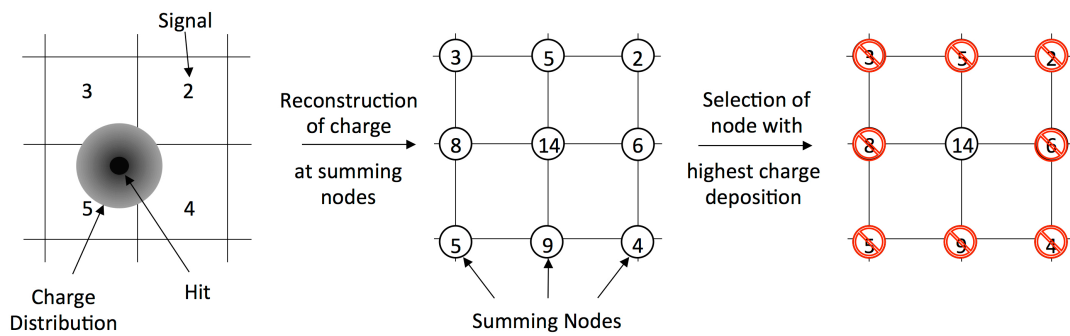
Figure 4.6: A schematic diagram of the Medipix3RX chip in CSM mode. In the first step, the charge deposited to a cluster unit is collected and reconstructed at the summing nodes located at the edge of the individual pixels. The arbitration logic will then discriminate and select the node with the highest charge deposition. The respective counter of the pixel will be increased, while at the same time other pixel counter will be inhibited. Figure adapted from Talla et al. [86].

The setup used in this study is shown in Figure 4.7. It consists of an X-ray source, a rotating sample holder, and the LAMBDA detector assembly (Medipix3 Collaboration and DESY). The LAMBDA detector assembly is equipped with bump-bonded Silicon sensors of 300μm thickness that also has a pitch of 55μm. This particular configuration enables acquisition with high spatial resolution, but does not allow the use of CSM in combination with spectroscopic mode.
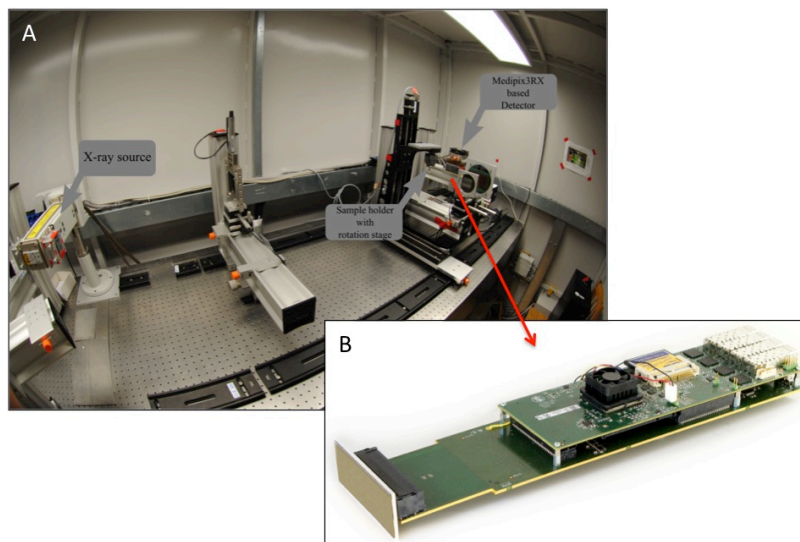
Figure 4.7: Image A shows the setup for the spectral CT measurements. The system consists of an X-ray source, a rotating sample holder, and the Medipix3RX-based detector. Image B illustrates the LAMBDA detector assembly. Credit to DESY and Chair for Biomedical Physics, Technical University Munich for the LAMBDA detector and the Medipix3RX chips.

4.4 Material Decomposition

4.4.1 Theoretical Framework

In diagnostic imaging X-ray energy range of 25 – 150 keV, the attenuation of X-ray photons are primarily due to photoelectric absorption and Compton scattering. Photoelectric absorption can be approximated by the E^{-3} energy dependence and takes place at the lower energy range [1]. At higher X-ray energies, the Compton effect is more dominant and the cross-section can be derived from the Klein-Nishina function. In the presence of materials with distinctive k-edge discontinuity such as iodine, the linear attenuation coefficient μ can be described as [43]:

$$\mu(\vec{x}, E) = a_1(\vec{x})\frac{1}{E^3} + a_2(\vec{x})f_{KN} + a_3(\vec{x})f_I(E) \qquad (4.1)$$

where a_1, a_2 and a_3 denotes the local density of the basis function, f_{KN} the Klein-Nishina function and f_I the mass attenuation of k-edge material. The Klein-Nishina function f_{KN} can be derived from (2.2)

In order to estimate the line integrals $a_i(\vec{x})$ of the individual basis functions, a minimum number of three X-ray intensity measurements are required. In this case, a PCD provides the measurements. For a PCD with N energy bins, the number of photons λ_n detected in an energy bin, given photon fluence of $\Phi(E)$, can be estimated as [43]:

$$\lambda_n(A_1, A_2, A_3) = \int_0^\infty S_n(E)\Phi(E)exp^{(-A_1E^{-3}-A_2f_{KN}-A_3f_I)} D(E)dE \qquad (4.2)$$

where

$$n = 1, \dots, N \quad \text{and} \quad A_i = \int a_i(\vec{x})ds \;\; i = 1,\dots,3$$

The index n refers to the nth energy window, A_i the line integral of the individual material, while $S_n(E)$ is the spectral response of the detector.

As the number of energy bins exceeds the number of the basis function, the system becomes over-determined. The maximum likelihood parameter estimation method is used to estimate the line integrals of the individual components. If the counting procedure is assumed to have a Poisson distribution, and given by

measurement results (m_1, m_2), the likelihood function parameterized by A_i can be written as:

$$P(m_1, \ldots, m_n \mid \lambda_1(A_i), \ldots, \lambda_n(A_i)) = \prod_{n=1}^{N} \frac{\lambda_n(A_i)^{m_n}}{m_n!} e^{-\lambda_n(A_i)} \qquad (4.3)$$

For convenience, it is best to minimize the negative log-likelihood function instead of maximizing the likelihood function P [43]. The negative log-likelihood function can then be expressed as:

$$L(m_1, \ldots, m_n \mid \lambda_1(A_i), \ldots, \lambda_n(A_i)) = \sum_{n=1}^{N}[\lambda_n(A_i) - m_n \ln \lambda_n(A_i)] \qquad (4.4)$$

This maximum likelihood technique yields the sinograms of photoelectric effect, Compton scattering and the attenuation of the k-edge material.

4.4.2 Estimation of Noise in Decomposed Sinograms

For parameters estimated using the Maximum-Likelihood Estimator (MLE), the variance of the unbiased estimator can be computed from the Fisher information matrix whose inverse defines the Cramer-Rao Lower Bound (CRLB)[87]. As the negative log-likelihood L is a function of line integrals A_i, the Fisher information matrix can be written as [88]:

$$F_{\alpha\acute{\alpha}} = E\left[-\frac{\delta^2 L}{\delta A_\alpha \delta A_{\acute{\alpha}}}\right]\bigg|_{A_i = \hat{A}_i}$$

$$\qquad (4.5)$$

$$= \sum_{n=1}^{N} \frac{1}{\lambda_n} \frac{\delta^2 \lambda_n}{\delta A_\alpha \delta A_{\acute{\alpha}}}\bigg|_{A_i = \hat{A}_i}$$

The diagonal elements of the inverse of the Fisher F^{-1} matrix provide the lower bound for the variance of the line integrals [89]. The noise in the material decomposed sinograms can be calculated from the square root of the variance.

4.5 Clinical Application (I) – Metal Artifact Reduction

Artifacts occur frequently in CT. They are generally described as the discrepancy between the CT numbers of the reconstructed image and the true

attenuation coefficients of the object [47]. Artifacts degrade the diagnostic quality of CT images and may result in false evaluation of patients. While the common type of artifact in CT image is the beam-hardening artifact, another cause of artifacts in clinical CT is the presence of high Z-materials in the field-of-view such as hip prostheses, metal implants and dental fillings [47], [90]. These materials have high attenuating properties, resulting in the photon starvation phenomenon, whereby the amount of photons reaching the detector is highly reduced [91]. The 'missing information' on the projection data cause incorrect calculations during the conventional analytical image reconstruction process, thus leading to severe streaking and dark and bright shading around the metal implant, as shown in Figure 4.8.
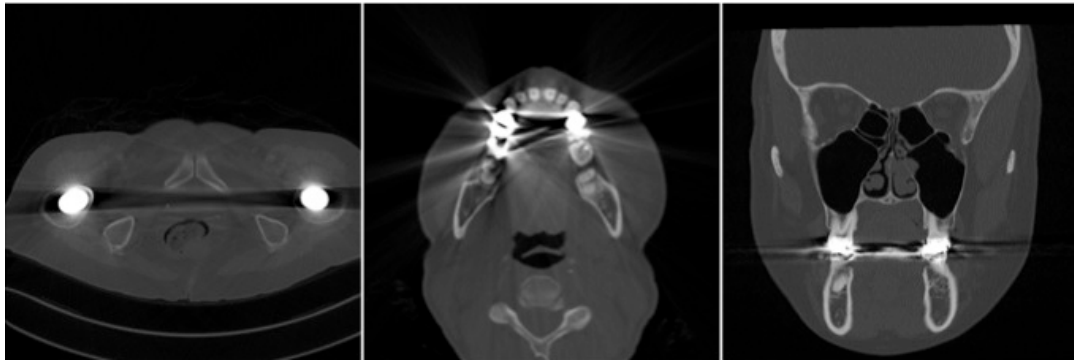
Figure 4.8: The presence of high Z-materials causes severe photon starvation and results to a significantly reduced amount of photons reaching the detector. The image left is metal artifacts due to the hip prostheses, the middle and the right due to dental implants. Examples taken from the Department of Diagnostics and Interventional Radiology, Klinikum rechts der Isar.

Various methods have been developed for metal artifact reduction (MAR) [92-98]. One popular technique is in-painting. In this method, regions associated with metal are 'replaced' by interpolating neighboring values in the sinogram. [97-99]. In detail, the technique involves masking or segmenting the CT images to obtain the metal only image, forward projecting it, remove the metal-only data from the original sonogram and interpolate the missing sinogram from its neighbors before re-reconstructing the modified sinogram. While this method removes most of the streaking artifacts in the image, it has limited effectiveness, as it is prone to reintroduce other artifacts due to interpolation errors, causing a loss of details especially around metal implants. Another advanced method is to recover the high frequencies of an uncorrected image, which contains edge information and noise, and recombine it with the MAR-corrected image [100]. This technique has been shown to

preserve details around the metal implant; however, it is very dependent on the optimal segmentation of the metal from other high frequency components in the image such as bone.

A unique approach from Stayman et al. [91] uses a model-based penalized maximum-likelihood estimation to reduce the effects of metal artifacts. In the method, known as Known Components Reconstruction (KCR), information on the shape and composition of the metal in the scanned object is derived from a computer-assisted design (CAD) model and is incorporated into the iterative reconstruction process as prior. CT images reconstructed using this technique have shown significant reduction of streaking artifacts and dark shading as a result of the presence of metal, when mono-energetic X-rays are used.

This work adopts the same concept of incorporating prior knowledge into the reconstruction algorithm to reduce metal artifacts in CT images. However, instead of using a CAD model, the additional information obtained from Spectral CT is used as a priori for the reconstruction scheme. The proposed algorithm is based on a two-step approach; in the first step the algorithm performs material decomposition on the spectral data to determine the shape and the spatial location of the metal implant, and in the second step the information is incorporated as a prior into a penalized maximum log-likelihood reconstruction algorithm.

4.5.1 Overview of the Algorithm

An overview of the algorithm is illustrated in Figure 4.9 as well as in the pseudo code in Algorithm 1. It consists of two steps: material decomposition of the Spectral CT data (A) and the penalized maximum likelihood iterative reconstruction (B). The algorithm is called Spectral-driven Iterative Reconstruction (SPIR).
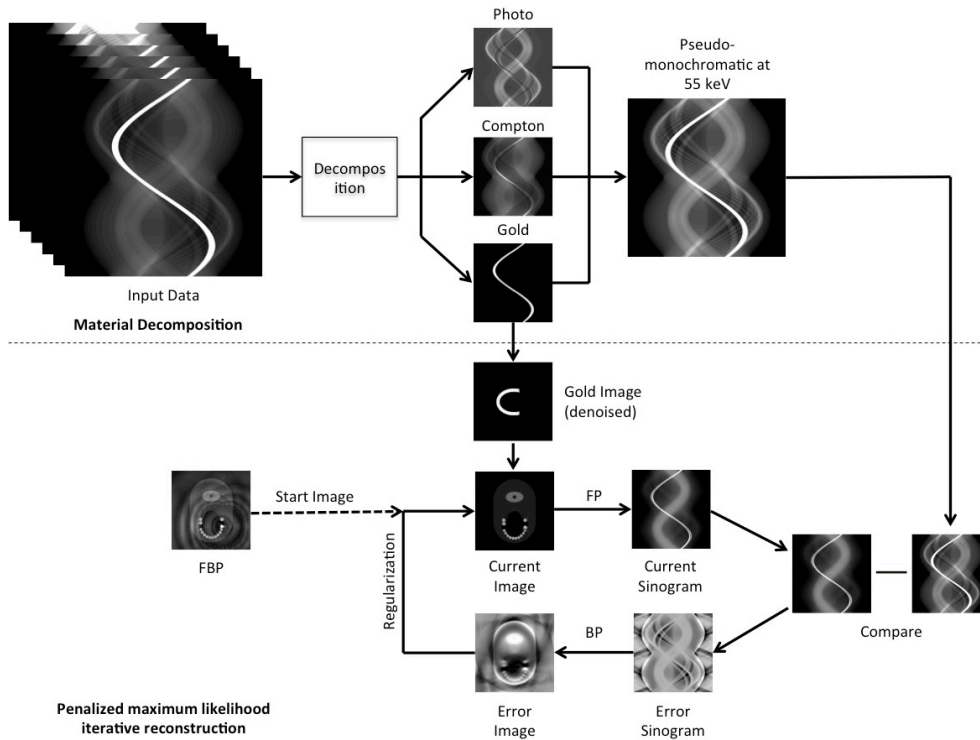
Figure 4.9: An overview of the SPIR technique. In the first of two steps, the projection data is decomposed into several basis functions from which the pseudo-monochromatic projection is calculated and the metal image is reconstructed. Using these as input and prior respectively, the image is iteratively reconstructed in the second step, while at the same time knowledge on the location and density of the metal implant is enforced and corrected.

4.5.2 Penalized Maximum Likelihood Iterative Reconstruction

For reconstruction, a penalized maximum likelihood approach was used. This Poisson-statistics-based algorithm uses the raw measurements rather than the logarithms of the data, and thus is believed to solve nonlinearity of the logarithm and handle low radiation scans.

The goal of the algorithm is to maximize a cost function Ψ, which consists of a likelihood term L and regularization term R. L indicates how the reconstructed result matches the input sinogram;

$$\hat{\mu} = arg\,max\,\Psi(\mu), \qquad \Psi(\mu) = L(\mu) - \beta R(\mu) \qquad (4.6)$$

where μ indicates the image matrix in attenuation values. It describes the probability of how the reconstructed result matches the measurement [15]. R is a regularization term given in [101]. The regularization can be controlled by β.

$$R(\mu) = \sum_{k} w_{jk}\psi(x_j - x_k)$$

(4.7)

Adding a penalty term to regularize the problem leads to a faster convergence and an enforcement of desired and beforehand known image properties like smoothness and edge preservation. Lange's [102] function is used as penalty function $\psi(t)$ in the regularization term. Lange's penalty has the feature to eliminate noise as well as preserve edges in the images.

$$\psi(t) = \delta^2[|t/d| - log\,(1 + |t/d|)]$$

(4.8)

δ is a constant as the edge threshold in denoising.

In order to maximize this optimization problem, the separable paraboloidal surrogate (SPS) technique [15] is used. Each update step is given by:

$$\mu^{n+1} = \left[\mu^n + \frac{BP\big[b\,\exp(-FP[\mu^*]) - y^*\big] - \beta \sum_k w_{jk}\dot{\psi}(x_j - x_k)\big]}{BP\big[y^*FP[1]\big] + \beta \sum_k w_{jk}\ddot{\psi}(x_j - x_k)}\right]$$

(4.9)

where y^* is the monochromatic projection data. FP [] and BP [] denote the forward- and backward projection respectively; $w_{jk}\psi()$ the regularization term; x_j are pixels in image μ, while x_k are neighboring pixels of x_j. w_{jk} indicates the distance-weight between x_j and x_k. b is the X-ray intensity at the source.

Selecting the constants β and δ for the regularization was subjectively done. The user defined the trade-off point between the data fidelity term and the roughness term. This was done by a specification of a desired target noise level of the reconstructed image.

Prior to each update step as in (4.9), the location and density of the gold determined in the previous section are pre-computed into exact pixel values in image matrix μ, where metal material is observed. The modified image matrix with prior information is noted as μ^*.

In each update step, a subset of three angles is taken in the forward and back projection to compute an update of μ. These angles are randomly chosen from the total number of projections to accelerate the optimization process. In this work, a full iteration is considered when all projections are chosen (360° rotation). Previous

51

experiments indicate that a convergence can be seen after 10 to 15 full iterations, thus for this work 15 iterations were chosen as the stopping criteria.

In summary a simplified version of the algorithm can be found as pseudo code in Algorithm 1.

Algorithm 1 pseudo code

$A \leftarrow$ initialize parameters A_1, A_2, A_3

for i = 1 to max projection data **do**

     for j = 1 to number of detector elements **do**

         $A \leftarrow \min \sum_{n=1}^{N} [\lambda_n(A) - m_n \ln \lambda_n(A)]$

     end for

end for

$\mu_{metal} \leftarrow \text{FBP}[A_3]$

$\mu \leftarrow$ initial reconstruction

$d = \text{BP}[y^* \cdot \text{FP}[1]]$

for k = 0 to max iteration do

   for m = 1 to number of subset do

         $\mu^* \leftarrow \mu_{metal}$

         $l \leftarrow FP[\mu^*]$

         $h \leftarrow b \cdot exp\,(-l) - y^*$

         $L \leftarrow \text{BP}\,[h]$

         $\mu \leftarrow \left[\mu + (L - \beta \dot{R})/(d + \beta \ddot{R})\right]^+$

     end for

end for

4.5.3 Description of Experiment

A phantom based on the information provided by the Phantom-Group (IMP, University Erlangen-Nürnberg, Erlangen, Germany) was simulated. It consisted of 16 molars, with one of which has a dental implant out of pure gold (density 19.3 g/cm³). Two of the molars were removed to simulate a gap (see Figure 4.10). In this work, different shapes and sizes of dental implants were used. This was done to test the influence of prior knowledge on the overall performance of the SPIR algorithm. For the simulation, a mathematical phantom made out of known geometry was used, instead of a voxel phantom, in order to accelerate the simulation process.
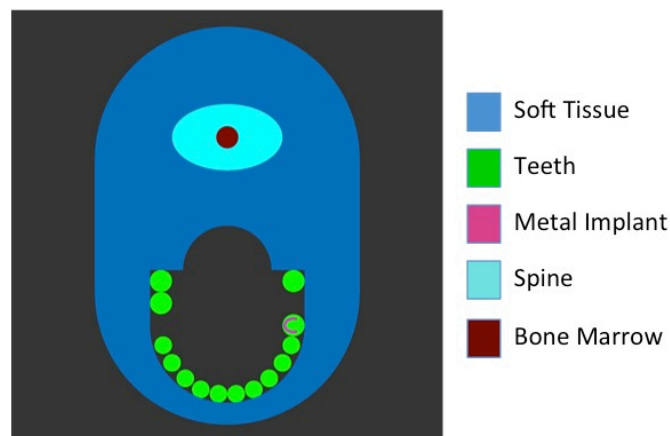
Figure 4.10: One of the virtual phantoms used in this work. It contains several anatomic components of a jaw such as soft tissue, spine, bone marrow and teeth. A metal implant is embedded on one of the teeth. In this work, three different shapes of metal implant: circle, horseshoe and triangle were simulated.

The X-ray source was generated at tube voltage of 125 kV with Tungsten target and aluminum filter of thickness 2.7mm, yielding mean spectrum energy of 55.457 keV. A total of 3.10×10^{10} photons were released at the source. A clinical dental CT system with a source to detector distance of 80 cm, source to isocenter distance of 60 cm and a detector with 2200x2200 pixels of 0.01 x 0.01 cm^2 size was modeled. The detector was operated in photon-counting mode with each photon discriminated according to its kinetic energy into 62 bins, with each bin having a bin width of 2 keV. The implementation of 2 keV energy bins allowed the determination of the optimal number and size of the energy windows even after the simulation, thus avoiding the need to redo the simulations for other energy window configurations. These individual energy bins were summed together after the complete simulation to obtain spectral CT projection data with six energy windows. Although the number of energy windows can be arbitrarily chosen, the choice of six energy windows was made as this yielded better material decomposition results, without negatively effect the photon statistics in an individual window [10]. In order to make the simulations as realistic as possible, all physical effects such as Rayleigh scattering, atomic relaxations and photoelectron angular sampling were taken into consideration. The detector was assumed to be ideal, thus effects such as charge sharing and pulse splitting can be neglected. However, the effects of scattered photons were taken into account in the simulation.

4.5.4 Results

In the first step of the SPIR algorithm, the projection data were first decomposed into three basis functions that describe the total attenuation in the scanned object. Figure 4.11 illustrates the original model and the results of decomposition into three basis component images: (A) photoelectric effect, (B) Compton scattering and (C) gold attenuation. One can see that the spatial location of the gold implant is accurately detected and distinguished from other anatomic structures of the phantom such as teeth and spine. On a closer visual inspection, the shape of the metal implant is exact and resembles the original model, as illustrated by the top row of Figure 4.12. Subtracting images of the gold component image from the original model show only a slight difference of 1 pixel between the images, which can be attributed to discretization error in the simulation, indicating the high accuracy of the material decomposition technique. Further, the average difference in density between the decomposed metal and the original model is about 1.5% or $0.285 g/cm^3$.
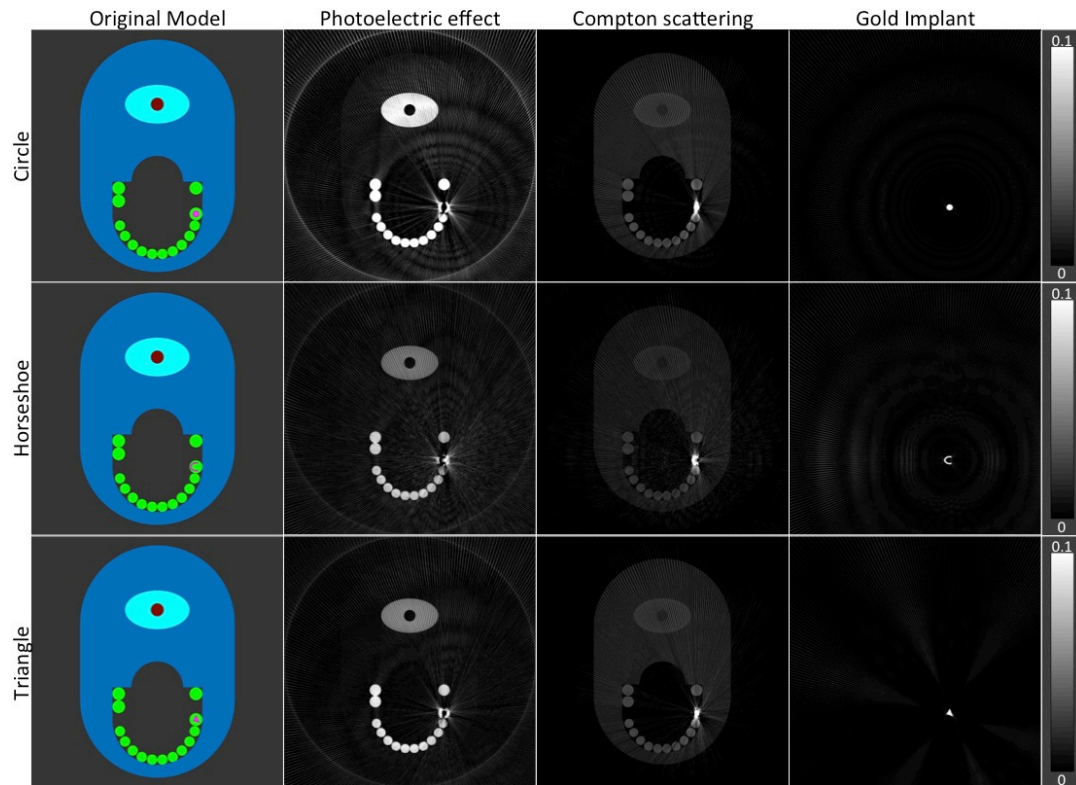
Figure 4.11: The original model of the phantom and the images of the decomposed basis functions reconstructed with filtered back-projection (FBP). The second column shows photoelectric attenuation, third column the Compton scattering, and the fourth column the gold attenuation. Row-wise are the different shapes of the metal implant: first row circle, second row horseshoe, and bottom row triangle. It can be seen that, the location of the gold implant is accurately detected, while the gold implant can be distinguished from other parts of the phantom, especially the teeth. The reconstructed images are normalized to 1, and have WW of 0.2 and WL of 0.1.
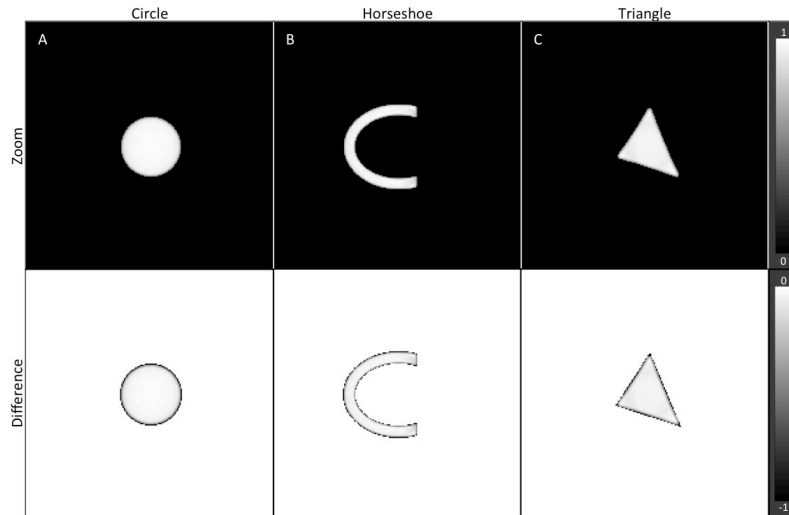
Figure 4.12: The zoom-in of the metal implant obtained shown in the top-row indicates the accuracy of the material decomposition technique in detecting the metal implant. When compared to the original model, only a slight difference as in 1 pixel is observed, which can be attributed to discretization error. The average difference in density is about 0.285 g/cm^3. The top-row images are normalized to 1, with WW of 1.0 and WL of 0.5. The bottom-row images have WW 1.0 and WL of -0.5.

The second step of the algorithm involves the statistical reconstruction of the pseudo-monochromatic data, with the information of the gold component used as a prior. Figure 4.13 presents the full-view and the zoom-in of the images reconstructed with three different reconstruction algorithms: filtered back projection (FBP), penalized maximum likelihood iterative reconstruction on the plain absorption data without prior information (IR), and SPIR. In the first row, the reconstruction using FBP produces images with massive streaks and black and white shadings, especially around the metal implant. The presence of these artifacts severely degrades the diagnostic quality of the image, while at the same time information near the implant is lost. Using the more advance IR algorithm these artifacts are significantly reduced, as shown by images in the second row; however the dark and bright shadings around the implant are still visible. In the third row one can observe that the incorporation of prior information obtained from the material decomposition technique into the reconstruction algorithm delivers notably improved images: bright streaks are reduced significantly without compromising the anatomical information, while the shadings around the dental implant are considerably eliminated, as displayed in the zoom-in. The SPIR algorithm is not only able to reduce the artifacts, but also is able to preserve the edges and valuable anatomical details near the implant.
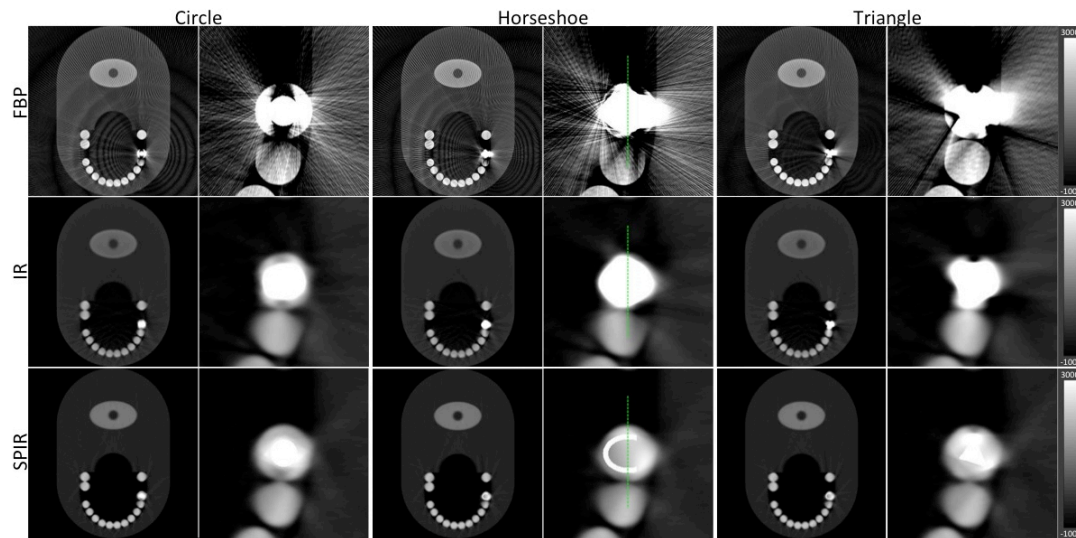
Figure 4.13: The reconstructions of the phantom using different algorithms: first row using FBP, second row penalized maximum likelihood iterative reconstruction without prior (IR), and the third row Spectral-driven Iterative Reconstruction (SPIR). Column wise are the different shapes of metal implant at full-view and zoomed-view. The first column-pair has the shape circle, second column-pair horseshoe, and third column-pair triangle. All images have WW of 1000 HU and WL of 4000 HU.

The results are analyzed quantitatively by selecting a line-of-interest and collected pixel values (attenuation values) along the line, as indicated by the green line in the middle column images of Figure 4.13, and compare it to the true theoretical values used in the Monte Carlo simulation. Figure 4.14 illustrates the line profiles of the three reconstruction algorithms. On the y-axis, the theoretical attenuation values of several anatomical components such as teeth and the gold implant are shown as dashed lines. From the graph one can see that the artifacts in the FBP images cause a massive fluctuation of values. The IR algorithm produces a smooth profile but does not return attenuation values similar to the true theoretical one. SPIR algorithm is the only one to produce robustly and reproducibly the true theoretical value.
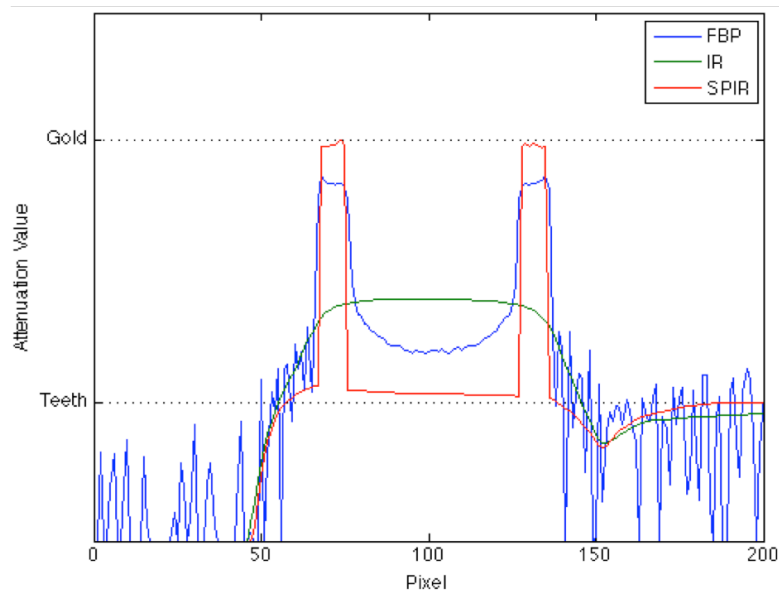
Figure 4.14: The vertical line profiles as marked in **Figure 4.13** for different reconstruction algorithms. The line profile from SPIR algorithm reflects the true attenuation values best, in comparison to FBP and IR.

Computationally, the FBP algorithm needs 5 seconds to reconstruct an image. For the same image the IR and the proposed SPIR algorithm took about 20 minutes for 15 iterations.

Further, the influence of accurate localization and detection of the metal implant on the performance of the SPIR algorithm is also investigated. Figure 4.15 shows the result of reconstruction presuming that the prior information on the metal implant is inaccurate; i.e. the metal implant is smaller or larger than the original size by 1 to 2 pixels. From the images, one can notice that SPIR suffers badly under such conditions. Artificially induced artifacts in the form of bright or dark shadings appear near the metal implant, resulting in the loss of details near the implant.
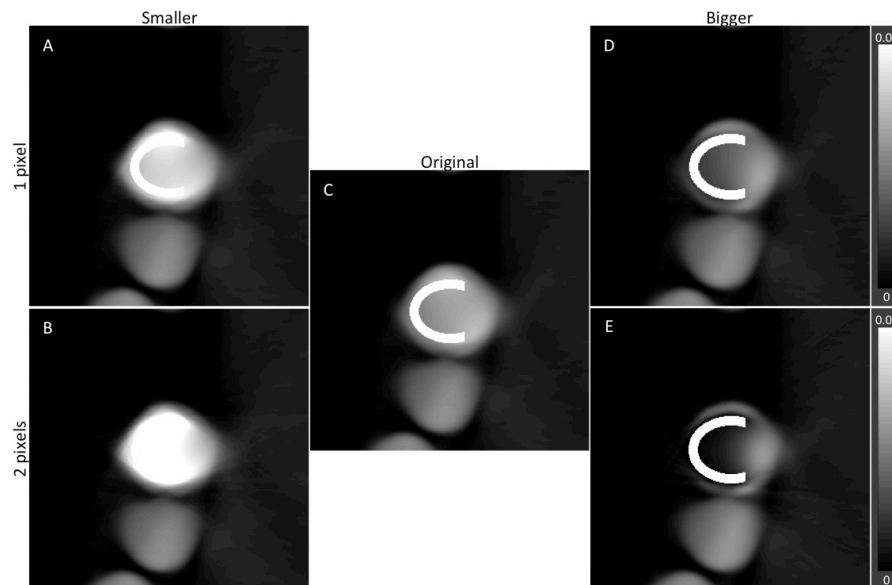
Figure 4.15: The influence of the prior information on the outcome of the model-based iterative reconstruction. The results with a smaller (A and B) or larger (D and E) metal implant show that inaccurate prior results in a less than optimal image. The reconstruction result with the original model is shown in C for comparison. All images have WW of 4000 HU and WL of 1000 HU.

4.6 Clinical Application (II) – Low Concentration of Iodine

In unenhanced CTs, the differentiation of abnormalities is difficult, as the solid organs have similar density range of 40-60 HU. The usage of CM enhances the density of the different tissues; hence an improvement in contrast can be observed [103-105]. This is clinically beneficial, especially in the detection of tumors and lesions. The magnitude of enhancement is proportional to the amount of iodine concentration deposited in the target organ; the higher the amount of iodine, the higher the enhancement of the organ [104]. However, the usage of iodinated CM poses health issues, ranging from mild side effects such as headache, nausea and itching to serious complications such as contrast-induced nephropathy (CIN) [106-108]. The risks associated with the usage of CM warrant more investigation into methods to reduce the amount of CM, without compromising the diagnostic quality. Additionally, the reduction of CM would also bring down the related healthcare cost. This work focuses on the reduction of iodinated CM in contrast-enhanced DECT. In the first step, the material decomposition technique was applied on the projection data to identify and discriminate iodine of lower concentration from other materials in the phantom. Using the spatial information of the low-concentrated iodinated CM, a CT

image that enhances the appearance of the iodine in the image was iteratively reconstructed.

4.6.1 Detection of Iodine per Material Decomposition

The material decomposition technique explained in section 4.4.1 was used to detect and distinguish iodine from other components of the phantom. The basis materials chosen were the photoelectric effect, Compton scattering and iodine. Additionally, the variance of the likelihood estimation for each basis material line integrals, $\sigma_{A_i}^2$, was estimated using the Fisher matrix as discussed in subsection 4.4.2. The mean value of the line integrals and their variances were used as input in a statistical iterative reconstruction scheme.

4.6.2 Statistical Iterative Reconstruction

The noise in the material-specific image is affected by the total attenuation of all materials in the object. The presence of other strong attenuating materials reduces the number of photons reaching the detector, results to the increase in noise in the energy bins, which subsequently propagates into the decomposed sinograms. The estimated variance can be used in a statistical image reconstruction scheme to reduce noise and enhance image contrast. For the statistical image reconstruction of a material-specific image, the same penalized maximum likelihood iterative reconstruction as discussed in subsection 4.5.2 was used. However, instead of using Poisson distribution, a Gaussian noise model was assumed. The Gaussian noise model was chosen because it has been shown that the line integrals of the decomposed images approximately follow a Gaussian distribution [89]. The marginal log-likelihood function and its derivatives is given by:

$$g_{A_i}(\mu) = -\frac{1}{2}ln\left(2\pi\sigma_{A_i}^2\right) - \frac{(A_i - \mu)^2}{2\sigma_{A_i}^2}$$

$$\dot{g}_{A_i}(\mu) = \frac{(A_i - \mu)^2}{\sigma_{A_i}^2} \qquad\qquad (4.10)$$

$$\ddot{g}(\mu) = -\frac{1}{\sigma_{A_i}^2}$$

The term A_i is the mean value of the material decomposed sinogram and $\sigma_{A_i}^2$ is the variance, which can be obtained from the noise estimation steps described in section 4.4.2.

In this work, the statistical image reconstruction is called maximum-likelihood iterative reconstruction (MLIR). The algorithm is based on the separable paraboloidal surrogates and penalty weighting as discussed in section 4.5.2. However, instead of using (4.9), a modified update function is used is given by:

$$x_A^{n+1} = \left[x_A^n + \frac{BP\left[\dot{g}_{A_i}\left(\mu_{A_i}^{(n)} \right) - \beta \sum_k w_{jk} \dot{\psi}(x_j - x_k) \right]}{-BP\left[\ddot{g}_{A_i}{}^* FP[1] \right] + \beta \sum_k w_{jk} \ddot{\psi}(x_j - x_k)} \right] \qquad (4.11)$$

where $\mu_{A_i}^{(n)}$ describes the forward projection of material image $x_A^{(n)}$ at the nth iteration and **1** the unity image, which can be pre-calculated. FP [] and BP [] denote the forward- and backward projection respectively; $w_{jk}\psi()$ the regularization term; x_j are pixels in image x, while x_k are neighboring pixels of x_j. w_{jk} indicates the distance-weight between x_j and x_k; and β is the penalty strength. The regularization term and penalty is as discussed in the previous section.

4.6.3 Description of Experiment

A modified CTP515 module of the CatPhan 600 (The Phantom Laboratory, Incorporated, Greenwich, New York, USA) was simulated as the object to be imaged. The original module is designed to measure low contrast sensitivity and consists of a series of cylindrical rods of various diameters and contrast-levels. Instead of three contrast-levels, the phantom was modified to have six contrast-levels with each level having a different concentration of Imeron 400 MCT, a tri-iodinated non-ionic monomeric contrast medium commonly used in diagnostic radiology. The supra-slice contrast targets have concentrations of 25%, 12.5% and 6.25% of the pure Imeron 400 MCT solution, while each of the sub-slices have 2.5%, 1.25% and 0.625%. This corresponds to 100 mg/ml, 50 mg/ml, 25 mg/ml of iodine in the supra-slice targets, and 10 mg/ml, 5mg/ml and 2.5mg/ml for the sub-slices. All other areas of the phantom are constructed out of water. A sketch of the phantom can be seen in Figure 4.16.
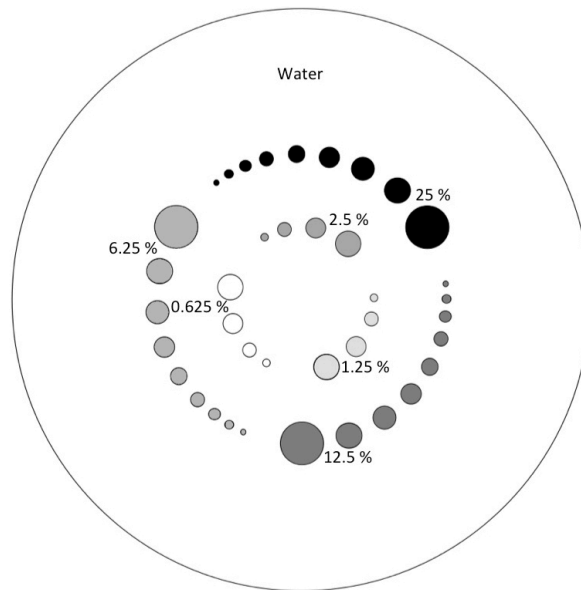
Figure 4.16: The phantom used in this study. The targets (regions-of-interest) consist of different iodine concentrations.

In this study, the projection data was generated from the Monte-Carlo simulation technique. The same simulation protocol was used as in the previous study in the previous section. The X-ray source was generated at tube voltage of 125 kV with Tungsten target and aluminum filter of thickness 2.7mm. A total of 3.10×10^{10} photons were released at the source. The detector was operated in photon-counting mode with each photon discriminated according to its kinetic energy into 62 individual bins of 2 keV width each. At completion of the simulation, these individual energy bins were summed together to obtain spectral CT projection data with six energy windows. The energy windows are chosen such that all photons at the k-edge energy of iodine are captured into a narrow energy window. All physical effects such as Rayleigh scattering, atomic relaxations and photoelectron angular sampling were taken into consideration. The detector was assumed to be ideal, thus effects such as charge sharing and pulse splitting can be neglected.

4.6.4 Results
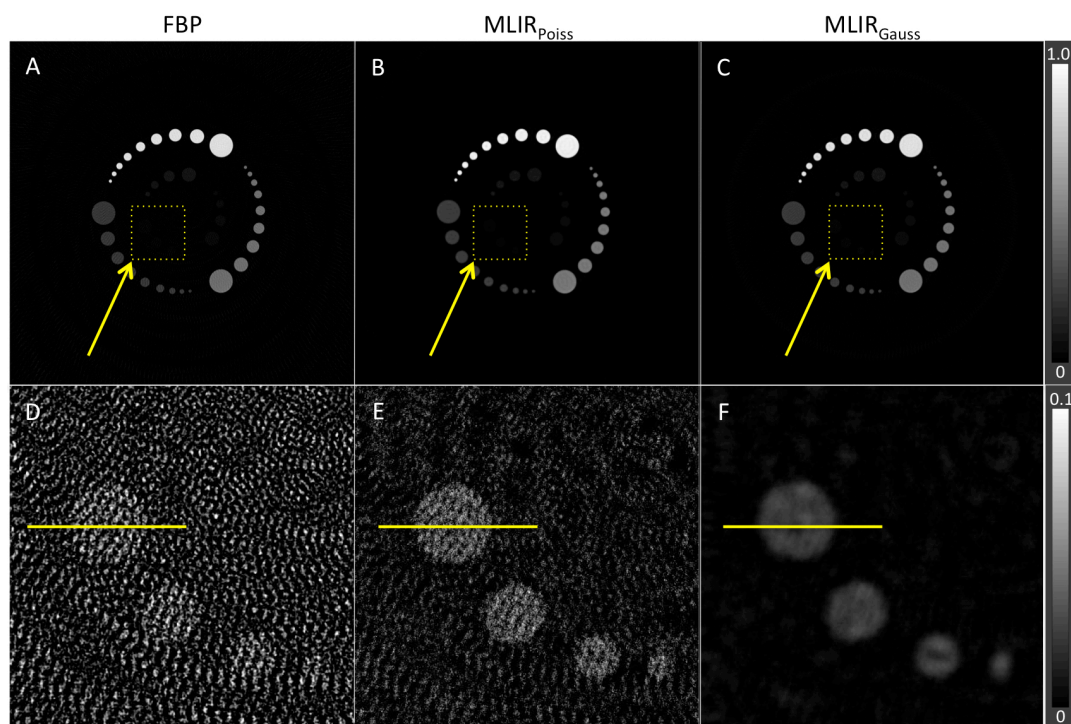
Figure 4.17: The decomposed iodine-only image and the zoom-in image reconstructed using FBP (A and D), MLIR$_{\text{Poiss}}$ (B and E), and MLIR$_{\text{Gauss}}$ (C and F). The strong noise in the FBP image as seen in D overwhelms the signal from the iodine, affecting the appearance of iodine in the image. A reduction of noise can be achieved using advance algorithm such as MLIR$_{\text{Poiss}}$ as seen in E, but with the proposed MLIR$_{\text{Gauss}}$ algorithm, most of the noise is suppressed; thus the SNR ratio of the iodine is significantly increased. All images are normalized to 1, with the images A, B, and C having WL of 0.5 and WW of 1.0, while images C, D, and E are windowed with WL of 0.05 and WW of 0.1.

The spectral data was first decomposed to three basis components: photoelectric effect, Compton effect, and the attenuation due to iodine. Then, the decomposed iodine-only projection data was reconstructed using three different methods: by using conventional FBP, the maximum-likelihood iterative reconstruction using Poisson distribution (MLIR$_{\text{Poiss}}$), and the proposed maximum likelihood iterative reconstruction based on Gaussian distribution (MLIR$_{\text{Gauss}}$) algorithm. Figure 4.17 shows the reconstruction of the material decomposed data using all three algorithms. In general, one can see that the material decomposition technique was able to isolate the iodine solutions from other parts of the phantom. However, on closer inspection the MLIR$_{\text{Gauss}}$ reconstruction algorithm delivered a notably improved contrast of the iodine: the lower concentrated iodine solutions are better seen in the MLIR$_{\text{Gauss}}$ reconstructed image than in the FBP and MLIR$_{\text{Poiss}}$

images. Additionally, a significant reduction of noise can be seen in the $MLIR_{Gauss}$ reconstructed image, as seen in the plot profile in Figure 4.18. Quantitatively, the measured signal-noise-ratio (SNR) for FBP, $MLIR_{Poiss}$, and $MLIR_{Gauss}$ reconstructed iodine-only images are 1.05, 1.45 and 8.25 respectively.
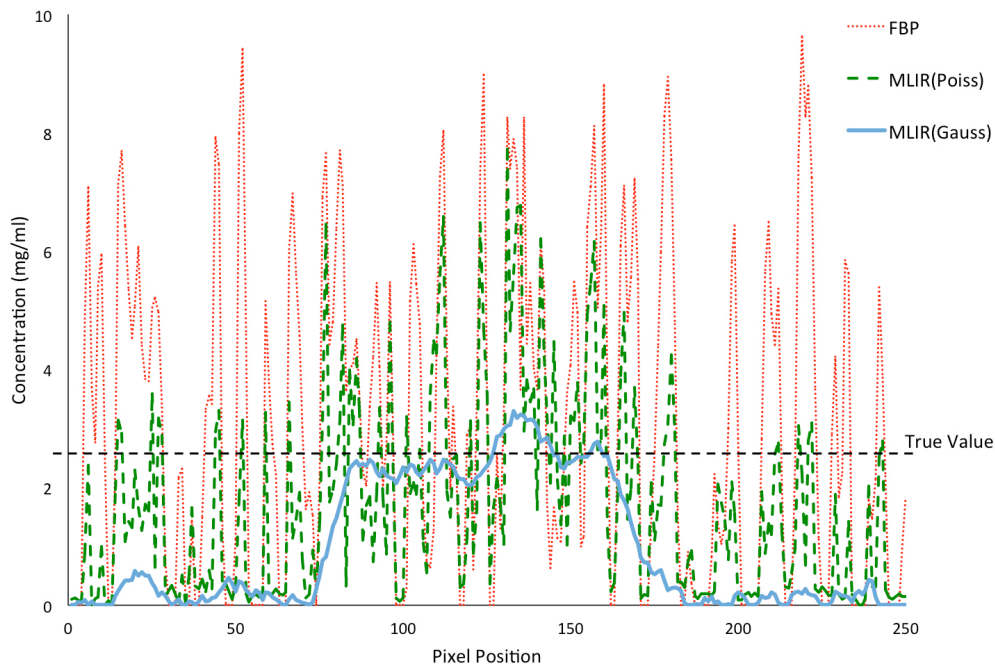
Figure 4.18: The line profile across the iodine target with the lowest concentration as specified in **Figure 4.17**. The plot of the line of interest shows that the pixel value in FBP has a huge deviation from the true value that can be attribute to the presence of noise. Using advance algorithm such as $MLIR_{Poiss}$ reduces the amount of noise, yet the pixel value deviates from the true value, On the other hand, the $MLIR_{Gauss}$ has a more constant value along the line and better reflects the true value (2.5 mg/ml).

Further, the concentration of iodine in the images were measured and compared to the true concentration value. The contrast targets of the same concentrations but different sizes were measured and the obtained values were averaged. Table 4.2 shows the result of the iodine concentration measurements. The measurement results show that the iodine concentrations in the $MLIR_{Gauss}$ reconstructed image are closer to the true value in comparison to the ones measured in the FBP and $MLIR_{Poiss}$ image. This demonstrates the algorithm's ability to detect low concentration of iodine with high accuracy.

Table 4.2: The concentration measurements from images reconstructed using FBP and MLIR.

Target	True Concentration (mg/ml)	Measured Concentration (mg/ml)		
		FBP	$MLIR_{Poiss}$	$MLIR_{Gauss}$
Target 1	100.00	99.23	98.24	97.61
Target 2	50.00	50.39	49.37	48.62
Target 3	25.00	26.61	25.64	24.90
Target 4	10.00	11.11	10.64	9.80
Target 5	5.00	6.20	5.63	4.85
Target 6	2.50	3.79	3.28	2.46

Both $MLIR_{Poiss}$ and $MLIR_{Gauss}$ images were reconstructed with 20 iterations for comparison reasons. Additionally, the same penalty function and strength were used for both algorithms. However, it has to be noted that no visual changes can be seen in the $MLIR_{Gauss}$ image after 10 iterations, while the iodine concentrations remained constant after 15 iterations. Additionally, the same regularization function and penalty strength were used for both algorithms.

4.7 Clinical Application (III) – Multi-material K-edge Imaging

In addition to iodine, other examples of radiological CM are barium sulfate [109] and gadolinium [110]. Barium sulfate is usually used in CT examinations, while gadolinium is predominantly used to provide enhancement in MR imaging. Recently, new CM based on bismuth, gold, and ytterbium are developed for usage in CT [80, 111]. These CM are disease-specific and have the advantage that they can remain in the blood circulation for a long period of time. The variety of CM serving different diagnostic purposes raises the question on the possibility of the simultaneous usage of the different CM in a single examination. Such examination protocol is desirable, as more diagnostic information can be obtained in a single scan, and thus eliminates the need for multiple scans that may increase radiation dose exposure to patients.

The Medipix3RX detector can be operated with up to eight different threshold levels, making it possible to perform multi-material K-edge imaging. The thresholds can be set below and above the K-edge energy of the material of interest, and using simple processing steps such as subtraction, the material can be easily distinguished from the other materials in the scanned object. Figure 4.19 illustrates an example of

placing energy thresholds below and above the K-edge energy of iodine. Additionally, material decomposition method described in Section 4.4.1 can also be applied to the projection data to distinguish multiple materials in the scanned object.
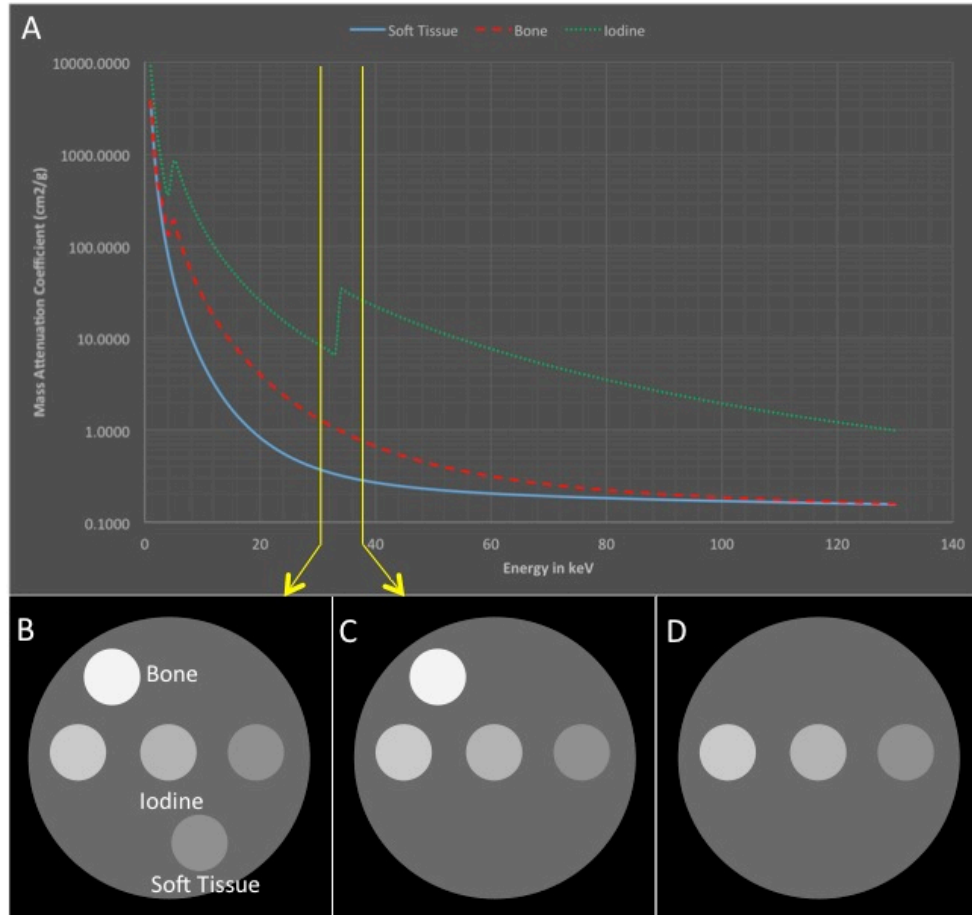
Figure 4.19: An example of the placement of thresholds in K-edge imaging. In this example, image of energy lower (B) and higher (C) than the K-edge of iodine are reconstructed and subtracted from each other. This results in the iodine only image, as shown in D.

In this study, the feasibility of multi-material K-edge imaging was investigated. Two methods of material detection were used: first, by subtracting images below and above the K-edge energy of the material, and second, by applying the material decomposition method.

4.7.1 Description of Experiment

The Medipix3RX is operated in Spectroscopic mode with SPM mode enabled. A total of eight energy thresholds were set up, but two pairs were set at the same threshold in the higher-energy range in order to increase the photon statistics in this energy window. The energy thresholds were 20, 24, 27, 31, 35, 40, 35 and 40 keV.

The source-detector distance (SDD) was set to 164 cm, while the isocenter-detector distance (IDD) was 19.3 cm. At the X-ray source, the tube voltage was set to 60kVp, while the tube was operated at 30 mA.

The phantom used in this study consisted of bone and two tubes, one filled with silver, Ag (K-edge of 25.5 keV) and the other with iodine, I (32.2 keV). The bone and tubes where embedded in a soft tissue (muscle and fatty tissue).

4.7.2 Results

Figure 4.20 shows the reconstructed images of the different energy windows as well as the results of the subtraction between these images to detect the K-edge materials. The subtraction of image B from image A reveals the location of silver in the image, while the result of subtracting image C from image B displays the material iodine. The explicit detection of the materials shows not only the effectiveness of the technique in detecting K-edge materials in general, but also in particular the accurate positioning of the thresholds.
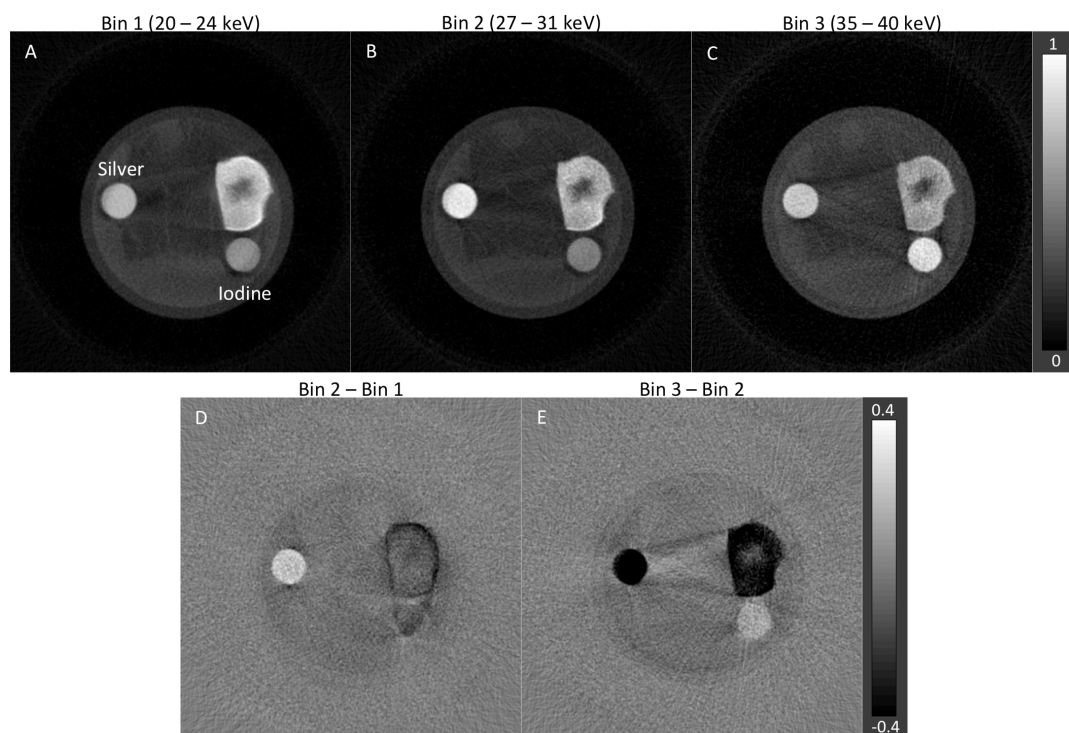
Figure 4.20: The reconstructed images from three energy bins (A-C) and the result of subtraction between the images (D-E). The images on the top row are normalized to 1, with WL of 0.5 and WW of 1.0, while the images on the bottom row illustrated with WL of 0 and WW 0.8.

In the second step of this study, the material decomposition technique was applied to the projection data. Three materials were selected as the basis function: silver, iodine, and bone. Results from the material decomposition technique delivered inexact differentiation of materials, as shown in Figure 4.21. While iodine was accurately distinguished from other materials, silver and bone appeared in both the silver-only and bone-only images. One reason for the inaccuracy of the material decomposition technique is the lack of information provided into the decomposition algorithm. Vital information such as the spectral response of the detector and the X-ray source were missing; and thus the detection process was not accurately modeled. Additionally, due to limitation in the detector configuration, the CSM mode could not be enabled; thus charge-sharing effect was not taken into consideration. It is believed that the decomposition results would be better if this vital information is included in the detection model or if the CSM could be used.
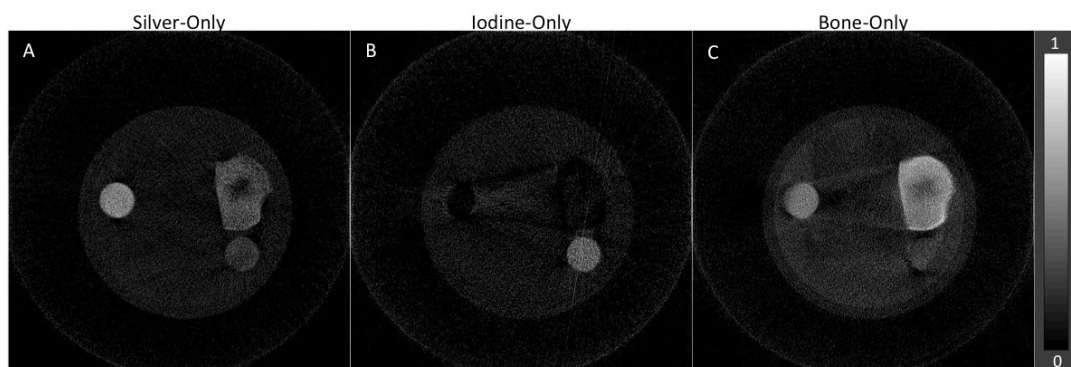
Figure 4.21: The material-decomposed images. Iodine was perfectly distinguished from other materials in the image. In contrast, silver and bone appeared in both the silver-only and in the bone-only images. Imperfect modeling of the detection process is believed to be the cause of the inaccuracy. One positive point is that the contrast of silver is the highest in the silver-only image, in comparison to the one in bone-only image. All images are normalized to 1, with WL of 0.5 and WW of 1.0

4.8 Discussions

4.8.1 Data Acquisition

Simulation

Due to the lack of availability of clinical photon-counting detectors, there is a need for a fast yet reliable simulation package that can assist the development of various algorithms and applications that take advantage of the Spectral CT's potential. In this work, two types of simulators were introduced: the Analytical Simulator (AS)

and Monte Carlo Simulator (MCS). AS has the advantage that it is fast and generates projection data that are comparable to MCS; however it is still not a proven reliable simulation tool. On the other hand, MCS has the capability to generate projection data from a PCD and to simulate results that closely resemble measurements from an actual CT system. Compared to currently available PCDs, MCS is able to simulate very small energy windows. This allows the adjustment of the window size to suit different K-edges or applications even after the simulation was done; hence avoids the need to re-run a time consuming MC simulation and is particularly advantageous when designing experiments and evaluating PCDs.

Further, MCS has the capability to simulate the effect of scatter. This is important as the presence of scatter does not only degrade the image quality, but is also found to have an impact on the material decomposition technique [112]. This has several consequences: first the presence of scatter may restrict the effectiveness of the image decomposition technique, especially in finding small concentrations of contrast agents in the image. Secondly, the presence of scatter may cause false quantification of contrast agents and hence reduce the diagnostic quality. However, the presence of scatter may not necessarily be disadvantageous. As one can observe, in the difference images in Figure 4.4 that scatter radiation holds information about the imaged objects. Similar observations have been made in dark field [113] as well as small-angle X-ray scattering (SAXS) imaging [114].

A drawback of the studies done using the MCS is that an ideal detector was simulated, which has maximum detective quantum efficiency. The spectral response of a detector has effects on the reconstructed images and the material decomposition technique, therefore constructing a real detector would be subject of interest in future studies. Another limitation is the missing comparison to real PCD systems. Currently PCDs are only very limited available and thus a direct comparison was not feasible. However, the results obtained in the studies are comparable to already published results of other investigators working with PCDs [43]. Lastly, if diagnostic multi-slice CT systems are to be simulated, it will be necessary to include several additional components such as a bowtie filter or a 3D anti-scatter grid.

Medipix3RX

The first generation of the Medipix chip, the Medipix1, demonstrated the working principle of photon-counting detectors, while the second generation Medipix2 showed the ability to discriminate photons based on their incident energy. However, the energy spectrum detection of the Medipix2 is limited by the charge sharing between pixels in the chip [82]. The latest generation Medipix3RX was designed specifically to address this charge-sharing problem. The chip's architecture comprises of additional arbitration logic and synchronization logic that enables the accurate detection of photons; while at the same time removes charge-sharing tail from the energy measurement.

Nevertheless, photon-counting detector (PCD) based on the Medipix3RX chip is not yet ready for usage in clinical CT due to few reasons. First, the detector element made out of silicon will pose a problem to detect high-energy X-ray photons. Silicon is has poor detector efficiency at high energy levels [64]. In this study, the X-ray tube was operated at 60kVp; however typical scans in clinical radiology employ tube voltage in the range of 80kVp to 140kVp. One workaround to this problem is to use cadmium telluride (CdTe) as the detector element instead of silicon. CdTe is reported to have a high detector efficiency of about 88% at 100kVp (detector thickness ∼ 2 mm); thus is suitable for operation in the human diagnostic X-ray range [115, 116]. There exists Medipix3 assembly using CdTe as detector material, but it was not available for use in this work. Second, there is the high-flux problem, which is a common problem for PCDs. In modern CT system, flux rates are as high as 10^9 photons s^{-1} mm^{-2} in the center beam. Most PCDs have electronics that may not cope with the high flux rate, resulting in pulse pileup that affect the count rate and ultimately leads to a degradation of the spectral measurements. For Medipix3RX, the effect would be worse especially if operated in the Charge Summing Mode (CSM) [117].

Despite all of the limitations, PCD based on the Medpix3RX chip has great potential. If these technical hurdles can be overcome and such detectors can be deployed clinically, one could foresee the integration of spectral information not only to improve the diagnostic image quality, but also to aid diagnostic procedures.

4.8.2 Applications

Metal Artifact Reduction

In this work, an algorithm that combines spectral information and statistical reconstruction to reduce metal artifacts caused by the presence of high Z-materials is proposed. It is demonstrated that the projection data generated from photon-counting detectors (PCD) can be accurately decomposed into several basis functions, providing additional knowledge on the components in the underlying scanned object. This information can be used as a prior into a penalized maximum log-likelihood iterative reconstruction, in which the true spatial location and density are enforced and corrected. The algorithm was tested with Monte Carlo simulated data of jaw phantoms that contain various shapes of dental implants. The results from the algorithm are promising, where a significant reduction of streaks in the image, elimination of bright and dark shadings, and the preservation of edges and anatomical details especially near the metal implant can be seen.

Previous work has shown the advantages of model-based reconstruction [91], in which prior information is incorporated into a reconstruction process to reduce artifacts as a result of the presence of high-Z number materials. The KCR method yields a significant reduction of streaks as well as the dark shades near the metal, while preserving the anatomical information in the background. Nevertheless, CAD based reconstruction is very dependent on the exact information of the component in the image; an inaccurate prior may result in a less than optimal image as confirmed by the findings in Figure 4.15. This problem will be challenging in daily clinical routines as the metal components are often deformed due to rough surgical procedure or due to prostheses experiencing significant wear prior to imaging. The SPIR algorithm can overcome this difficulty by performing material decomposition on the projection data and consequently the location and shape of the metal component can be detected with minor discrepancies, as evident by the images in Figure 4.12. Further, the ability to accurately detect any shape of implant indicates that the proposed method can be generalized and extended to other part of the body such as extremity or spine.

Another feature of the algorithm is the ability to generate pseudo-monochromatic projection data from the decomposed sinogram. This is particularly advantageous as this minimizes errors during reconstruction, thus producing images

of high quality. In CT the attenuation of photons is material and energy dependent as shown in (4.1). Lower energy photons are more rapidly absorbed than higher energy photons. However, in most CT reconstruction algorithm the X-ray energy is averaged; thus the energy-dependency is neglected, causing the occurrence of beam hardening artifacts [15, 47, 90]. This error can be mitigated in multi energy CT or Spectral CT due to the more accurate modeling of the energy and material dependence of the X-ray attenuation, which enables the calculation of a pseudo-monochromatic projection data at different energy levels.

The successfulness of the material decomposition technique is limited to the information of chemical composition of the metal implant. In this work, metal implant made out of gold that has a distinctive k-edge property was used. Implants made out of a mixture of several unknown metal may pose a challenge to the decomposition technique. However, this technique works well as long as the chemical composition of the metal is known beforehand so that accurate basis functions are chosen for decomposition.

Low-Concentration Iodine Detection

The ability to generate material-specific images via material decomposition technique is promising because it enables applications of low-concentration of contrast medium such as iodine in clinical CT. However, the imaging of low concentrations of contrast medium (CM) inherently leads to a low signal levels. Additionally, the decomposition method induces artificial noise in the image that further reduces the signal-noise-ratio (SNR) in the image. For these reasons, an algorithm is proposed to reduce the noise in the image; while at the same time improve the appearance of the CM in the image. Results in this study indicate that the algorithm is not only able to deliver better image quality, but also has the capability to preserve the contrast of the CM in the image.

One drawback of this study is that the phantom used contains only iodine and water. In reality, a human body is more complex as it is made out of various other materials such as adipose tissues, soft tissues and bones. The presence of these different materials may pose problems for the material decomposition technique due to low K-edge energy of iodine (33.2 keV), which also lies in the energy range where photoelectric absorption and Compton scattering are dominant. A more suitable

choice of contrast medium should have K-edge energy high enough (>50 keV) that produces high signal even at low concentrations. One contrast medium that has recently been seen as attractive for use as contrast agent is ytterbium [118]. Ytterbium has shown to have low toxicity, is highly available, and more importantly has the K-edge of 61.3 keV that produces high signal levels [111].

Nevertheless, this study has shown that the application of low iodine concentration is feasible with the combination of material decomposition technique and the statistical iterative reconstruction of the decomposed image.

Multi-material K-edge Imaging

The K-edge imaging technique based on the accurate positioning of the threshold is a simple method of detecting different materials in the scanned object. Results shown in Figure 4.20 shows that silver and iodine can be distinguished from each other and other materials by simply subtracting the reconstructed images before and after the K-edge of each material. This technique, while simple, is impractical for several reasons. First, the materials to be distinguished need to be known beforehand. Second, the successfulness of the technique is highly dependent on the accurate positioning of the thresholds, which need to be set before the acquisition. This means, once the acquisition is done, there is no possibility of adjusting the energy windows to suit the K-edge energy of the materials of interest.

A more realistic approach is to decompose the projection data into several basis materials of choice. Although the choice of material must also be known beforehand, the placement of the thresholds (or the energy window) has only a minimal impact in decomposition process [10]; thus the material decomposition can be applied even after the acquisition is done regardless of the energy window. Nevertheless, this approach has several weaknesses too in that the accurate modeling of the detection process is vital for the accuracy of the decomposition. Information on the spectrum generated by the tube and the spectral response of the detector need to be characterized for a successful decomposition. For Medipix3RX, this information is not readily available and need to be measured, but the characterization of the detector is a complex matter. In order to characterize the spectral response of the detector, monochromatic beam is needed, which can be only generated by a synchrotron [119], which itself is not widely available.

Nonetheless, the successfulness of multi-material imaging will spur the developments of new novel contrast agents, which are more targeted and disease-specific. Ytterbium and gold for example have high K-edge energies, 61.1keV and 80.1keV respectively, and have shown to enhance the appearance of diseased tissue in the image [120]. A 'cocktail' of contrast media containing these two materials and iodine can be administered in a patient; thus a different level of tissue enhancement and the detection of the various diseases can be obtained in a single scan. This will result to a significant reduction of radiation dose exposure. Of course the creation of this 'cocktail' must be first subjected to vigorous toxicity and biological compatibility test, that make take years before such scan is possible.

4.9   Summary

This chapter describes the principle of photon counting detector (PCD) based spectral CT (SCT) and outlines the various benefits of this CT imaging technique. The additional information provided by SCT can be used in many clinical applications that aid diagnostic procedures. Further, the quantum efficiency of PCD produces images of high quality; while at the same time enables low-radiation dose acquisition protocols. However, the unavailability of a clinical scanner with PCD hampers the development of new clinical application based on SCT. Due to this reason, simulation tools were developed to assist research and development of new clinical applications. The simulation tools have shown to be able to generate projection data from PCD, as shown as in Section 4.3.1. Besides simulation, a PCD detector based on the Medipix3RX chip was also employed to test the practicality of the algorithm and applications developed in this work.

Three possible applications based on SCT were presented, the first of which is to use the additional spectral information to correct for metal artifacts in images. The proposed algorithm utilizes the spectral information to detect the spatial location of the metal and further uses the knowledge of the metal as a prior to a maximum-likelihood iterative reconstruction. Results in Section 4.5.4 show the robustness of the algorithm and the promising prospect of this method for use in clinical routine. The next proposed application is to detect low concentrated iodine. It is shown that this technique is able to distinguish iodine from other materials, while the iodine concentration measurements in Table 4.2 demonstrate the accurateness of the

74

detection process. The feasibility of the algorithm will lead to a possible reduction of iodinated contrast agent usage in CT; hence reduce the incidence of CIN.

Finally, the realization of multi-material k-edge imaging was tested. In this method, the thresholds of the PCD were optimized by placing them before and after the K-edge of a chosen material. The results from this approach demonstrate the possibility of distinguishing k-edge materials; hence open new prospect to the usage of a mixture of contrast agents in a single scan.

Chapter 5

Beyond Medical Purposes

5.1 Introduction

Outside the domain of medical diagnostics, X-ray CT is used for pre-clinical imaging and non-biomedical purposes. Advancements in micro-CT technology with fine spatial resolution up to sub-micrometer has enable imaging of biological specimens and in-vivo small animals. Current pre-clinical imaging researches in small animals includes the development of gating strategies in cardiothoracic imaging [121], characterization of blood pool contrast media [122], visualization of fracture healing [123], and characterization of the phenotype of animal models [124] . Other interesting studies in the molecular imaging domain include the development of novel contrast agents [125] and in the imaging of specimens in molecular level with the help of staining materials. The effectiveness of pre-clinical research is of great interest, as the techniques developed would eventually translate into clinical purposes.

X-ray CT is widely used in medical diagnostic, as it is non-invasive, accurate, and fast, yet provides information of the internal structure of the scanned object. The same objective is strived in industrial inspections, which is to non-destructively visualize and inspect the internal structure in an object [126, 127]. Most of this industrial examination, known as non-destructive testing (NDT), utilizes conventional methods such as radiography and acoustic illumination [128], while the usage of X-ray CT is not as widespread as in medical CT. Nevertheless, the basic principle behind medical CT imaging is the same as in industrial CT imaging; thus in theory, algorithms developed for general medical CT purposes can also be use for industrial purposes. In fact, algorithms designed for medical CT can be specifically optimized to industrial applications because industrial objects have more detailed information available in the form of mathematical models and mechanical drawings [128]. This information can be utilized as a priori in many of these algorithms to improve image quality as well as material detection.

This work tries to exploit the similarities between micro-CT, industrial CT and medical CT by examining the applicability of the multi-energy CT algorithms and

techniques developed in the previous chapter in solving pre-clinical and industrial problems. In particular, is to analyze the capability of the material decomposition technique to distinguish different types of materials in the scanned object.

5.2   Xradia Versa XRM-500 Imaging System

The VersaXRM-500 (Carl Zeiss X-ray Microscopy, Pleasanton, CA, USA) is a state-of-the-art 3D X-ray imaging system designed for non-destructive micro tomography. It has a fine spatial resolution up to sub-micrometers and enables imaging of wide range of sample sizes for various applications such as in material science, geo sciences, and life sciences.
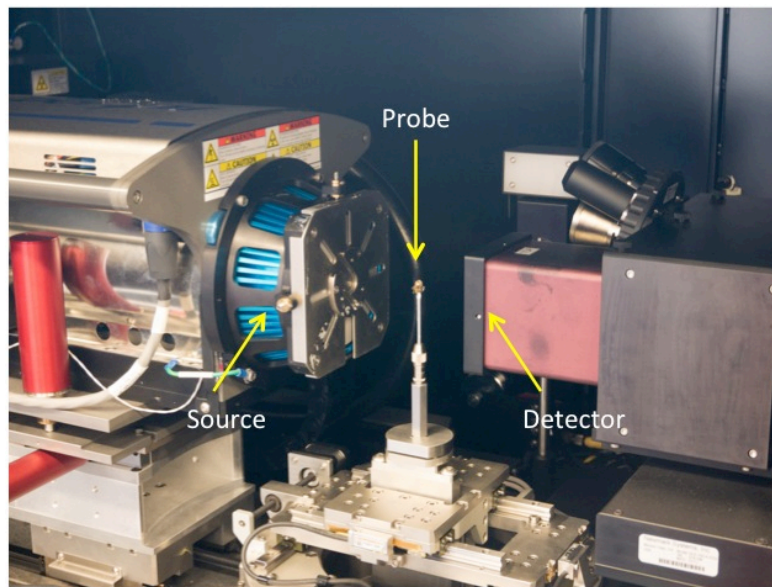
Figure 5.1: The X-Radia VersaXRM-500 setup. It consists of the X-ray source, the sample holder, the detector, and a turret of objectives. Picture courtesy of Jolanda Schwarz, E17 TUM.

Similar to other micro-CT system, the Versa XRM-500 consists of a source, a sample holder, and a detector equipped with of a turret of objective for magnification. The system uses a special type of transmission target at the source that produces X-ray beam with small focal size. Small focal size is desirable in micro-CT as it enables high-resolution tomography. In between the source and the detector is the sample holder. The sample holder has high-precision motors that allow an exact positioning of the sample in the sub-micron range. In contrast to most micro-CT systems, the setup provides a movable detector and a movable source, which facilitates measurements of samples of different sizes and to adapt the FOV of the detector to

different image sizes. The turret of objective is able to produce variable magnification (0.39x, 4x and 20x). After the conversion of X-ray into photon lights, the objectives magnify the converted lights via conventional optical microscope methods. Finally, the CCD camera collects the signal and produces an image of the object.

5.2.1 System Characterization

The knowledge of the source spectrum and detector response is essential for many multi-energy imaging analyses. In this work, the source spectrum was characterized by means of measuring the spectrum as well as using an open source simulation tool pyPENELOPE. Figure 5.2 shows the plot of the measured and simulated X-ray spectrum at 80kVp. One can see that the simulated spectrum has a relatively similar spectrum shape as the measured, but with a slightly higher mean energy. A calibration factor has to be introduced for every energy spectrum to correct for this discrepancy, but this process is time consuming and in unusable if the spectrum is then filtered. Additionally, a special detector is needed to measure the higher-energy spectra. Due to this reasons, the spectrum used in the analysis is simulated with pyPENELOPE.
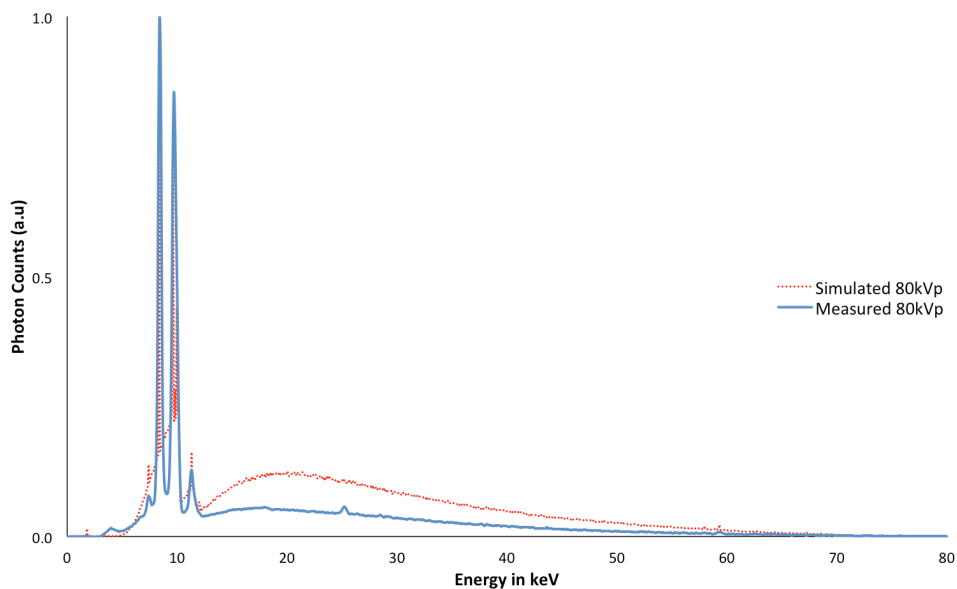
Figure 5.2: The simulated and measured X-ray spectrum at 80kVp for the X-Radia VersaXRM-500 system. Both have approximately similar spectrum shape, but the measured spectrum has low mean spectrum energy.

While the source spectrum can be measured, the characterization of the detector response is not as straightforward. As the VersaXRM is a commercial

product, the scintillator materials and thicknesses are not exactly known. Details on the scintillator material and thickness would allow simulations of the detector to estimate the detector response.

5.3 Applications

5.3.1 Staining of Biological Specimens

The staining of biological samples is a widely used method in biology and medicine. The main purpose of this method is to enhance contrast in microscopic image and to highlight fine structures in tissues and in cells. Examples of types of staining media and their purpose are iodine for starch indicator [129], methylene blue for enhancement of cell nuclei [130], ethidium bromide for staining of unhealthy cells [131], and phosphotungstic acid (PTA) for connective tissues [132]. Staining media such as iodine and PTA have high effective Z-numbers relative to biological tissue, thus is suitable for multi-energy imaging.

In this study, a sample of mouse testicles was stained with iodine solution and PTA. Both of the solutions were diluted with ethanol to have concentration of 5% for iodine and 10% for PTA. The mouse testicle was first stained with iodine and then was left in the PTA solution overnight. Then, dual-energy acquisitions were done with a tube voltage of 60kVp filtered with 1.46 mm of SiO_2 for the low energy spectrum and 160kVp filtered 3.5mm aluminum (Al), 2mm Teflon and 0.4mm tin (Sn). The reason for the application of the filters was to increase the spectral separation between the two spectra. In addition to the mouse testicle, two tubes of the solutions were also included in the scanned phantom. After acquisition, the projection data and the reconstructed images were subjected to the projection-based and image-based material decomposition techniques, respectively.

Results

The reconstructed images from the two spectra are shown in Figure 5.3. Comparing the two images, one can see that in the low-energy image, iodine has better contrast than in the high-energy image. This can be attributed to the effective energy of the low-energy spectrum being closer to the K-edge of iodine.
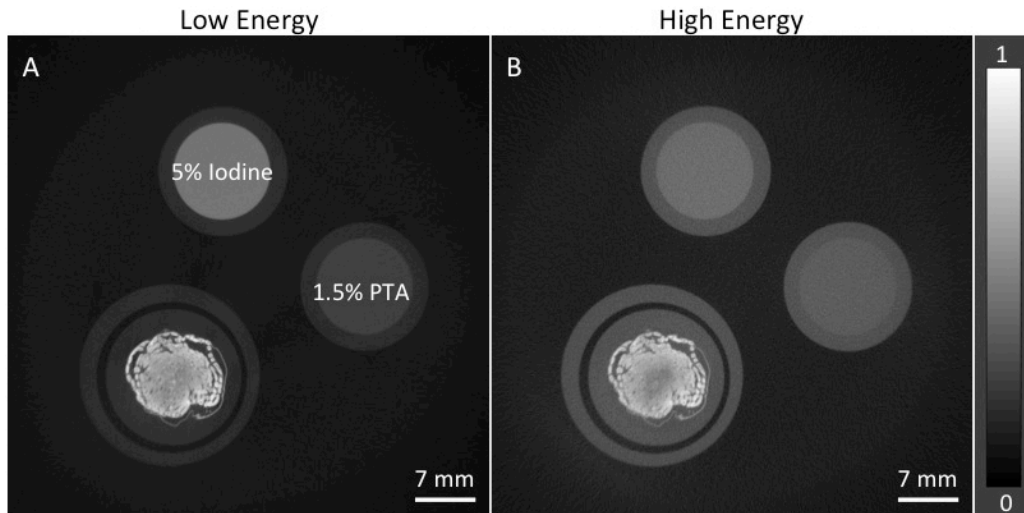
Figure 5.3: The low- (A) and high-energy (B) images of the mouse testicle and the iodine and PTA tubes of the low- and high-energy. Both images are normalized to 1, with WL of 0.5 and WW of 1.0

Figure 5.4 illustrates the results for both image-based and projection-based material decomposition techniques. In general, both techniques were able to distinguish iodine from other components in the image, but the PTA solution could not be differentiated from other materials. One reason for this is the low concentration of PTA in the falcon tube and in the sample, which makes it difficult for the algorithm to distinguish PTA. Another further observation is that the biological specimen almost contains iodine with only traces of PTA can be seen at the peripherals of the specimen. This can be explained by the fact that PTA has big molecules and cannot be easily absorbed by the sample, whereas iodine can easily diffuse into the sample. This finding is in line with results from other studies [133]. One way of increasing the absorption of PTA is to cut open the sample before the staining process to allow better diffusion.
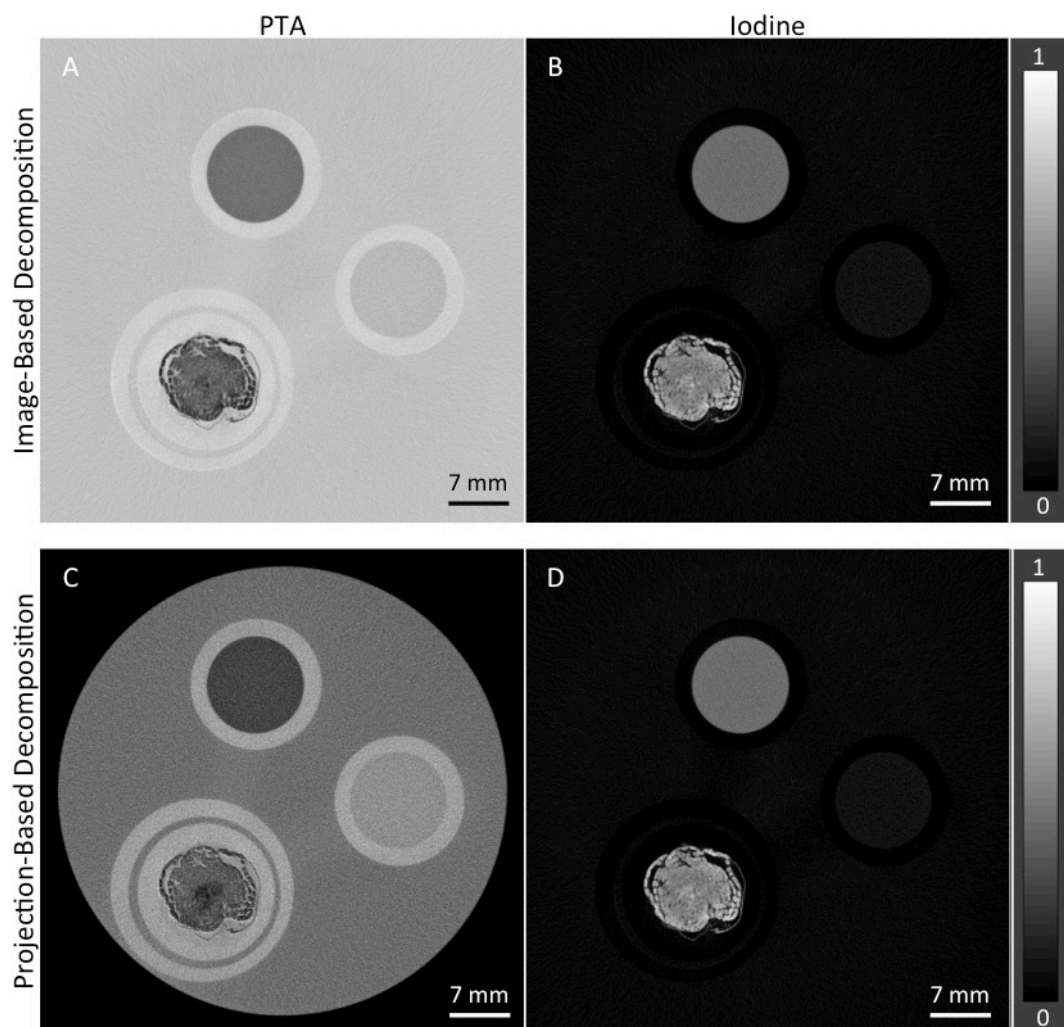
Figure 5.4: The decomposed images from both the image-based (A, B) and projection-based (C, D) material decomposition technique. One can see that while iodine can be accurately distinguished from other components in the image, PTA could not be differentiated. This may be due to the low concentration of PTA in the tube. All images are normalized to 1, with WL of 0.5 and WW of 1.0

5.3.2 Quantification of Concentration in Solution

For the quantification experiment, a phantom consisting of three falcon tubes filled with 15% concentration of sodium chloride (NaCl) was used. The falcon tubes were held using a placeholder made out of polyoxymethylene (POM). The phantom was scanned twice with two X-ray energies – the first with tube voltage of 60kVp filtered with 1.46 mm of SiO_2, while the second with 160kVp with 5.0 mm of CaF filter. After the dual-energy acquisitions, the projection data and reconstructed images were decomposed to two basis functions – NaCl and POM. The concentration of the NaCl and iodine in each phantom was quantitatively measured.

Results

Both the image-based and the projection-based material decomposition techniques were able to correctly distinguish NaCl from POM. Figure 5.5 illustrates the decomposed images from the image-based technique. While both techniques were able to accurately detect NaCl, the results from the concentration measurements show that the image-based decomposition technique delivers better result in comparison to the projection-based. The measured NaCL concentration is more accurate, with only a relative difference of 6 – 8% from the true value, as can be seen in Table 5.1.
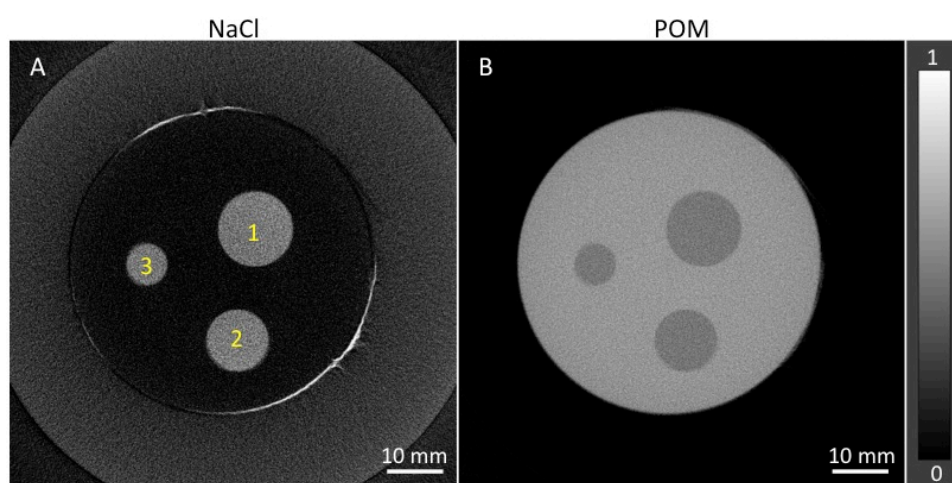
Figure 5.5: The result from the image-based material decomposition technique. It can be seen that NaCl is accurately detected and distinguished from the POM placeholder. The projection-based technique also delivers the same decomposed images; thus is not shown. Both images were normalized to 1.0 and are shown with WL 0.5 and WW 1.0.

The inaccuracy of the projection-based technique can be attributed to the inaccurate modeling of the acquisition process. In the data analysis, the source spectrum was simulated, while the details on the detector were not known.

Table 5.1: The results of the iodine concentration quantification. The image-based technique delivers more accurate iodine concentration measurements, in comparison to the projection-based technique

Target	True Concentration (%)	Measured Concentration			
		Image-Based		Projection-Based	
		Mean (%)	Difference	Mean (%)	Difference
1	15	13.8	8.0	11.22	25.2
2	15	14.1	6.0	11.14	25.7
3	15	13.7	8.7	11.00	26.7

5.3.3 Non-Destructive Testing

Non-Destructive Testing (NDT) is one of the most widely use technique in industrial inspections. NDT techniques are of particular interest due to its ability to visualize the internal structure of a sample without causing any damage; thus is cost-efficient and less time consuming. Common NDT techniques include ultrasonic illumination, magnetic-particle, and radiographic. Until recently, X-ray CT technique was not widely used in NDT due to technical limitations of CT scanners such as small detector area relative to normal industrial objects and the limited spatial resolution of the detector. However, with new detector technology, acquisition techniques, and reconstruction algorithm, industrial CT has begin to attract more interest among researchers in the field [134, 135].

The additional spectral information obtained from multi-energy CT can be exploited for examining the internal structure for industrial or construction objects. In this work, the applicability of the material decomposition techniques in detecting the constituents of a concrete block is investigated. The sample was first subjected to dual-energy acquisitions with a tube voltage of 60kVp filtered with 1.46 mm of SiO_2 for the low-energy scan and 160kVp filtered with 5.0 mm of CaF for the high-energy scan. Subsequently, the reconstructed images from the low-energy and high-energy scans were decomposed into three basis materials. The components of the material and their ratios are given in Table 5.2

Table 5.2: The components of the sample and their ratios.

Name	Formula	Density (g/cm^3)	Ratio
Lime	CaO	3.37	53.4
Silicon Dioxide	SiO_2	2.65	32.8
Water	H_2O	1.0	13.8

Results

The reconstructed images from the projection data are illustrated in Figure 5.6. One can see that the VersaXRM-500 micro-CT system is able to deliver high-resolution axial images of the concrete sample. Fine details of the structures in the image can be seen, while at the same time the different materials inside the sample is clearly shown.
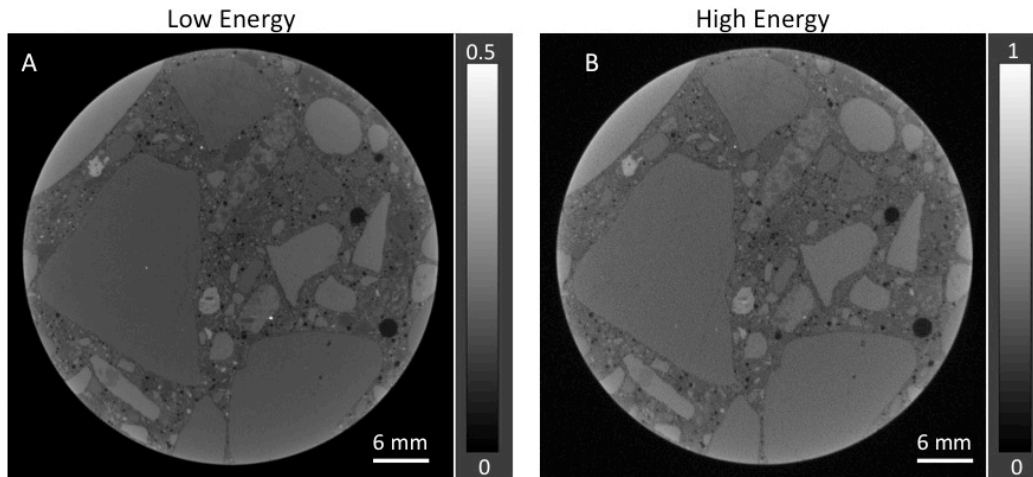
Figure 5.6: The axial slice of the concrete sample. Details of the structure and the constituent materials can be clearly seen in the images. Image A is shown with WL 0.25 and WW 0.5, while image B has WL 0.5 and WW 1.0.

Dead pixels in the detector contribute to the appearance of ring artifacts in the image. In order to avoid the occurrence of ring artifacts, the sample holder was constantly moved during the whole period of acquisition. The shifting of the sample holder, also known as the typewriter concept, is recorded by the system and can be corrected during the image reconstruction process. However, additional vibration can occur from the system but this is not recorded. The combination of the deliberate shifting and the internal vibration aggravates the misalignment between the low-energy and high-energy images. Due to this reasons, both images were registered prior to the material decomposition technique. Figure 5.7 shows the decomposed images of the concrete sample. The components in the sample have effective Z-numbers that are quite low and close to each other. As a result, the only small differences of attenuation coefficients between the materials would pose problems for the decomposition technique.
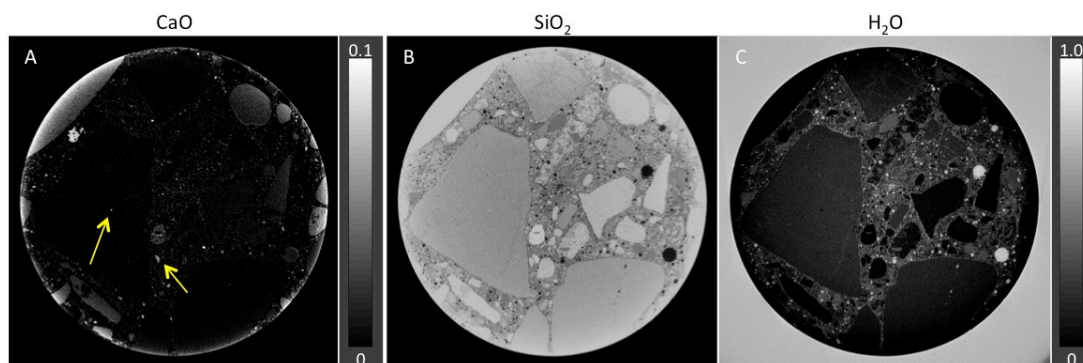
Figure 5.7: The decomposed images of the concrete sample using the image-based technique. Image A shows the component CaO, image B the material SiO2, and image C water. Image A has WL 0.05 and WW 0.1, while image B and C have WL 0.5 and WW 1.0.

5.4 Discussions

5.4.1 Xradia VersaXRM-500

The Xradia VersaXRM-500 has shown to be capable of acquiring high resolution scans of samples. Fine structures can be clearly visualized, while details of the different components can also be seen, as shown in Figure 5.6. The system is able to perform multi-energy scans at different tube voltage settings, while the use of filters can further increase the spectral separation between two spectra. In most of the studies done in this work, the material decomposition techniques were able to decompose the projection data or the reconstructed images to several basis functions. However, the projection-based decomposition performed worse than the image-based technique. This can be attributed to the lack of accurate input for the modeling of the acquisition process. Detail such as the detector efficiency was absent, while the source spectrum could only be simulated, especially for the higher energy spectrum. Therefore, there is a need to characterize the system further.

One particular problem with the system is the source instability. During acquisitions, a drop of tube current may occur after a certain period of measurements. This phenomenon can be seen in Figure 5.8 and may result in artifacts in the reconstructed volume. One way of addressing this issue is by calibrating the projections with the reference projection taken at the corresponding source power and by adjusting the gray values between the projections. However, the downside of this method is that the comparability to another measurement with the same tube voltage is reduced.

85

Figure 5.8: The illustration of the tube current drop. In this acquisition, there is a change in intensity as shown in box A, due to the drop in tube current. This lasted for several projections before the condition normalized again, as can be seen in B

Another type of instability is mechanical instability of the system. A typical scan may take long period of time to complete, during which slight vibration from the system and unintentional movement of sample may occur. While the VersaXRM-500 system does record any sample holder movement during the acquisition process and correct this during the reconstruction of the projection data, misalignment can still occur between two sets of dual-energy scans due to these reasons. The misalignment poses problem for both the image-based and projection-based material decomposition technique. In the image-based technique, this problem can be overcome by registering low-energy images to the high-energy image prior to decomposition; however, the process is not as straightforward in the projection space.

5.4.2 Pre-Clinical Applications

In the biological specimen staining experiment, it has been demonstrated that the multi-energy projection data and reconstructed images acquired using micro-CT system can be subjected to the material decomposition techniques. In this work, it has been shown that two different staining solutions PTA and iodine can be distinguished. Additionally, the micro-CT data can also be subjected to material decomposition techniques in order to quantify the concentration NaCl.

In the detection and quantification studies, both the projection-based and image-based material decomposition techniques were tested. Both methods have been shown to be able to detect and distinguish materials. However, in the quantification,

the image-based technique delivers superior results in comparison to the projection-based technique. The poor performance of the projection-based technique proves that this technique works best if the details on the accurate source spectrum input and detector efficiency information are available.

5.4.3 Non-Destructive Testing

The high resolution of the Xradia VersaXRM-500 micro-CT machine enables the detail visualization of the internal structure of the concrete sample. From the reconstructed images, one can not only see the shape of the constituent materials, but also see the air bubbles in between the materials. Such detail visualization is important, especially in analyzing the ratio of materials and determining the strength of the sample.

In this study, only the image-based material decomposition technique was used. The misalignment between the acquired projection data (see Figure 5.9) prevents the projection-based algorithm to accurately decompose the sample. The registration of two data in the projection domain is very complicated. On the other hand, it is easier in the image domain; thus this problem can be overcome in the image-based method. This difficulty implies that although in theory the projection-based technique should deliver superior decomposition results as the modeling of the acquisition process, it is sensitive to the quality of the data input.
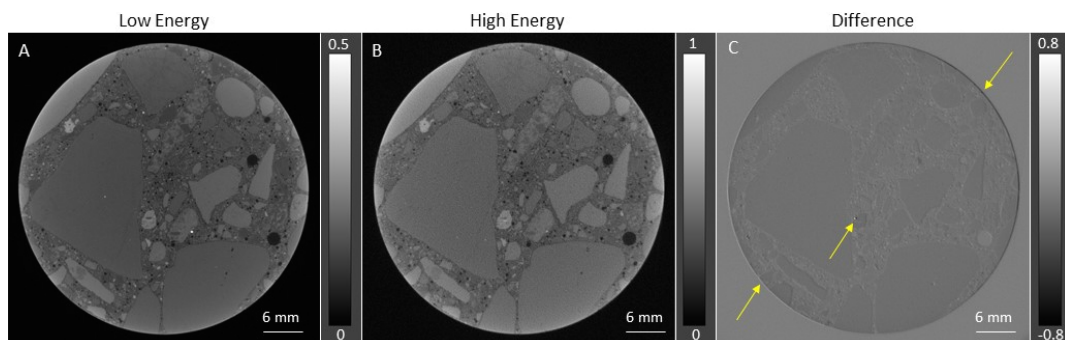
Figure 5.9: The images of the concrete sample for (A) low-energy, (B) high-energy image, and (C) the difference of both. The arrows in C points to the artifacts due to the misalignment between the low- and high-energy images.

The micro-CT's ability to image fine structures as well as the combination of multi-energy CT has much potential, especially in detecting valuable materials in huge chunk of stones. For instance, goldsmith can know which part of the stone has gold or diamond, thus optimize the method of extracting the stones.

5.5 Summary

This chapter demonstrates the prospect of expanding applications and algorithms developed for clinical CT beyond clinical purposes such as for pre-clinical studies and industrial applications. The results from experiments shown in this work show the potential benefit of multi-energy CT for pre-clinical and industrial purposes. The Xradia Versa XRM-500 machine has the capability to assist the research and development of application-specific algorithms, but more work has to be done to characterize the system. The availability of detailed information on the source and detector response, for instance, can lead to more advance studies on material sciences using the system.

Chapter 6

Discussions and Future Outlook

6.1 Dual-Energy CT

Dual-energy CT has been around in the clinical arena for some time and is widely used in diagnostics. Although there are already various applications available for medical purposes that can aid the diagnostic processes in clinical routines, there are still more applications that can be developed to take advantage of the additional spectral information provided. For instance is the reduction of beam-artifacts in CT images that leads to the improvement of automated detection of polyps and lesions in CT colonoscopy.

Another potential application is the detection of low-concentration iodine in patients. The ability to detect and subsequently enhance low-concentration iodine signal in image is clinically desirable as it may lead to the reduced usage of iodinated contrast agent, which in turn reduces the incidence of CIN, especially among older patients. The detection of low-concentration iodine is challenging, as the signal can be too weak to be detected, resulting in poor SNR of the contrast medium. One approach is to increase the radiation dose in order to increase the signal of iodine, while at the same time reduce the appearance of noise in the image. This approach can be done, especially in older patients due to the fact the probability that this group of patients suffering from fatal CIN far outweighs the harm of the extra radiation received.

6.2 Spectral CT

Spectral CT using photon-counting detectors (PCD) has great potential and offers many advantages, especially in delivering higher quality images and more diagnostic information in comparison to conventional X-ray CT. In a conventional detector, incident photons are converted to optical photons at the scintillator and these signals are further amplified by the photomultiplier. These analog signals are then integrated and converted to digital signals. The whole detecting and amplification processes are inefficient, while the digitization may induce some noise in the signal sampling. On the other hand, PCD counts single photons, thus is already discrete in nature. The concept of electron holes avoids amplification and conversion process,

making photon-counting detectors efficient and 'noise-free'. This has several advantages. Firstly, due to the 'absence' of electronic noise at the detector, low dose acquisition protocols are possible without compromising the quality of the CT image. Secondly, low energy photons that contain valuable contrast information can be correctly detected. In an energy-integrating detector, low-energy photons may get 'mixed' with electronic noise. However, in energy resolving single photon-counting detector such problem does not arise, thus valuable information contain in the low-energy photons can be preserved.

The additional information provided by SCT is valuable for a variety of clinical applications - for example quantitative K-edge imaging [58], the usage of high-Z contrast agents [136, 137] and plaque detection and characterization [137, 138]. Nevertheless, photon-counting spectral CT scanners are still unavailable in the clinical arena due to several technical limitations. The slow read-out rate restricts the ability of PCD in coping with high X-ray flux, causing in pulse pile-up and photons wrongly discriminated at the detector. Currently, photon-counting detectors are able to measure photon flux levels up to $50Mcps/mm^2$ [59, 138]. In comparison, photon flux up to $10Gcps/mm^{-2}$ is common in conventional CT. In addition, pulse splitting due to K-fluorescence from Cd (26.7 keV) or Te (37.8 keV) atoms of the detector elements will also contribute to inaccurate photon counting and discrimination. Many techniques and methods are in development to overcome these technical limitations [59]. If these technical hurdles can be overcome and such detectors can be deployed clinically, one could foresee the integration of spectral information to improve the diagnostic image quality while possibly reducing the radiation dose to the general patient population.

6.3 Pre-Clinical Purposes

The combination of micro-CT and multi-energy CT has huge prospect for pre-clinical purposes. In this work, two examples were shown, which is the differentiating of two staining solutions and the quantification of the concentration of contrast medium. The development of these applications can provide an alternative to the conventional histological staining of biological specimens.

Further applications for pre-clinical purposes are visualization of tumor growth and metastasis and the assessment of cardiac function in small animals.

Especially for the assessment of cardiac function, the usage of X-ray CT with the appropriate gating is beneficial, as it provides fast, yet accurate and reliable measurements. And with the combination of multi-energy CT, the distribution of contrast medium in the body can be visualized and characterized.

6.4 Industrial Purposes

X-ray CT is used in various industrial purposes such as for component inspection, structural analysis, and metallurgy. It is a great tool, especially for inspecting objects non-destructively. However, most applications are limited to single-energy acquisitions, while spectral analysis is not widespread. It has been shown that algorithm mainly developed for medical CT can also be used for industrial purposes, especially with regards to multi-energy CT. In comparison to medical CT, industrial CT has the advantage that radiation dose is not an issue; thus X-ray projection measurements can be repeatedly done on the same sample. The only drawback to repeat acquisitions is the potential movement of the sample in between scans that may cause misalignment in the projection datasets.

The usage of multi-energy CT in the industrial domain has many advantages and bright prospects. In addition for structural analysis or material inspection, multi-energy CT can be used for detecting and distinguishing materials in a sample. This has benefits, especially for the mining industry. An example of potential application is the detection and quantification of gold in a gold ore or to establish the purity of diamond. Multi-energy CT is advantageous for such purposes as it provides fast and accurate yet cost-efficient solutions to industrial inspections.

Chapter 7

Conclusions

The idea of dual-energy CT (DECT) was first proposed in the late 70s, but it was not until three decades later that CT scanners with dual-energy capabilities were finally deployed in the clinical settings. The introduction of the DECT scanners has spurred many investigations on possible clinical applications that take advantage of the additional spectral information. Although there are already many DECT applications that assist clinicians in diagnosis process, there are still more to be explored. This work has introduced two more promising applications that have proved to be able to improve image quality and aid diagnostics decision in CT colonoscopy.

The development of energy-resolving photon counting detector (PCD) has seen the emergence of Spectral CT as the next big invention in medical imaging. The exciting prospect of SCT using PCD will lead to new techniques in clinical CT that take advantage of the additional spectral information provided. In addition, the high efficiency of PCD enables the reduction of radiation exposure to patients, without compromising the image quality. This work has investigated several aspects of SCT, such as ability to simulate SCT system and decompose scanned object, as well as introduce possible clinical applications. It has been shown that the combination of spectral information and statistical reconstruction can significantly reduce the appearance of metal artifacts in CT image, as well as to detect and enhance the signal from low-concentrated contrast medium in the image. Further, the ability to distinguish more than two materials in an image may lead to the introduction of mixture of contrast agents that can be provide contrast enhancement and detection of diseased tissues in a single scan; thus reducing the need for unnecessary radiation exposure to patients.

In conclusion, multi-energy CT provides many advantages in clinical diagnostics. One could foresee that the impending introduction of SCT will improve the diagnostic image quality while possibly reducing the radiation dose to the general patient population.

Bibliography

[1]   R. E. Alvarez and A. Macovski, "Energy-selective reconstructions in x-ray computerised tomography," *Physics in medicine and biology,* vol. 21, p. 733, 1976.

[2]   L. Lehmann, R. Alvarez, A. Macovski, W. Brody, N. Pelc, S. Riederer, *et al.*, "Generalized image combinations in dual KVP digital radiography," *Medical physics,* vol. 8, pp. 659-667, 1981.

[3]   A. Macovski, R. Alvarez, L. Lehmann, E. Roth, and W. Brody, "Iodine imaging using three energy spectra," in *Conference on Digital Rdiography*, 1981, pp. 140-142.

[4]   F. Kelcz, P. M. Joseph, and S. K. Hilal, "Noise considerations in dual energy CT scanning," *Medical physics,* vol. 6, pp. 418-425, 1979.

[5]   W. A. Kalender, W. Perman, J. Vetter, and E. Klotz, "Evaluation of a prototype dual‐energy computed tomographic apparatus. I. Phantom studies," *Medical physics,* vol. 13, pp. 334-339, 1986.

[6]   R. Zeman, S. Fox, P. Silverman, W. Davros, L. Carter, D. Griego, *et al.*, "Helical (spiral) CT of the abdomen," *AJR. American journal of roentgenology,* vol. 160, pp. 719-725, 1993.

[7]   L. M. Hamberg, G. J. Hunter, E. F. Halpern, B. Hoop, G. S. Gazelle, and G. L. Wolf, "Quantitative high-resolution measurement of cerebrovascular physiology with slip-ring CT," *American journal of neuroradiology,* vol. 17, pp. 639-650, 1996.

[8]   A. Graser, T. R. Johnson, M. Bader, M. Staehler, N. Haseke, K. Nikolaou, *et al.*, "Dual energy CT characterization of urinary calculi: initial in vitro and clinical experience," *Investigative radiology,* vol. 43, pp. 112-119, 2008.

[9]   A. Graser, T. R. Johnson, H. Chandarana, and M. Macari, "Dual energy CT: preliminary observations and potential clinical applications in the abdomen," *European radiology,* vol. 19, pp. 13-23, 2009.

[10]   E. Roessl and R. Proksa, "Optimal energy threshold arrangement in photon-counting spectral x-ray imaging," in *Nuclear Science Symposium Conference Record, 2006. IEEE*, 2006, pp. 1950-1954.

[11]   P. M. Shikhaliev, T. Xu, and S. Molloi, "Photon counting computed tomography: concept and initial results," *Medical physics,* vol. 32, pp. 427-436, 2005.

[12]   T. M. Buzug, *Computed tomography: from photon statistics to modern cone-beam CT*: Springer, 2008.

[13]   W. Cong and G. Wang, "X-ray scattering tomography for biological applications," *Journal of X-ray Science and Technology,* vol. 19, pp. 219-227, 2011.

[14]   J. Hsieh, *Computed Tomography Principles, Design, Artifacts, and Recent Advances*: Wiley, 2009.

[15]   J. A. Fessler, "Statistical image reconstruction methods for transmission tomography," in *Handbook of Medical Imaging, Volume 2. Medical Image Processing and Analysis*, ed Bellingham, WA: SPIE Press, 2000.

[16]   A. Fehringer, T. Lasser, I. Zanette, P. B. Noël, and F. Pfeiffer, "A versatile tomographic forward-and back-projection approach on multi-GPUs," in *SPIE Medical Imaging*, 2014, pp. 90344F-90344F-7.

[17]   P. B. Noël, B. Renger, M. Fiebich, D. Münzel, A. A. Fingerle, E. J. Rummeny*, et al*., "Does iterative reconstruction lower CT radiation dose: evaluation of 15,000 examinations," *PLOS ONE,* vol. 8, p. e81141, 2013.

[18]   G. J. Gang, J. Lee, J. W. Stayman, D. J. Tward, W. Zbijewski, J. L. Prince*, et al*., "Analysis of Fourier-domain task-based detectability index in tomosynthesis and cone-beam CT in relation to human observer performance," *Med Phys,* vol. 38, pp. 1754-68, Apr 2011.

[19]   S. Richard, J. H. Siewerdsen, D. A. Jaffray, D. J. Moseley, and B. Bakhtiar, "Generalized DQE analysis of radiographic and dual-energy imaging using flat-panel detectors," *Medical physics,* vol. 32, pp. 1397-1413, 2005.

[20]   J. P. Johnson, J. Lo, T. Mertelmeier, J. S. Nafziger, P. Timberg, and E. Samei, "Visual image quality metrics for optimization of breast tomosynthesis acquisition technique," in *SPIE Medical Imaging (pp. 65150P-65150P). International Society for Optics and Photonics.*, 2007.

[21]   S. N. Friedman, G. S. K. Fung, J. H. Siewerdsen, and B. M. W. Tsui, "A simple approach to measure computed tomography (CT) modulation transfer function

(MTF) and noise-power spectrum (NPS) using the American College of Radiology (ACR) accreditation phantom," *Medical Physics,* vol. 40, May 2013.

[22]   J. H. Siewerdsen, L. E. Antonuk, Y. El-Mohri, J. Yorkston, W. Huang, and I. A. Cunningham, "Signal, noise power spectrum, and detective quantum efficiency of indirect-detection flat-panel imagers for diagnostic radiology," *Medical Physics,* vol. 25, pp. 614-628, May 1998.

[23]   X. Tang, Y. Yang, and S. Tang, "Characterization of imaging performance in differential phase contrast CT compared with the conventional CT: spectrum of noise equivalent quanta NEQ(k)," *Med Phys,* vol. 39, pp. 4467-82, Jul 2012.

[24]   J. T. Payne, "CT radiation dose and image quality," *Radiologic clinics of North America,* vol. 43, pp. 953-962, 2005.

[25]   A. Berrington de Gonzalez and S. Darby, "Risk of cancer from diagnostic X-rays: estimates for the UK and 14 other countries," *Lancet,* vol. 363, pp. 345-51, Jan 31 2004.

[26]   P. Herzog and C. T. Rieger, "Risk of cancer from diagnostic X-rays," *Lancet,* vol. 363, pp. 340-1, Jan 31 2004.

[27]   P. Prakash, M. K. Kalra, A. K. Kambadakone, H. Pien, J. Hsieh, M. A. Blake*, et al.*, "Reducing abdominal CT radiation dose with adaptive statistical iterative reconstruction technique," *Investigative radiology,* vol. 45, pp. 202-210, 2010.

[28]   A. K. Hara, R. G. Paden, A. C. Silva, J. L. Kujak, H. J. Lawder, and W. Pavlicek, "Iterative reconstruction technique for reducing body radiation dose at CT: feasibility study," *American Journal of Roentgenology,* vol. 193, pp. 764-771, 2009.

[29]   P. J. La Rivière, "Penalized-likelihood sinogram smoothing for low-dose CT," *Medical physics,* vol. 32, pp. 1676-1683, 2005.

[30]   S. Leng, L. Yu, J. Wang, J. G. Fletcher, C. A. Mistretta, and C. H. McCollough, "Noise reduction in spectral CT: reducing dose and breaking the trade-off between image noise and energy bin selection," *Medical physics,* vol. 38, pp. 4946-4957, 2011.

[31]   A. Primak, J. R. Giraldo, X. Liu, L. Yu, and C. McCollough, "Improved dual-energy material discrimination for dual-source CT by means of additional spectral filtration," *Medical physics,* vol. 36, pp. 1359-1369, 2009.

[32]   B. Heismann, B. Scmidt, and T. Flohr, *Spectral Computed Tomography*: SPIE Bellingham, WA, 2012.

[33]   J. G. Fletcher, N. Takahashi, R. Hartman, L. Guimaraes, J. E. Huprich, D. M. Hough, *et al.*, "Dual-energy and dual-source CT: is there a role in the abdomen and pelvis?," *Radiologic clinics of North America*, vol. 47, pp. 41-57, 2009.

[34]   M. Petersilka, H. Bruder, B. Krauss, K. Stierstorfer, and T. G. Flohr, "Technical principles of dual source CT," *European journal of radiology*, vol. 68, pp. 362-368, 2008.

[35]   K. J. Engel, C. Herrmann, and G. Zeitler, "X-ray scattering in single-and dual-source CT," *Medical physics*, vol. 35, pp. 318-332, 2008.

[36]   Y. Kyriakou and W. A. Kalender, "Intensity distribution and impact of scatter for dual-source CT," *Physics in medicine and biology*, vol. 52, p. 6969, 2007.

[37]   M. Petersilka, K. Stierstorfer, H. Bruder, and T. Flohr, "Strategies for scatter correction in dual source CT," *Medical physics*, vol. 37, pp. 5971-5992, 2010.

[38]   R. Carmi, G. Naveh, and A. Altman, "Material separation with dual-layer CT," in *Nuclear Science Symposium Conference Record, 2005 IEEE*, 2005, p. 3 pp.

[39]   S. Kappler and S. Wirth, "Comparison of dual-kVp and dual-layer CT in simulations and real CT system measurements," in *Nuclear Science Symposium Conference Record, 2008. NSS'08. IEEE*, 2008, pp. 4828-4831.

[40]   S. Kappler, M. Grasruck, D. Niederlöhner, M. Strassburg, and S. Wirth, "Dual-energy performance of dual kVp in comparison to dual-layer and quantum-counting CT system concepts," in *SPIE Medical Imaging*, 2009, pp. 725842-725842-8.

[41]   M. A. Desai, J. J. Peterson, H. W. Garner, and M. J. Kransdorf, "Clinical utility of dual-energy CT for evaluation of tophaceous gout," *Radiographics*, vol. 31, pp. 1365-1375, 2011.

[42]   X. Liu, L. Yu, A. N. Primak, and C. H. McCollough, "Quantitative imaging of element composition and mass fraction using dual-energy CT: three-material decomposition," *Medical physics*, vol. 36, pp. 1602-1609, 2009.

[43]   J. Schlomka, E. Roessl, R. Dorscheid, S. Dill, G. Martens, T. Istel, *et al.*, "Experimental feasibility of multi-energy photon-counting K-edge imaging in pre-clinical computed tomography," *Physics in medicine and biology,* vol. 53, p. 4031, 2008.

[44]   R. E. Alvarez, "Estimator for photon counting energy selective x-ray imaging with multibin pulse height analysis," *Medical physics,* vol. 38, pp. 2324-2334, 2011.

[45]   P. Stenner, T. Berkus, and M. Kachelriess, "Empirical dual energy calibration (EDEC) for cone-beam computed tomography," *Medical physics,* vol. 34, pp. 3630-3641, 2007.

[46]   R. A. Brooks and G. Di Chiro, "Beam hardening in x-ray reconstructive tomography," *Phys Med Biol,* vol. 21, pp. 390-8, May 1976.

[47]   J. F. Barrett and N. Keat, "Artifacts in CT: recognition and avoidance," *Radiographics,* vol. 24, pp. 1679-91, Nov-Dec 2004.

[48]   M. Liedenbaum, M. Denters, F. Zijta, V. Van Ravesteijn, S. Bipat, F. Vos, *et al.*, "Reducing the oral contrast dose in CT colonography: evaluation of faecal tagging quality and patient acceptance," *Clinical radiology,* vol. 66, pp. 30-37, 2011.

[49]   B. C. Pineau, E. D. Paskett, G. J. Chen, M. A. Espeland, K. Phillips, J. P. Han, *et al.*, "Virtual colonoscopy using oral contrast compared with colonoscopy for the detection of patients with colorectal polyps," *Gastroenterology,* vol. 125, pp. 304-310, 2003.

[50]   N. Petrick, M. Haider, R. M. Summers, S. C. Yeshwant, L. Brown, E. M. Iuliano, *et al.*, "CT Colonography with Computer-aided Detection as a Second Reader: Observer Performance Study," *Radiology,* vol. 246, pp. 148-156, 2008.

[51]   R. M. Summers, L. R. Handwerker, P. J. Pickhardt, R. L. Van Uitert, K. K. Deshpande, S. Yeshwant, *et al.*, "Performance of a previously validated CT colonography computer-aided detection system in a new patient population," *American Journal of Roentgenology,* vol. 191, pp. 168-174, 2008.

[52]   R. M. Summers, "Polyp Size Measurement at CT Colonography: What Do We Know and What Do We Need to Know? 1," *Radiology,* vol. 255, pp. 707-720, 2010.

[53]   J. Näppi and H. Yoshida, "Fully automated three-dimensional detection of polyps in fecal-tagging CT colonography," *Academic radiology,* vol. 14, pp. 287-300, 2007.

[54]   S. Allner, T. Koehler, A. Fehringer, M. Willner, F. Pfeiffer, and P. B. Noël, "Bilateral filtering for X-ray phase-contrast imaging," in *The Third International Conference on Image Formation in X-ray Computed Tomography*, Salt Lake City, UT, USA, 2014.

[55]   P. Fischer, A. Helmich, M. Lindner, N. Wermes, and L. Blanquart, "A photon counting pixel chip with energy windowing," *IEEE Transactions on Nuclear Science,* vol. 47, pp. 881-884, 2000.

[56]   P. M. Shikhaliev, "Computed tomography with energy-resolved detection: a feasibility study," *Physics in medicine and biology,* vol. 53, p. 1475, 2008.

[57]   P. M. Shikhaliev, "Energy-resolved computed tomography: first experimental results," *Physics in medicine and biology,* vol. 53, p. 5595, 2008.

[58]   E. Roessl and R. Proksa, "K-edge imaging in x-ray computed tomography using multi-bin photon counting detectors," *Phys Med Biol*, vol. 52, pp. 4679-96, Aug 7 2007.

[59]   J. P. Schlomka, E. Roessl, R. Dorscheid, S. Dill, G. Martens, T. Istel, *et al.*, "Experimental feasibility of multi-energy photon-counting K-edge imaging in pre-clinical computed tomography," *Phys Med Biol*, vol. 53, pp. 4031-47, Aug 7 2008.

[60]   X. Wang, J. Xu, and E. C. Frey, "Optimization of energy window widths in basis material decomposition using a multi-window photon counting X-ray detector," in *Nuclear Science Symposium Conference Record, 2007. NSS'07. IEEE*, 2007, pp. 3826-3829.

[61]   W. C. Barber, E. Nygard, J. S. Iwanczyk, M. Zhang, E. C. Frey, B. M. Tsui, *et al.*, "Characterization of a novel photon counting detector for clinical CT: count rate, energy resolution, and noise performance," in *SPIE Medical Imaging*, 2009, pp. 725824-725824-9.

[62]   T. G. Schmidt, "Optimal "image-based" weighting for energy-resolved CT," *Medical physics,* vol. 36, pp. 3018-3027, 2009.

[63]   E. Roessl, J.-P. Schlomka, and R. Proksa, "Edge-on semiconductor x-ray detectors-towards high-rate counting computed tomography," in *Nuclear Science Symposium Conference Record, 2008. NSS'08. IEEE*, 2008, pp. 1748-1751.

[64]   C. Herrmann, K.-J. Engel, and J. Wiegert, "Performance simulation of an x-ray detector for spectral CT with combined Si and Cd [Zn] Te detection layers," *Physics in medicine and biology,* vol. 55, p. 7697, 2010.

[65]   K. J. Engel, R. Steadman, and C. Herrmann, "Pulse Temporal Splitting in Photon Counting X-Ray Detectors," *Nuclear Science, IEEE Transactions on,* vol. 59, pp. 1480-1490, 2012.

[66]   R. A. Nasirudin, P. Penchev, K. Mei, E. J. Rummeny, M. Fiebich, and P. B. Noël, "A comparison of simulation tools for photon-counting spectral CT," in *SPIE Medical Imaging*, 2014, pp. 90334W-90334W-6.

[67]   C. Ma, J. Li, T. Pawlicki, S. Jiang, J. Deng, M. Lee*, et al.*, "A Monte Carlo dose calculation tool for radiotherapy treatment planning," *Physics in medicine and biology,* vol. 47, p. 1671, 2002.

[68]   H. Zaidi and M. R. Ay, "Current status and new horizons in Monte Carlo simulation of X-ray CT scanners," *Medical & biological engineering & computing,* vol. 45, pp. 809-817, 2007.

[69]   M. Ay, M. Shahriari, S. Sarkar, M. Adib, and H. Zaidi, "Monte Carlo simulation of x-ray spectra in diagnostic radiology and mammography using MCNP4C," *Physics in medicine and biology,* vol. 49, p. 4897, 2004.

[70]   M. Bazalova and F. Verhaegen, "Monte Carlo simulation of a computed tomography x-ray tube," *Physics in medicine and biology,* vol. 52, p. 5945, 2007.

[71]   J. Peter, D. Gilland, R. Jaszczak, and R. Coleman, "Four-dimensional superquadric-based cardiac phantom for Monte Carlo simulation of radiological imaging systems," *Nuclear Science, IEEE Transactions on,* vol. 46, pp. 2211-2217, 1999.

[72]   W. Kalender, "Monte Carlo calculations of x-ray scatter data for diagnostic radiology," *Physics in medicine and biology,* vol. 26, p. 835, 1981.

[73]   M. Bontempi, M. Bettuzzi, and A. Visani, "Semiempirical simulation of x-ray detectors for imaging applications," *Medical physics,* vol. 39, pp. 7677-7685, 2012.

[74]   I. Kawrakow, E. Mainegra-Hing, F. Tessier, and B. Walters, "The EGSnrc C++ class library," *NRC Report PIRS-898 (rev A),* 2009.

[75]   M. Ljungberg, S.-E. Strand, and M. A. King, *Monte Carlo calculations in nuclear medicine: Applications in diagnostic imaging*: CRC Press, 2012.

[76]   E. Mainegra-Hing and I. Kawrakow, "Fast Monte Carlo calculation of scatter corrections for CBCT images," in *Journal of Physics: Conference Series*, 2008, p. 012017.

[77]   E. Mainegra-Hing and I. Kawrakow, "Variance reduction techniques for fast Monte Carlo CBCT scatter correction calculations," *Physics in medicine and biology,* vol. 55, p. 4495, 2010.

[78]   I. Kawrakow, E. Mainegra-Hing, D. Rogers, F. Tessier, and B. Walters, "The EGSnrc Code System: Monte Carlo simulation of electron and photon transport. NRCC Report PIRS–701. Ottawa, ON: National Research Council of Canada; 2010," ed, 2010.

[79]   M. J. Berger, J. Hubbell, S. Seltzer, J. Chang, J. Coursey, R. Sukumar, *et al.*, "XCOM: photon cross sections database," *NIST Standard reference database,* vol. 8, pp. 3587-3597, 1998.

[80]   D. P. Cormode, E. Roessl, A. Thran, T. Skajaa, R. E. Gordon, J.-P. Schlomka, *et al.*, "Atherosclerotic Plaque Composition: Analysis with Multicolor CT and Targeted Gold Nanoparticles 1," *Radiology,* vol. 256, pp. 774-782, 2010.

[81]   S. Feuerlein, E. Roessl, R. Proksa, G. Martens, O. Klass, M. Jeltsch, *et al.*, "Multienergy Photon-counting K-edge Imaging: Potential for Improved Luminal Depiction in Vascular Imaging 1," *Radiology,* vol. 249, pp. 1010-1016, 2008.

[82]   R. Ballabriga, J. Alozy, G. Blaj, M. Campbell, M. Fiederle, E. Frojdh, *et al.*, "The Medipix3RX: a high resolution, zero dead-time pixel detector readout chip allowing spectroscopic imaging," *Journal of Instrumentation,* vol. 8, p. C02016, 2013.

[83]   R. Ballabriga, M. Campbell, E. Heijne, X. Llopart, and L. Tlustos, "The Medipix3 prototype, a pixel readout chip working in single photon counting mode with improved spectrometric performance," in *Nuclear Science Symposium Conference Record, 2006. IEEE*, 2006, pp. 3557-3561.

[84]   T. Koenig, E. Hamann, S. Procz, R. Ballabriga, A. Cecilia, M. Zuber, *et al.*, "Charge summing in spectroscopic x-ray detectors with high-Z sensors," 2013.

[85]   D. Pennicard, R. Ballabriga, X. Llopart, M. Campbell, and H. Graafsma, "Simulations of charge summing and threshold dispersion effects in Medipix3," *Nuclear Instruments and Methods in Physics Research Section A: Accelerators, Spectrometers, Detectors and Associated Equipment,* vol. 636, pp. 74-81, 2011.

[86]   P. T. Talla, P. Bartl, T. Michel, J. Durst, and G. Anton, "A modified spectrum reconstruction method for the Charge Summing Mode of Medipix3," *Nuclear Instruments and Methods in Physics Research Section A: Accelerators, Spectrometers, Detectors and Associated Equipment,* vol. 633, pp. S128-S130, 2011.

[87]   S. M. Kay, "Fundamentals of statistical signal processing: estimation theory," 1993.

[88]   E. Roessl and C. Herrmann, "Cramér–Rao lower bound of basis image noise in multiple-energy x-ray imaging," *Physics in medicine and biology,* vol. 54, p. 1307, 2009.

[89]   C. O. Schirra, E. Roessl, T. Koehler, B. Brendel, A. Thran, D. Pan, *et al.*, "Statistical reconstruction of material decomposed data in spectral CT," *Medical Imaging, IEEE Transactions on,* vol. 32, pp. 1249-1257, 2013.

[90]   B. De Man, J. Nuyts, P. Dupont, G. Marchal, and P. Suetens, "Metal streak artifacts in X-ray computed tomography: a simulation study," *IEEE Transactions on Nuclear Science,* vol. 46, pp. 691-696, 1999.

[91]   J. W. Stayman, Y. Otake, J. L. Prince, A. J. Khanna, and J. H. Siewerdsen, "Model-based tomographic reconstruction of objects containing known components," *IEEE Trans Med Imaging,* vol. 31, pp. 1837-48, Oct 2012.

[92]   D. Man, "Reduction of metal streak artifacts in x-ray computed tomography using a transmission maximum a posteriori algorithm," 1999.

[93]   G. Wang, D. L. Snyder, J. A. O'Sullivan, and M. W. Vannier, "Iterative deblurring for CT metal artifact reduction," *IEEE Trans Med Imaging,* vol. 15, pp. 657-64, 1996.

[94]   D. D. Robertson, J. Yuan, G. Wang, and M. W. Vannier, "Total hip prosthesis metal-artifact suppression using iterative deblurring reconstruction," *Journal of Computer Assisted Tomography,* vol. 21, pp. 293-298, Mar-Apr 1997.

[95]   T. Koehler, B. Brendel, and K. M. Brown, "A New Method for Metal Artifact Reduction in CT," presented at the The International Conference in X-ray Computed Tomography, Salt Lake City, 2011.

[96]   O. Watzke and W. A. Kalender, "A pragmatic approach to metal artifact reduction in CT: merging of metal artifact reduced images," *Eur Radiol,* vol. 14, pp. 849-56, May 2004.

[97]   G. H. Glover and N. J. Pelc, "An algorithm for the reduction of metal clip artifacts in CT reconstructions," *Med Phys,* vol. 8, pp. 799-807, Nov-Dec 1981.

[98]   W. A. Kalender, R. Hebel, and J. Ebersberger, "Reduction of CT artifacts caused by metallic implants," *Radiology,* vol. 164, pp. 576-7, Aug 1987.

[99]   E. Meyer, R. Raupach, M. Lell, B. Schmidt, and M. Kachelriess, "Normalized metal artifact reduction (NMAR) in computed tomography," *Med Phys,* vol. 37, pp. 5482-93, Oct 2010.

[100]   E. Meyer, R. Raupach, M. Lell, B. Schmidt, and M. Kachelriess, "Frequency split metal artifact reduction (FSMAR) in computed tomography," *Med Phys,* vol. 39, pp. 1904-16, Apr 2012.

[101]   H. Erdogan and J. A. Fessler, "Ordered subsets algorithms for transmission tomography," *Physics in medicine and biology,* vol. 44, p. 2835, 1999.

[102]   K. Lange, "Convergence of EM image reconstruction algorithms with Gibbs smoothing," *Medical Imaging, IEEE Transactions on,* vol. 9, pp. 439-446, 1990.

[103]   R. Baron, "Understanding and optimizing use of contrast material for CT of the liver," *AJR. American journal of roentgenology,* vol. 163, pp. 323-331, 1994.

[104]   F. Cademartiri, N. R. Mollet, A. van der Lugt, E. P. McFadden, T. Stijnen, P. J. de Feyter, *et al.*, "Intravenous Contrast Material Administration at Helical 16–Detector Row CT Coronary Angiography: Effect of Iodine Concentration on Vascular Attenuation 1," *Radiology,* vol. 236, pp. 661-665, 2005.

[105]   S. J. Swensen, L. R. Brown, T. V. Colby, and A. L. Weaver, "Pulmonary nodules: CT evaluation of enhancement with iodinated contrast material," *Radiology,* vol. 194, pp. 393-398, 1995.

[106]   B. J. Barrett, R. W. Katzberg, H. S. Thomsen, N. Chen, D. Sahani, G. Soulez, *et al.*, "Contrast-induced nephropathy in patients with chronic kidney disease undergoing computed tomography: a double-blind comparison of iodixanol and iopamidol," *Investigative radiology,* vol. 41, pp. 815-821, 2006.

[107]   R. J. Solomon, R. Mehran, M. K. Natarajan, S. Doucet, R. E. Katholi, C. S. Staniloae, *et al.*, "Contrast-induced nephropathy and long-term adverse events: cause and effect?," *Clinical Journal of the American Society of Nephrology,* vol. 4, pp. 1162-1169, 2009.

[108]   R. Dittrich, S. Akdeniz, S. Kloska, T. Fischer, M. Ritter, P. Seidensticker, *et al.*, "Low rate of contrast-induced nephropathy after CT perfusion and CT angiography in acute stroke patients," *Journal of neurology,* vol. 254, pp. 1491-1497, 2007.

[109]   A. K. Hara, J. A. Leighton, V. K. Sharma, and D. E. Fleischer, "Small Bowel: Preliminary Comparison of Capsule Endoscopy with Barium Study and CT 1," *Radiology,* vol. 230, pp. 260-265, 2004.

[110]   R. C. Semelka, D. R. Martin, C. Balci, and T. Lance, "Focal liver lesions: Comparison of dual‐phase CT and multisequence multiplanar MR imaging including dynamic gadolinium enhancement," *Journal of Magnetic Resonance Imaging,* vol. 13, pp. 397-401, 2001.

[111]   D. Pan, C. O. Schirra, A. Senpan, A. H. Schmieder, A. J. Stacy, E. Roessl, *et al.*, "An early investigation of ytterbium nanocolloids for selective and quantitative "multicolor" spectral CT imaging," *ACS nano,* vol. 6, pp. 3364-3370, 2012.

[112]   K. J. Engel, C. Bäumer, J. Wiegert, and G. Zeitler, "Spectral analysis of scattered radiation in CT," in *Medical imaging*, 2008, pp. 69131R-69131R-11.

[113]   M. Bech, O. Bunk, T. Donath, R. Feidenhansl, C. David, and F. Pfeiffer, "Quantitative x-ray dark-field computed tomography," *Physics in medicine and biology,* vol. 55, p. 5529, 2010.

[114]   T. H. Jensen, M. Bech, O. Bunk, M. Thomsen, A. Menzel, A. Bouchet, *et al.*, "Brain tumor imaging using small-angle x-ray scattering tomography," *Physics in medicine and biology*, vol. 56, p. 1717, 2011.

[115]   T. Takahashi and S. Watanabe, "Recent progress in CdTe and CdZnTe detectors," *Nuclear Science, IEEE Transactions on*, vol. 48, pp. 950-959, 2001.

[116]   K. Rajendran, M. Walsh, N. de Ruiter, A. Chernoglazov, R. Panta, A. Butler, *et al.*, "Reducing beam hardening effects and metal artefacts in spectral CT using Medipix3RX," *Journal of Instrumentation*, vol. 9, p. P03015, 2014.

[117]   E. Frojdh, R. Ballabriga, M. Campbell, M. Fiederle, E. Hamann, T. Koenig, *et al.*, "Count rate linearity and spectral response of the Medipix3RX chip coupled to a 300 μ m silicon sensor under high flux conditions," *Journal of Instrumentation*, vol. 9, p. C04028, 2014.

[118]   Y. Liu, K. Ai, J. Liu, Q. Yuan, Y. He, and L. Lu, "A High‐Performance Ytterbium‐Based Nanoparticulate Contrast Agent for In Vivo X‐Ray Computed Tomography Imaging," *Angewandte Chemie International Edition*, vol. 51, pp. 1437-1442, 2012.

[119]   E. N. Gimenez, R. Ballabriga, M. Campbell, I. Horswell, X. Llopart, J. Marchal, *et al.*, "Characterization of Medipix3 with synchrotron radiation," *Nuclear Science, IEEE Transactions on*, vol. 58, pp. 323-332, 2011.

[120]   R. Popovtzer, A. Agrawal, N. A. Kotov, A. Popovtzer, J. Balter, T. E. Carey, *et al.*, "Targeted gold nanoparticles enable molecular CT imaging of cancer," *Nano letters*, vol. 8, pp. 4593-4596, 2008.

[121]   S. J. Schambach, S. Bag, L. Schilling, C. Groden, and M. A. Brockmann, "Application of micro-CT in small animal imaging," *Methods*, vol. 50, pp. 2-13, Jan 2010.

[122]   F. Hallouard, N. Anton, P. Choquet, A. Constantinesco, and T. Vandamme, "Iodinated blood pool contrast media for preclinical X-ray imaging applications--a review," *Biomaterials*, vol. 31, pp. 6249-68, Aug 2010.

[123]   P. F. O'Loughlin, S. Morr, L. Bogunovic, A. D. Kim, B. Park, and J. M. Lane, "Selection and development of preclinical models in fracture-healing research," *The Journal of Bone & Joint Surgery*, vol. 90, pp. 79-84, 2008.

[124]   D. W. Holdsworth and M. M. Thornton, "Micro-CT in small animal and specimen imaging," *Trends in Biotechnology,* vol. 20, pp. S34-S39, Aug 2002.

[125]   Q.-Y. Cai, S. H. Kim, K. S. Choi, S. Y. Kim, S. J. Byun, K. W. Kim, *et al.*, "Colloidal gold nanoparticles as a blood-pool contrast agent for X-ray computed tomography in mice," *Investigative radiology*, vol. 42, pp. 797-806, 2007.

[126]   E. G. Barcelon, S. Tojo, and K. Watanabe, "X-ray computed tomography for internal quality evaluation of peaches," *Journal of agricultural engineering research*, vol. 73, pp. 323-330, 1999.

[127]   R. A. Johns, J. S. Steude, L. M. Castanier, and P. V. Roberts, "Nondestructive measurements of fracture aperture in crystalline rock cores using X ray computed tomography," *Journal of Geophysical Research: Solid Earth (1978–2012),* vol. 98, pp. 1889-1900, 1993.

[128]   H. Martz, S. Azevedo, J. Brase, K. Waltjen, and D. Schneberk, "Computed tomography systems and their industrial applications," *International Journal of Radiation Applications and Instrumentation. Part A. Applied Radiation and Isotopes*, vol. 41, pp. 943-961, 1990.

[129]   J. Bradbury and A. Hambly, "An investigation of errors in the amperometric and starch indicator methods for the titration of millinormal solutions of iodine and thiosulphate," *Australian Journal of Scientific Research A Physical Sciences,* vol. 5, p. 541, 1952.

[130]   C. D. Humphrey and F. E. Pittman, "A simple methylene blue-azure II-basic fuchsin stain for epoxy-embedded tissue sections," *Biotechnic & Histochemistry,* vol. 49, pp. 9-14, 1974.

[131]   N. Nakajima, M. Hijikata, H. Yoshikura, and Y. K. Shimizu, "Characterization of long-term cultures of hepatitis C virus," *Journal of Virology*, vol. 70, pp. 3325-3329, 1996.

[132] F. O. Schmitt, J. Gross, and J. H. Highberger, "A new particle type in certain connective tissue extracts," *Proceedings of the National Academy of Sciences of the United States of America*, vol. 39, p. 459, 1953.

[133] B. D. Metscher, "MicroCT for comparative morphology: simple staining methods allow high-contrast 3D imaging of diverse non-mineralized animal tissues," *BMC physiology,* vol. 9, p. 11, 2009.

[134] S. Moser, S. Nau, M. Salk, and K. Thoma, "In situ flash x-ray high-speed computed tomography for the quantitative analysis of highly dynamic processes," *Measurement Science and Technology,* vol. 25, p. 025009, 2014.

[135] V. Cnudde, B. Masschaele, M. Dierick, J. Vlassenbroeck, L. V. Hoorebeke, and P. Jacobs, "Recent progress in X-ray CT as a geosciences tool," *Applied Geochemistry,* vol. 21, pp. 826-832, 2006.

[136] E. Roessl, D. Cormode, B. Brendel, K. J. Engel, G. Martens, A. Thran, *et al.*, "Preclinical spectral computed tomography of gold nano-particles," *Nuclear Instruments & Methods in Physics Research Section a-Accelerators Spectrometers Detectors and Associated Equipment,* vol. 648, pp. S259-S264, Aug 21 2011.

[137] D. P. Cormode, E. Roessl, A. Thran, T. Skajaa, R. E. Gordon, J. P. Schlomka, *et al.*, "Atherosclerotic plaque composition: analysis with multicolor CT and targeted gold nanoparticles," *Radiology,* vol. 256, pp. 774-82, Sep 2010.

[138] S. Feuerlein, E. Roessl, R. Proksa, G. Martens, O. Klass, M. Jeltsch, *et al.*, "Multienergy photon-counting K-edge imaging: potential for improved luminal depiction in vascular imaging," *Radiology,* vol. 249, pp. 1010-6, Dec 2008.

List of Publications

Peer-Reviewed Journals

- R. A. Nasirudin, P. Penchev, K. Mei, E. J. Rummeny, M. Fiebich, P. B. Noël,. "A Monte-Carlo Software Bench for Simulation of Spectral K-Edge CT Imaging: Initial Results." EJMP, *in press*

- R. A. Nasirudin, K. Mei, P. Penchev, A. Fehringer, F. Pfeiffer, E. J. Rummeny, M. Fiebich, P. B. Noël, "The benefits of Spectral CT for Metal Artifact Reduction." PLOS ONE, *in press*

- R. A. Nasirudin, S. Allner, J. J. Nappi, K. Mei, F. K. Kopp, E. J. Rummeny, H. Yoshida, P. B. Noël, "The performance of computed-aided diagnosis for CT colonoscopy using virtual monochromatic images." Medical Physics, *in preparation*

- R. A. Nasirudin, J. Schwarz, A. Fehringer, J. Schock, E. J. Rummeny, F. Pfeiffer, P. B. Noël, "Advance micro-CT algorithms for non-destructive testing." Measurement Science and Technology, *in preparation*

- F. Nazari, R. A. Nasirudin, K. Mei, F. Kopp, E. J. Rummeny, T. Lasser, P. B. Noël, "Iterative Iodine Detection and Enhancement Algorithm for Dual-Energy CT." Physics in Medicine and Biology, *in preparation*

- F. Kopp, T. Baum, R. A. Nasirudin, E. G. Garcia, R. Burgkart, E. J. Rummeny, J. S. Bauer, P. B. Noël, "Trabecular bone microstructure assessed by low-dose MDCT and iterative reconstruction predicts vertebral bone strength." PLOS ONE, *in preparation*

- R. Meier, K. Thuermel, P. B. Noël, P. Moog, M. Sievert, C. Ahari, R. A. Nasirudin et al. (2014), "Synovitis in patients with early inflammatory arthritis monitored with quantitative analysis of dynamic contrast-enhanced optical imaging and MR imaging." Radiology 270(1): 176-185.

Conference Proceedings (Chronological Order)

- R. A. Nasirudin, R. Tachibana, J. J. Nappi, K. Mei, F. K. Kopp, E. J. Rummeny, H. Yoshida, P. B. Noël, "A comparison of material decomposition techniques for dual-energy CT colonography." SPIE Medical Imaging 2015, *in press*

- R. A. Nasirudin, K. Mei, F. K. Kopp, E. J. Rummeny, P. B. Noël, "Reduction of iodinated contrast medium in CT: feasibility study." SPIE Medical Imaging 2015, *in press*

- F. K. Kopp, R. A. Nasirudin, K. Mei, A. Fehringer, F. Pfeiffer, E. J. Rummeny, P. B. Noël, "Region-of-interest processing for iterative reconstruction in x-ray computed tomography." SPIE Medical Imaging 2015, *in press*

- F. K. Kopp, T. Baum, R. A. Nasirudin, E. J. Rummeny, J. S. Bauer, P. B. Noël, "Trabecular Bone Microstructure Assessed by Low-Dose MDCT and Iterative Reconstruction Predicts Vertebral Bone Strength." *RSNA 2014, Chicago, Illinois, USA.*

- J. J. Nappi, D. Regge, R. A. Nasirudin, P. B. Noël, H. Yoshida, "Computer-aided Detection for Non-cathartic Low-dose Virtual Monochromatic CT Colonography." *RSNA 2014, Chicago, Illinois, USA.*

- R. A. Nasirudin, P. Penchev, K. Mei, E. J. Rummeny, M. Fiebich, P. B. Noël. "A comparison of simulation tools for photon-counting spectral CT " In *SPIE Medical Imaging (pp. 90334W-90334W). International Society for Optics and Photonics. 2014*

- R. A. Nasirudin, K. Mei, P. Penchev, E. J. Rummeny, M. Fiebich, P. B. Noël. "Application of Photon-Counting CT: Metal Artifact Reduction", *RSNA 2013, Chicago, Illinois, USA.*

- R. A. Nasirudin, K. Mei, P. Penchev, E. J. Rummeny, M. Fiebich, P. B. Noël. "Reduction of Artifacts Caused by High-Z Materials in Dental Spectral CBCT". *In Fully 3D 2013, Lake Tahoe, California, USA.*

- R. A. Nasirudin, P. Penchev, K. Mei, E. J. Rummeny, M. Fiebich, P. B. Noël. "Characterization of spectral X-ray imaging for dental cone-beam computed tomography". In *SPIE Medical Imaging (pp. 86684S-86684S). International Society for Optics and Photonics*. 2013

- R. A. Nasirudin, R. Meier, C. Ahari, M. Sievert, M. Fiebich, E. J. Rummeny, P. B. Noël, "Preliminary clinical results: an analyzing tool for 2D optical imaging in detection of active inflammation in rheumatoid arthritis." *In SPIE Medical Imaging (pp. 796512-796512). International Society for Optics and Photonics.* 2011.